

# Monitoring angiogenesis using magnetic resonance methods

**Holm, David Alberg**

*Publication date:*
2008

*Document Version*
Publisher's PDF, also known as Version of record

# *Monitoring angiogenesis using magnetic resonance methods*

**David Alberg Holm**

IMM-PHD-2008-199

Technical University of Denmark
Informatics and Mathematical Modelling
Building 321, DK-2800 Kongens Lyngby, Denmark
Phone +45 45253351, Fax +45 45882673
reception@imm.dtu.dk
www.imm.dtu.dk
IMM-PHD-2008-199

# Summary

When a tumor reaches a certain size it can no longer rely on passive perfusion for nutrition. The tumor therefore emits signaling molecules which stimulating surrounding vessels to divide and grow towards the tumor, a process known as angiogenesis. Very little angiogenesis is present in healthy adults where it is primaily found in wound healing, pregnancy and during the menstrual cycle. This thesis focus on the negative consequences of angiogenesis in cancer. It consists of a an initial overview followed by four manuscripts. The overview gives a short introduction to the process of angiogenesis and the involved signaling molecules. Subsequently, a short review of contrast agents and perfusion measurements is given. Finally, methods for monitoring angiogenesis using magnetic resonance imaging are reviewed.
A method for monitoring early stages of angiogenesis as well as the effect of anti-angiogenic treatment is presented in the first manuscript. In the second and third manuscript, two separate methods of quantifying perfusion, blood volume and vessel permeability are presented. The methods are used to show that drug delivery to a xenografted tumor is plausible and to show possible vascular maturation in a transgenic mouse model. The last manuscript presents a new method for *in vivo* cell labeling. This method could find use in studying the metastatic spread of cancer cells throughout the body.

# Resumé

Når en tumor når en vis størrelse kan dens behov for ernæring ikke længere opfyldes ved passiv diffusion alene. Derfor udsender tumoren signalstoffer som stimulerer omkring liggende kar til at dele sig og vokse hen imod tumoren, en proces som kaldes angiogenese. Angiogenese finder primært sted hos raske i forbindelse med sårheling, vækst og kvindens menstruations cyklus. I denne afhandling fokuseres på de negative konsekvenser af angiogenese i forbindelse med cancer. Afhandlingen består af en sammenfatning fulgt af fire artikler. Sammenfatningen giver en kort introduktion til angiogenese samt hvilke signalstoffer er involveret heri. Dernæst gives en kort introduktion til kontraststoffer og måling af perfusion. Tilsidst introduceres metoder til monitorering af angiogenese ved hjælp af magnetisk resonans billeddannelse.
Gennem artiklerne præsenteres metoder til at monitorere de tidlige stadier af angiogenese samt effekten af anti-angiogenetisk behandling. Dernæst anvendes forskellige perfusionsmetoder til at monitorere perfusion, blodvolumen og permeabilitet af angiogenetiske kar. Disse metoder sandsynliggør at et kemoterapeutisk stof kan leveres til en transplanteret hjernetumor. Endvidere viser de en mulig modning af karrene i en transgen mamma brystcancer model. Til slut præsenteres en metode til mærkning af celler *in vivo*. Denne metode kan på sigt udvikles til at monitorere spredningen af cancer celler (metastaser).

# Preface

This thesis was prepared at Informatics Mathematical Modelling, the Technical University of Denmark and Danish Reserch Centre for Magnetic Resonance, Copenhagen University Hospital, Hvidovre in partial fulfillment of the requirements for acquiring the Ph.D. degree in engineering.

The thesis deals with monitoring anigogenesis using magnetic resoanance methods. The main focus has been on developing techniques for monitoring the effects of anti-angiogenic drugs in cancer.

Readers are expected to have a basic understanding of magnetic resonance imaging and spectroscopy as well as a basic understanding of normal physiology. The more advanced methods used in this thesis will briefly be presented in the following chapters.

The thesis consists of a summary report and a collection of four manuscripts written during the period 2004–2008.

Hvidovre, May 2008
David Alberg Holm

# Manuscripts included in this thesis

**Manuscript I:**
David Alberg Holm, Carsten Dan Ley, Paul E.G. Kristjansen, Ian John Rowland: *In vivo angiogenesis assayed using MRI*

**Manuscript II:**
Yoshinori Kato, David Alberg Holm, Baasil Okollie, and Dmitri Artemov: *Noninvasive Detection of Temozolomide in Brain Tumor Xenograft by Magnetic Resonance Spectroscopy*

**Manuscript III:**
David Alberg Holm*, Sadia Asghar Butt*, Lise Vejby Søgaard, Henrik B.W. Larsson: *Perfusion and permeability measurements using a single T1W acquisition in a transgenic mammary cancer model.*

**Manuscript IV:**
David Alberg Holm, Ian John Rowland: *In vivo metabolite compartmentalization probed using intracellular GdDTPA*

* These authors contributed equally to the paper.

# Papers and abstracts not included

## *Peer reviewed papers*

David Alberg Holm, Karam Sidaros: *Slice profile optimization in arterial spin labeling using presaturation and optimized RF pulses.* Magn Reson Imaging. 2006 Nov;24(9):1229-40

Michael Sass Hansen, David Alberg Holm, Karl Sjøstrand, Carsten Dan Ley, Ian John Rowland, Rasmus Larsen: *Multiscale Hierarchical Support Vector Clustering.* International Symposium on Medical Imaging 2008

Christian Thomas Brandt, David Alberg Holm, Matthew Liptrot, C. Østergaard, J.D. Lundgren, Niels Frimodt-Møller, I.C. Skovsted, Ian John Rowland: *Impact of bacteremia on the pathogenesis of experimental pneumococcal meningitis.* J Infect Dis. 2008 Jan 15;197(2):235-44.

Kathrine Skak Madsen, David Alberg Holm, Lise Vejby Søgaard, Ian John Rowland: *The effect of paramagnetic manganese cations on 1H MR spectroscopy of the brain.* Accepted for publication in NMR Biomed

## *Peer reviewed abstracts*

David Alberg Holm, Karam Sidaros: *ASL: Comparison of presaturation and RF pulse optimization.* Proc Intl Soc Magn Reson Med 2005.

Kathrine S Madsen, David Alberg Holm, Lise Vejby Søgaard, GR Christoffersen, Ian John Rowland: *The effect of paramagnetic manganese cations on 1H MR spectroscopy of the brain.* Proc Intl Soc Magn Reson Med 2006.

David Alberg Holm, Carsten Dan Ley, Lise Vejby Søgaared, Helle J. Simonsen, Paul E.G. Kristjansen, Eva L. Lund, Ian John Rowland: *In vivo monitoring of angiogenesis within Matrigel chambers using MRI.* Proc Intl Soc Magn Reson Med - MR of Cancer Study Group Workshop 2006

Kato Yoshinori, David Alberg Holm, Baasil Okollie, Dimitri Artemov: *Visualization of Drug Distribution in Brain Tumors in Mice by MRSI.* Proc 98th American Association for Cancer Research Annual Meeting 2007.

David Alberg Holm, Ian John Rowland: *In vivo metabolite compartmentalization probed using intracellular GdDTPA.* Proc Intl Soc Magn Reson Med 2007.

Kathrine Skak Madsen, David Alberg Holm, Lise Vejby Søgaard, Ian John Rowland: *Preservation of manganese induced contrast in fixed rat brain.* Proc Intl Soc Magn Reson Med 2007.

# Acknowledgments

A lot of people have been of assistance in making this thesis possible. The first to come to mind is my wife whos patience and support, especially during the final phases of the work has been outstanding. Without her help and understanding I would never have completed my thesis.
A big thanks, and a beer or two, is also in order for all my supervisors who, each in their way, have contributed to parts of my work. A special thanks goes to Ian Rowland, who, even after moving accross the Atlantic, managed to keep me busy, my phone bills high and for revising manuscripts I and II. I am grateful toward Karam Sidaros for filling a lot of manuscripts and thesis chapters with red lines, and for his technical support. Rasmus Larsen has been of great assistance with image processing, selection of relevant courses and in explaining complex mathematics in a way a (part) medic can understand.
I wish to thank the following organizations for financial support without which the present thesis would not have been possible: The BIOP graduate school on biomedical optics and new laser systems, the Technical University of Denmark as well as Copenhagen University Hospital, Hvidovre.
Apart from my supervisors a lot of people need mentioning.
Samuel Alberg Kock for useful discussions and for listening to my wining about this and that throughout the thesis. Sadia Butt for countless hours of assistance with scanning, animal procedures, discussions, biochemical work and critical reading of almost all parts of this work and for her always

positive mind. Lise Søgaard for critical reading of several manuscripts and parts of the thesis, as well of her assistance in running (kicking!) and programming the preclinical scanner. Helle Simonsen for introducing me to preclinical procedures and her always positive mood. Lars Hanson for always having '5 minutes' to explain 'trivial' MR physics in a pedagogical way. Carsten Ley for all of his work on implanting Matrigel chambers, administering drugs and analysis of optical imaging involved in manuscript I. Henrik Larsson for his help and support in the preparation and planning of manuscript III. Lars Engelholm from Finsen Laboratoriet for providing the PyMT mice used in manuscript III.
A special thanks should also go to Dmitri Artemov, Yoshinori Kato, Arvind Pathak and Zhaver Bhujwalla who took great care of me during my visits to Johns Hopkins Hospital. They should also be thanked for their great work in manuscript II.

# List of abbreviations

| | |
|---|---|
| AIF | Arterial Input Function |
| α | Flip angle |
| ASL | Arterial Spin Labeling |
| BF | Blood flow or Perfusion |
| bFGF | basic Fibroblast Growth Factor |
| BOLD | Blood Oxygen Level Dependant |
| BSA | Bovine serum albumin |
| BV | Blood volume |
| $Ca^{2+}$ | Calcium |
| CLIO | Cross Linked Iron Oxide particles |
| $C_p$ | Plasma concentration |
| CT | Computed Tomography |
| $C_t$ | Tissue Concentration |
| dCE | Dynamic Contrast Enhancement ($T_1$ weighted dynamic MRI) |
| dSC | Dynamic Susceptibility Contrast ($T_2$* weighted dynamic MRI) |
| EMCL | ExtraMyoCellular Lipid |
| EPI | Echo Planar Imaging |
| $Fe^{3+}$ | Iron |
| Gd-BT-DO3A | gadobutrol or Gadovist |
| Gd-DTPA | gadopentate dimeglumine or Magnevist |
| Gd-HP-DO3A | Prohance |
| $Gd^{3+}$ | Gadolinium |
| GE | Gradient Echo |
| HIF-1 | Hypoxia Inducible Factor 1 |
| IMCL | IntraMyoCellular Lipid |
| $K_i$ | unidirectional transfer constant |
| $M_0$ | equilibrium magnetization |
| MION | Monocrystaline IrON oxide particles |

| | |
|---|---|
| MMCM | Macromolecular contrast agents |
| $Mn^{2+}$ | Manganese |
| MPIO | Micron sized Particles of Iron Oxide (1-6µm( |
| MRI | Magnetic Resonance Imaging |
| MTT | Mean Trasnsit Time |
| MVD | MicroVascular Density |
| mW | molecular weight |
| NCAM | Neural Cell Adhesion Molecules |
| NO | Nitric Oxide |
| NAA | N-acetyl aspartate |
| PDGF | Platelet Derived Growth Factor |
| PET | Positron Emissoon Tomography |
| PlGF | Placenta Growth Factor |
| PRESS | PointRESolved Spectroscopy |
| q | coordination number |
| R | residue impulse function |
| $R_1$ | $1/T_1$ |
| $r_1$ | longitudinal relaxivity |
| $R_2$ | $1/T_2$ |
| $r_2$ | transversal relaxivity |
| RF | Radio Frequency |
| SE | Spin Echo |
| SPECT | Single Photon Emission Computed Tomography |
| SPIO | SuperParamagnetic Iron Oxide particles (60-150nm) |
| SVD | Singular Value Decomposition |
| $T_1$ | Longitudinal or spin-lattice relaxation |
| $T_1W$ | $T_1$ weighted |
| $T_2$ | Transversal or spin-lattice relaxation |
| $\tau_d$ | diffusion correlation time |
| $\tau_m$ | correlation time |
| $\tau_r$ | rotational correlation time |
| tCr | total Creatine (creatinephosphate + creatine) |
| TD | saturation delay |
| TE | Echo Time |
| TI | Invertion time |
| TR | Repetition time |
| USPIO | Ultra Small SuperParamagnetic Iron Oxide particles (20-40nm) |
| VD | distribution volume |
| VEGF | Vascular Endothelial Growth Factor |
| VEGFR | VEGF receptors |
| VPF | Vacular Permeability Factor (same as VEGF) |
| VSOP | Very Small Superparamagnetic iron Oxide Particles (4-8nm) |
| X | inversion efficacy |

# Contents

# Chapter 1 Angiogenesis

The interest for tumor vasculature has existed since the 1920s and even earlier. In 1907 Goldmann[1] noticed that the development of tumors in organs resulted in ”chaotic irregularity” of the blood vessels and that growing tumors exhibited extensive formation of blood vessels most apparent in the zone of proliferation. He also noted that necrosis occurred even in highly vascularized growths and suggested that necrotic areas were ”the battlefield on which assailant and defendant both perished”. In 1945 Algire et al[2] noted that malignant cells provoke vascular proliferation.

Ever since more knowledge about the necessity for a tumor to establish a vasculature and its consequences have been obtained. In the following a brief introduction to angiogenesis is given. Which factors are involved, which types of angiogenesis exists and what the consequences of angiogenesis are will be introduced.

## *1.1 Introduction*

Angiogenesis is the process of formation of new blood vessels from existing ones. It is both benign (wound healing, fetal growth, menstrual cycle) and pathological (e.g. cancer, diabetic blindness, age-related macular degeneration, rheumatoid arthritis). In healthy adults angiogenesis is governed by the balance of angiogenic stimulating and inhibiting factors. If the balance between these is affected a pathology may develop.

Researchers are developing ways of inducing[3,4] and inhibiting angiogenesis [5] in order to cure various pathologies in which angiogenesis is either too active or lacking. The focus of this thesis is angiogenesis during cancer development.

## 1.2 Angiogenesis in cancer

Cancer begins with a population of cells which are unresponsive to normal control of cell division and cell death by which normal cells are regulated[6]. Therefore the cells divide and a lesion forms as a solid mass with no blood vessels. Normal cells can survive up to 100µm away from vessels whilst cancer cells, which are more resistant to hypoxia, can survive at greater distances[7]. This is visualized in figure 1.1[7].

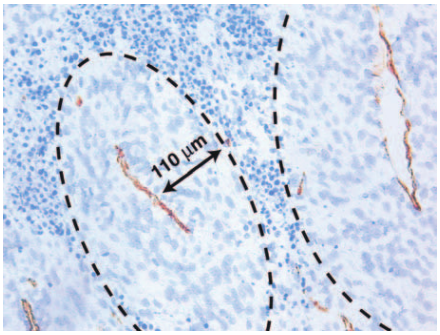


*Figure 1.1: Vessels stained with CD31 (brown) in a tumor. At 110µm the tumor cells are necrotic which can be seen by the hematoxylin staining of DNA (blue). From 7*

### 1.2.1 Tumors need angiogenesis

When the tumor reaches a size of 1-2 $mm^3$ the central cells can no longer be supplied with oxygen by passive diffusion. After a while the lack of oxygen makes the cells unable to maintain their electrolyte balance. The concentration of metabolites inside the cells becomes higher than outside the cells. As the cells are not permeable to metabolites but have water channels, water pours in to neutralize the metabolite concentration gradient (osmosis). The inflowing water makes the cells swell and ultimately burst. The intracellular content of the bursting cells damage surrounding cells and causes inflammation. This process is called necrosis. It differs from the naturally occurring process of apoptosis in which cells are degraded in a controlled manner. As the inner cells in the tumor lack oxygen and become necrotic, the tumor needs vascularization in order to grow further[8].

Normal blood vessels are lined with endothelial cells and include pericytes (smooth muscle cells). Further, fully developed blood vessels contain a basement membrane. The basement membrane is a specialized, sheet like

structure of the extracellular matrix. Its primary function is to anchor the endothelium to connective tissues and to act as a barrier preventing malignant cells from invading the deeper tissue. Larger vessels also contain smooth muscle cells which contraction state can be controlled, to regulate blood flow.

Blood vessels can be formed in three different ways:

- Vasculogenesis is the formation of vascular structures from endothelial stem cells (angioblasts), This form is mostly seen during embryonal development of the vascular system.
- Intussusception is the process, where the capillary wall extends into the lumen to split a single vessel in two. In this form the basal membrane is not breached.
- Angiogenesis is the process when new vessels are formed by sprouting from existing vessels.

Angiogenic sprouting is an ordered series of events. Cancer cells emit angiogenic growth factors which bind to receptors on the endothelial cells of preexisting blood vessels making the nucleus produce new proteolytic molecules. These dissolve the basement membrane. Endothelial cells proliferate and begin to migrate towards the tumor. Additional enzymes are produced to dissolve tissue in front of the budding vessels (matrix metalloproteinases). Sprouting endothelial cells form a blood vessel tube and individual blood vessels connect to form loops that can circulate blood[9].

Tumors have several ways of obtaining a vascular supply. The term Vascular-Cooption is used when tumor cells grow around existing vessels in highly vascularized organs[10]. Intussusception has been seen in some tumor xenografts[11]. Furthermore speculation has arisen that stem cells from the bone marrow may be involved in the neovascularization of tumors[12,13,14], meaning that vasculogenesis could also be involved.

However, it is widely accepted that the main way tumors obtain a blood supply is through sprouting angiogenesis. The transcription factor Hypoxia Inducible Factor 1 (HIF-1) is thought to be the main initiator of angiogenesis. HIF-1 regulates the physiologic responses to low oxygen levels (hypoxia) and pathophysiology of cancer, heart attach, stroke and chronic lung disease. The HIF-1 regulated genes encode for proteins that are

involved in angiogenesis and vascular remodeling.

Another contributing factor in angiogenesis is over expression of heat shock proteins (HSP). HSP supports the correct conformation, stabilization, activation, and localization of proteins, many of which are involved in tumor cell proliferation, angiogenesis and invasion[15]. Furthermore, defects in p53 tumor suppressor genes result in decreased production of the angiogenesis inhibitor thombospondin-1[16].

### 1.2.2 Signaling molecules

The secretion of angiogenic growth factors by the tumor cells (especially vascular endothelial growth factor (VEGF) and basic fibroblast growth factor (bFGF)) is considered to be the most important mechanism for induction of angiogenesis among a range of different molecules. Necrotic parts of the tumor, which are found in even well perfused tumors, induce a strong inflammatory response and VEGF is highly expressed in adjacent tissue[17]. Macrophages are often seen in tumors as they are in wound healing[18]. Non-malignant stromal cells inside the tumor can contribute to the production of angiogenic growth factors, possibly by stimulation from the tumor cells[19].

VEGF and bFGF have been studied in detail and are secreted by a wide variety of human tumors. Other molecules are involved[20], but description of these is beyond the scope of this text.

VEGF

VEGF was first described in 1989 as a molecule that enhances mitosis of endothelial cells[21]. Later, VEGF was discovered to be identical to vascular permeability factor (VPF) which had been described as increasing vascular permeability[22]. Because of the strong angiogenic effect and specificity for endothelium VEGF is considered to be the most important signaling molecule in tumor angiogenesis[20]. VEGF binds to various VEGF receptors (VEGFR) and neuropilins acting as enhancing co-receptors. VEGFR are expressed on most vascular endothelial cells, bone marrow derived cells including hematopoietic stem cells, and lymphatic endothelial cells. The VEGF molecule exists in different forms (VEGF-A through F and placenta growth factor (PlGF)[20]. For tumor angiogenesis VEGF-A is the most important type as it is considered to be the key regulator of blood vessel

formation[23]. Binding of VEGF-A to different VEGFR induce endothelial cell proliferation, angiogenesis and enhance vascular permeability. The murine version of VEGF, which was used to promote angiogenesis in matrigel chambers in manuscript I, has similar affinity for human receptors.

VEGF-A expression is regulated by multiple stimuli, including hypoxia through HIF-1 activation, p53 mutation, estrogen and nitric oxide (NO). In many tumors VEGF-A is continuously expressed even under normal oxygenation and can be particularly upregulated during hypoxia[24].

VEGF contributes to the phenotype of tumors in multiple ways: angiogenic sprouting is induced by its chemotactic and mitogenic effect on endothelial cells. Newly formed immature tumor vessels (which depend on VEGF signaling to survive) are allowed to persist. Vessels in and around the tumor are dilated as a result of NO production and high vascular permeability disrupts the fluid exchange between vessels and interstitium. VEGF expression is one of the first steps in the angiogenic process and is considered to be ”the master switch of the angiogenic cascade”[25].

bFGF

Basic fibroblast growth factor (bFGF) was originally isolated from bovine brain and pituitary extracts because of its proliferative effect on fibroblasts[26]. Binding of bFGF to an FGF receptor induces mitogenic, proliferative and chemotactic effects[27]

FGF receptors are expressed in many cell types, including tumor cells (so it is not specific for endothelium). However FGF does have a strong angiogenic effect and is a classically used growth factor for angiogenesis[28]. Inhibition of bFGF binding to the FGF receptor can prevent angiogenesis and tumor growth, though it is difficult to separate the effects on angiogenesis and the direct anti-proliferative effect[29].

bFGF signaling is regulated in multiple ways. It is strongly bound to heparin sulfate proteoglycans in the extracellular matrix from which it can be released by proteases during the angiogenic process[30]. It may also be released directly from cells producing it. bFGF modulates integrin expression and FGFR are believed to crosstalk with integrin during angiogenesis. bFGF regulates integrin expression and binds a form of integrin which is expressed on endothelial cells during angiogenesis and is required for bFGF and VEGF driven angiogenesis[31].

bFGF and VEGF control many of the same pathways and several observations supports crosstalk between the two signaling pathways. The synergistic effects of bFGF and VEGF have been observed by several researchers and may be a result of common signaling pathways[32,33].

### 1.2.3 Vascular abnormalities and hypoxia

In normal tissue, vessels are equally distributed and structured for efficient perfusion and oxygen exchange. Tumor vasculature is often disordered and unsystematic as shown in figure 1.2. The diameter of the vessels changes and the distance between branches is high which results in a high resistance to blood flow. Therefore even small changes in blood pressure can have consequences for the tumor blood flow. Tumor vessels appear dilated mainly due to VEGF. Blood vessels are immature which is why loops, blind ends and shunts between arteries and veins are common[8,34].

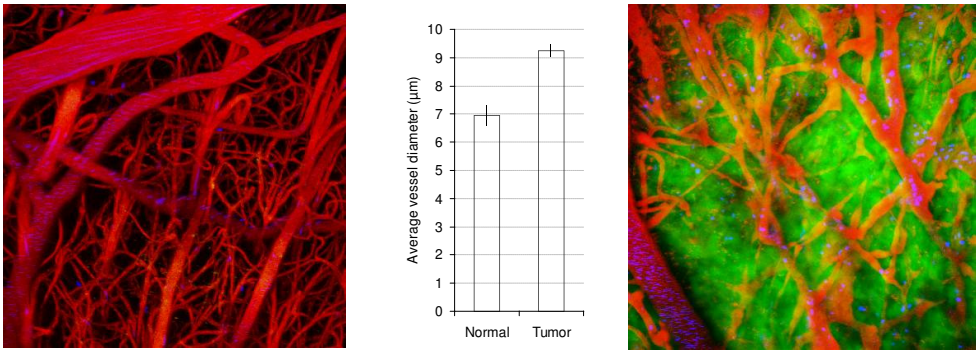


*Figure 1.2: Morphology of blood vessels (red) in the normal brain (left) is very different from the dilated and disorderly vessels in the U87 glioma xenograft (right). Deep tumor vessels are hidden by the bright signal from the tumor itself (green), vascular density is similar in both fields. Stained red blood cells (blue) appear round in slow-flowing tumor vessels, but only as single streaks in the normal vessels. In vivo multi-photon laser scanning micrographs; 250µm Z-projection, field width ~600µm, false colors. Kindly provided by Carsten Dan Ley who acquired it at the Edwin L. Steele laboratory. 3D quantification shows that tumor vessels are larger than the vessels in normal brain (middle).*

Tumor vessels generally have sparse or no pericyte coverage and an abnormal detached basement membrane[35]. Large openings between

endothelial cells make tumor vessels more permeable than normal vessels to contrast agents used for magnetic resonance imaging[36].

Even after the induction of angiogenesis, hypoxia is a feature of most solid tumors, even those which are well vascularized[37]. Vessels are not organized in the arteriole-capillary-venule pattern as normal vasculature meaning that blood pressure and flow is inhomogeneous across the tumor. Because of this, blood flow in tumor vessels can be low or intermittent and even tumor cells in close proximity to a vessel may experience transient periods of hypoxia[38]. Acute vascular collapse due to high interstitial pressure[39,40,41] the immune related destruction of cells, and the release of toxic agents[42] has been speculated to explain this.

Erythrocytes flowing through loops or shunts can have suboptimal conditions for oxygen exchange. Furthermore tumor cells proliferate very rapidly, meaning that metabolic demands increase faster than the vascular system can support. This increases tumor hypoxia and makes the vascular supply the rate limiting step for further tumor growth[43].

The main cellular response to hypoxia is the release of HIF-1, which in tumors mediates angiogenesis, increased survival, proliferation and increased glucose metabolism. These effects are critical to the formation of solid tumors. Because HIF-1 expression is a big advantage for tumor cells there is a strong selection for cells with HIF-1 pathways and HIF-1 is often active even without hypoxia[44].

Most clinically detectable tumors have necrotic zones where tumor vasculature is insufficient. HIF-1 inhibits apoptotic pathways leading to a predominance of necrotic cell death. Immune reaction to these necrotic zones, attract inflammatory cells contributing to the angiogenic process. The shift from apoptotic to necrotic cell death may be an important step for development and growth of cancers[45].

Exposure to hypoxia may contribute to promoting tissue invasion and increasing metastatic potential. In clinical tumors hypoxia has been correlated with tumor progression, increased metastatic potential and poor prognosis[44].

## 1.3 Inhibition of angiogenesis and vascular disruptive agents

As tumors depend on vascular supply in order to grow it follows that inhibition of the vascular development may be desirable. This form of therapy is called vascular targeted therapy and exploits ways in which tumor vasculature differs from normal vasculature. Tumor vessels have an activated endothelium which is proliferating, a basement membrane which is abnormal, and are immature and unstable. Thus, drugs targeting developing vessels with limited effect on normal vasculature have been developed.

Two different forms of vascular targeted therapy exist. Anti-angiogenic therapy targets angiogenesis and thereby limits the growth of new vessels while leaving existing vessels intact. Vascular disruptive therapy destroys existing tumor vessels without affecting normal vessels in the body. Not all drugs fall into one of these two categories. Many anti-angiogenic drugs have vascular damaging effects at high doses and some cancer drugs have secondary anti-angiogenic effects. For example chemotherapeutic agents target all dividing cells including the endothelial cells.

### 1.3.1 anti-angiogenic therapy

Anti-angiogenic therapy stops the formation of new blood vessels but may induce regression of immature tumor vessels as well. As previously mentioned, vascular supply is the rate limiting step in tumor growth. Therefore, prevention of angiogenesis should stop further growth. Indeed preclinical studies have shown that inhibition of angiogenesis decreases mean vascular diameter and arrests tumor growth[46].

Most of the anti-angiogenic drugs block the effects of VEGF at some level. This may happen by binding free VEGF, blocking the receptors or by inhibiting the function of the receptors. VEGF is an ideal target because of its many roles in angiogenesis and the limited side effects in normal adults. Because of VEGFs role, inhibition of VEGF is most likely necessary in all anti-angiogenic therapy, but may not be able to stand alone[47].

Thalidomide, though not initially developed for this purpose, is an example of a drug found to have a strong anti-angiogenic effect [48]. Thalidomide may downregulate the synthesis of an integrin that is essential for VEGF and

bFGF induced angiogenesis[49]but the mechanism for the anti-angiogenic action of Thalidomide is not fully understood[50]. Thalidomide was employed as an anti-angiogenic treatment in the Matrigel Chamber assay described in manuscript I.

### 1.3.2 Vascular disruptive therapy

Vascular disruptive agents do not affect angiogenesis directly but affects blood flow through existing vasculature. Vascular disruptive agents cause hypoxia which only leaves viable cells on the rim of the tumor close to vasculature in the surrounding tissue. The main classes of agents are tubulin binding agents and flavonoids.

Flavonoids are mainly known for the DMXAA compound, currently in phase II clinical trial testing. The method of action of the flavonoids is not entirely clear. However, stable production of tumor necrotic factor and elevation of NO production has been observed. How these factors lead to a decrease in blood flow and apoptosis of endothelial cells is not yet understood[51].

The tubulin binding agents interfere with the function of the cytoskeleton of endothelial cells. The classic agent is Colcicine which is too toxic for clinical use. An alternative is Combretastatin having similar effects. In general tubulin binding agents destabilize the microtubuli of the endothelial cytoskeleton and may also interfere with junctions between cells influencing vascular permeability. The exact method by which they lower blood flow is still unknown. Tumor blood vessels are more sensitive to tubulin binding agents than normal blood vessels which may be caused by the lack of maturity of the tumor vessels.

### 1.3.3 Pros and cons for vascular targeted therapy

Mainly tumors exhibit neovasculature in adults. Hence, antivascular therapy should be more specific than chemotherapy and radiation. Secondly, since endothelial cells are not malignant they are less likely to develop drug resistance. Thirdly, endothelial cells are in direct contact with the bloodstream so delivery of the vascular targeted agent should be persistent.

Correctly administered vascular targeted agents do, however, have side effects[52] and primarily delay the growth of tumor. The increased hypoxia in

the tumor may even cause selection of clones that are resistant to hypoxia or increase production of angiogenic growth factors.

The vascular damaging agents can have significant effects on tumor blood flow and most of the tumor may become necrotic after treatment. Unfortunately the necrotic part of the tumor can be repopulated very quickly and blood flow restored making the delay in tumor growth small[51]. Because of this, vascular targeted therapy is not widely used in the clinic.

Vascular targeted therapy was originally envisioned as a monotherapy and concern was raised that reduced tumor perfusion would compromise drug delivery to the tumor and hypoxia would reduce sensitivity to radiation therapy. Fortunately, this was not the case and vascular targeted can thereby increase sensitivity to chemotherapy and radiation[53,54].

Details of the synergistic effect of vascular targeted drugs and traditional cancer therapy remain to be elucidated. Evidence that anti-angiogenic drugs, especially the ones which affect VEGF, can work to ”normalize” tumor vasculature by inhibiting VEGFs effect on vascular permeability exists. This would normalize osmotic pressure gradients and increase exchange of water and molecules between the tumor vasculature and interstitium. Although the long term effect of the vascular targeted agents is to deprive the tumor of blood supply a ”normalization window” may exist where the tumor perfusion is significantly improved[34]. Most studies have shown improvement in vascular function and drug delivery when combined with anti-VEGF treatment[55] though some have not[56]. This indicates that the correct timing between the two may be important for efficient synergistic effects.

Synergistic effects between traditional cancer treatment and vascular disruptive agents are more intuitive. The vascular disruptive agents usually target the core of the tumor due to the almost complete disruption of tumor blood vessels. Chemotherapy and radiation primarily target the rim of the tumor since delivery of drugs and oxygen is usually improved in the rim compared to the center of the tumor.

# Chapter 2 MR contrast agents

As the experimental basis of this thesis and all papers included, depend on the usage of contrast agents to estimate blood volume (Manuscript I), perfusion (Manuscripts II+III) or to label cells (Manuscript IV) a brief introduction to MR contrast agents is in place. Perfusion measurements and angiogenesis monitoring based on employment of different contrast agents will be described in chapter 3 and 4, respectively.

## 2.1 Introduction

Magnetic resonance imaging produces images by measuring RF signals from the magnetic moments of primarily water protons although other elements ($^{13}$Carbon,$^{31}$Phosphor,$^{3}$Helium) can be imaged as well. Because of its abundance proton MR is the most widely used method both clinically and preclinically[57].

In conventional MR images the contrast depends mainly on the proton spin density and the longitudinal ($T_1$) and transverse ($T_2$) relaxation times. These differences are often enough to provide good contrast between organs and to distinguish pathological from healthy tissue.

Nevertheless some pathological diseases do not lead to differences in morphology and do not show specific change in relaxation times. Combining MRI and contrast agents enhances the possibility to depict inflamed tissues in arthritis[58], tumor angiogenesis[59,60] and multiple

sclerosis[61].

New contrast agents have been developed in order to visualize molecular and cellular processes noninvasively[62]. This is possible by directing a tracer toward the target molecule or process of interest. Typically the target molecule is only present in very low concentrations. Therefore molecular imaging was traditionally used only in optical techniques, nuclear methods such as positron emission tomography (PET), and single photon emission computed tomography (SPECT). Because of the low spatial resolution of the nuclear methods, alternative methods based on magnetic resonance imaging (MRI) are being developed. The main challenge is to enhance the sensitivity of MR to the contrast agent. This may be realized using contrast agents with a high relaxivity such as iron oxide particles with a high payload of iron. Such methods have enabled MRI to monitor single cells. For example Heyn et al labeled cancer cells and followed metastasis to the brain[63].

## 2.2 Generation of contrast

The equilibrium magnetization in MRI can be disturbed by radiation with an external radio frequency (RF) field. When the RF is switched off the system relaxes back to thermal equilibrium, a process known as relaxation. Two different forms of relaxation are distinguished, namely spin-lattice or longitudinal relaxation ($T_1$) and spin-spin or transverse relaxation ($T_2$). The transverse relaxation may be accelerated by macro and microscopic field inhomogeneities in which case the relaxation time is referred to as $T_2$* being shorter than $T_2$ as the latter reflects only signal loss caused by nuclear interactions.

The potency of a contrast agent to shorten $T_1$ and $T_2$ is denoted its relaxivity. It is defined by the change in longitudinal and transversal relaxtion rates per unit of contrast agent[64].Relaxivity is denoted $r_1$ or $r_2$ and is expressed in $mM^{-1}s^{-1}$. In general $r_1$ decreases at higher field strength and $r_2$ less so. The ratio between $r_1$ and $r_2$ determines if a contrast agent is suitable for $T_1$ weighted imaging or if it only suitable for $T_2$ weighted imaging. The so called $T_1$ agents which are typically Gd-chelates have a low $r_2$ compared to $r_1$ and generate positive contrast on most $T_1$ weighted images while $T_2$ agents have a large $r_2$ yielding negative contrast on most $T_2$ weighted images.

### 2.2.1 $T_1$ Contrast agents

$T_1$ contrast agents are often paramagnetic ion containing agents. The metal ion must have the property of shortening $T_1$ without causing significant broadening of the proton peak. The most commonly used $T_1$ agent is the lanthanide Gadolinium ($Gd^{3+}$) which has a high paramagnetic moment. The transition metal ions manganese ($Mn^{2+}$) and iron ($Fe^{3+}$) are also good $T_1$ agents. Most free metal ions are toxic for living tissue and must be chelated in order to avoid toxicity.

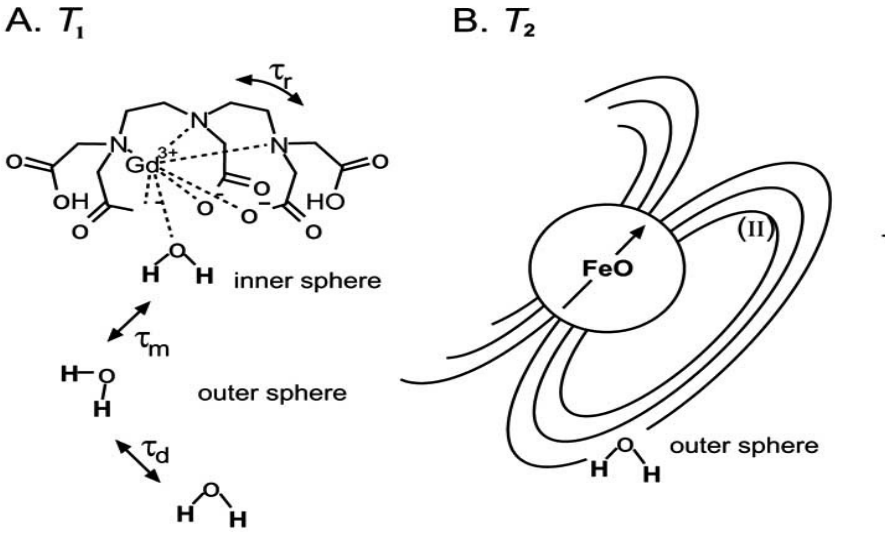


*Figure 2.1: Schematic of the physical principle of the working of MRI contrast agents. (A) T1 lowering agent Gd-DTPA. Efficient relaxation is experienced by water coordinated to the inner sphere of the $Gd^{3+}$ ion (first hydration layer). Important properties governing relaxation are the rotational correlation time r of the whole complex, the exchange correlation time m, and the diffusion correlation time d. (B) Susceptibility induced dephasing causes rapid loss of transverse magnetization resulting in short T2 relaxation times of water surrounding a superparamagnetic FeO particle. Adapted from reference 57*

The action of a $T_1$ agent can be explained using figure 2.1A showing Gd-DTPA (gadopentate dimeglumine) also known as Magnevist[57]. The

observed difference in relaxation is caused by an intrinsic contribution ($R_{1t}$) and a contribution from the contrast agent ($R_{1CA}$):

$$R_1 = R_{1t} + R_{1CA}, where\, R_1 = \frac{1}{T_1} \quad 2.1$$

$R_{1t}$ is the intrinsic relaxation without contrast agent and $R_{1CA}$ is the paramagnetic contribution of the contrast agent which can be formulated as follows:

$$R_{1CA} = r_1 \cdot [CA] \quad 2.2$$

where $r_1$ is the relaxivity ($mM^{-1}s^{-1}$) and [CA] is the concentration of the contrast agent. In principle the shortening of the relaxation rate is linear with the contrast agent concentration (first order approximation). Furthermore, it is apparent that the effect can be enhanced by either increasing the amount of contrast agent [CA] or using a contrast agent with higher relaxivity $r_1$.Although $r_1$ is a contrast agent specific parameter it also depends on the solvent and its distribution which could vary *in vivo,* i.e. when the contrast agent is confined to the blood pool. Thus, the contrast agent may not affect all water protons in the tissue equally. Therefore linearity of $R_1$ with concentration of contrast agent cannot always be guaranteed[65].

The paramagnetic contribution from the contrast agent is generally understood to originate from relaxation in two pools of water either coordinated directly with $Gd^{3+}$ (inner sphere) or located in the second coordination sphere and the bulk (outer sphere see figure 2.1A. For simplicity a qualitative description of the most important factors will be given here while a more thorough description can be found in the following papers[65,66,64].

The fluctuating local magnetic field created by the paramagnetic ion provides a relaxation pathway for the water protons. The interaction falls of rapidly with distance. Gd should therefore have at least one site at which water can coordinate directly (q=coordination number). Furthermore the Gd should have fast water exchange, characterized by the correlation time $\tau_m$, so that a considerable number of water molecules may experience relaxation. The rotational correlation time of the whole complex $\tau_r$ is also important. Normally Gd-DTPA has a high $\tau_r$. Slowing down the complex

results in fluctuations of the paramagnetic center at frequencies close to the Larmor frequency improving relaxation. Finally, diffusion provides relaxation to water molecules in bulk surrounding the paramagnetic entity. Diffusion is characterized by the diffusion correlation time $\tau_d$[57].
Most commercially available Gd based $T_1$ lowering agents are low molecular weigh poly(amino-carboxylate) complexes. In this thesis two different agents have been used Gd-DTPA (Magnevist) and Gd-BT-DO3A (Gadovist). Their chemical structures are shown in figure 2.2 together with the structure of choline, creatine and N-acetyl aspartate (NAA). Magnevist was used in the two perfusion papers included in this thesis, while both Magnevist and Gadovist were used in the cell labeling paper.

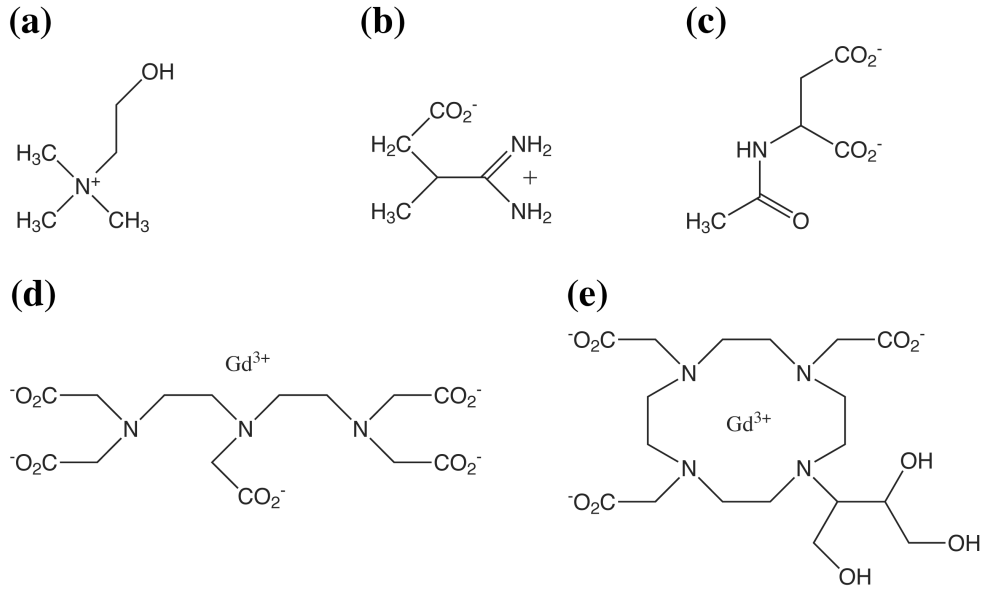


*Figure 2.2: Figure 6: Chemical structures, in charged form, of the metabolites: (a) choline (b) creatine (c) N-acetyl aspartate and contrast agents: (d) Gd-DTPA (Magnevist) and (e) Gd-BT-DO3A (Gadovist). Note that choline possesses an overall positive charge whilst zwitterionic creatine has both positive and negative charges and N-acetyl aspartate has two negatively charged carboxylate groups. Gd-DTPA is negatively charged whilst Gd-BT-DO3A is a neutral molecule.Kindly provided by Dr. Ian Rowland*

In order to improve image contrast the agents should have a local tissue concentration on the order of $10^{-7}$ mol/g tissue. This is sufficient when used

as a blood pool agent but not in order to image molecular epitopes expressed in the living body, since these receptors are usually only present in very low concentration of approximately $10^{-9}$ to $10^{-13}$ mol/g[67].
The low molecular contrast agents can be improved. They only have one water correlation site and their rotational correlation time $\tau_r$ is too short as a consequence of their low size. In addition the water exchange rate $1/\tau_m$ is in general too low for optimal relaxation.
Two different routes have been followed in order to improve $r_1$ of theese agents.
The first strategy aims to enhance $r_1$ by optimizing q, $\tau_r$ and $\tau_m$. Some have increased the water exchange rate[66,68] while others have increased the rotational correlation time by grafting chelates on to macromolecules[64]. Hitherto, these approaches have not lead to sufficiently high relaxation times for molecular imaging.
The second approach is to increase the number of $Gd^{3+}$ entities per particle. Multiple $Gd^{3+}$ chelates have been attached to dendrimers and these agents have been used as contrast agents[69,70]. Furthermore Aime et al[65] put multiple Prohance (Gd-HP-DO3A) inside an apoferritin cage obtaining relaxivites as high as 80 $mM^{-1}s^{-1}$. Their group later managed to monitor angiogenesis by labeling neural cell adhesion molecules (NCAM) with this complex[71].
The manganese ion ($Mn^{2+}$) is also a paramagnetic ion and may serve as an MRI contrast agent. Early studies used low doses of $MnCl_2$ in its ionic form although it is toxic[72]. The author of this thesis was involved in a work by Madsen et al[73] in which toxicity of $MnCl_2$ at low concentration was estimated based on spectroscopy. In this study, no toxic effects were found and $MnCl_2$ is quite popular in preclinical studies because it acts as a calcium ($Ca^{2+}$) analog. $Mn^{2+}$ can also be chelated to reduce the toxicity and a manganese based contrast agent, Mn-DPDD, is FDA approved for liver imaging[74].

### 2.2.2 $T_2$ contrast agents

The local magnetic field fluctuations of a paramagnetic ion result in a paramagnetic contribution to the transverse spin-spin relaxation, similar to the effect described for $T_1$. A more effective way of decreasing $T_2$ exists, using superparamagnetic contrast agents. These are usually iron oxide nanoparticles composed of magnetite ($Fe_3O_4$) or magnemite ($\gamma$-$Fe_2O_3$) with a diameter of 4nm to 2.8µm. They are also termed very small

superparamagnetic iron oxide particles (VSOP 4-8nm), ultra small superparamagnetic iron oxide particles (USPIO 20-40nm), superparamagnetic iron oxide particels (SPIO 60-150nm), or micron-sized particles of iron oxide (MPIO 1-6µm) according to their size or monocrystaline iron oxide particles (MION) or cross-linked iron oxide particles (CLIO) depending on their crystallin structure. MPIOs have been used to visualize individual cells[75].

The iron oxide particles can contain several thousand magnetically ordered iron ions and the net magnetic moment is much higher than of a single paramagnetic ion. The particles are not magnetic when outside a magnetic field but can be magnetized by the magnetic field inside the MR scanner. The effect on the transverse relaxivity can best be understood by the bulk susceptibility effect (figure 2.1B). The large magnetic moment of the superparamagnetic nanoparticles induces strong local field gradient yielding quick loss of phase coherence of the surrounding water proton spins[76,77]. Increased relaxivity can be observed at a considerable distance from the nanoparticles since the effects are not limited to water protons in close proximity to the nanoparticle. Water diffusion in the proximity of the nanoparticle enhances the dephasing effects.

Similar to $T_1$ we can define

$$R_2 = R_{2t} + R_{2CA}, where\, R_2 = \frac{1}{T_2} \quad 2.3$$

and

$$R_{2CA} = r_2 \cdot [CA] \quad 2.4$$

where $R_2$ and $r_2$ can also be substituted by $R_2^*$ and $r_2^*$.

As for the $T_1$ agents local decrease in R2 is strongly affected by biodistribution of the agent[78].

## 2.3 Measuring relaxivity of contrast agents

As described in 2.1 and 2.3 a linear relationship ($r_1/r_2$) between change in $R_1/R_2$ and contrast agent concentration exists. This relationship is not always linear *in vivo* as described, but a linear relationship is expected *in vitro*. Therefore, it is quite trivial to measure the water relaxivity for a contrast agent.

Since the possibility of inner-sphere relaxation and other interactions between the contrast agent and a given molecule, $r_1$ and $r_2$ may vary between metabolites and water. In order to measure $r_1$ and $r_2$ it is necessary to measure $R_1$ and $R_2$ of each metabolite separately in samples containing varying amounts of contrast agent.

Before presenting the results, $R_1$ measurement methods will briefly be introduced along with the exact method used to estimate relaxivity.

### 2.3.1 Spectroscopic $R_1$ measurements

In order to measure $R_1$ for each metabolite a new spectroscopic sequence was developed in which a non-selective inversion pulse was added to a PointRESolved Spectroscopy (PRESS) sequence. By varying the time between inversion and readout (TI) it was possible to fit $R_1$.

Conventionally the signal as a function of TI for an inversion recovery sequence is written as:

$$S \propto M_0 \cdot (1 - 2e^{-TI \cdot R_1} + e^{-TR \cdot R_1}) \quad 2.5$$

where repetition time (TR) is assumed >> TI, S is signal and $M_0$ is the equilibrium magnetization. This equation does not take the effects of imperfect inversion into account. Furthermore, the magnetization differs immediately before inversion, due to varying TI without changing TR. For these reasons a new set of equations were formulated:

$$S \propto M_0 + (M(0) - M_0) \cdot e^{-TI \cdot R_1} \quad 2.6$$

$$M(0) = M_0 \cdot X \cdot \left(1 - e^{-(TR - TI) \cdot R_1}\right) \quad 2.7$$

where M(0) is the magnetisation immediately before the inversion and X is the inversion efficacy with -1 corresponding to perfect inversion.

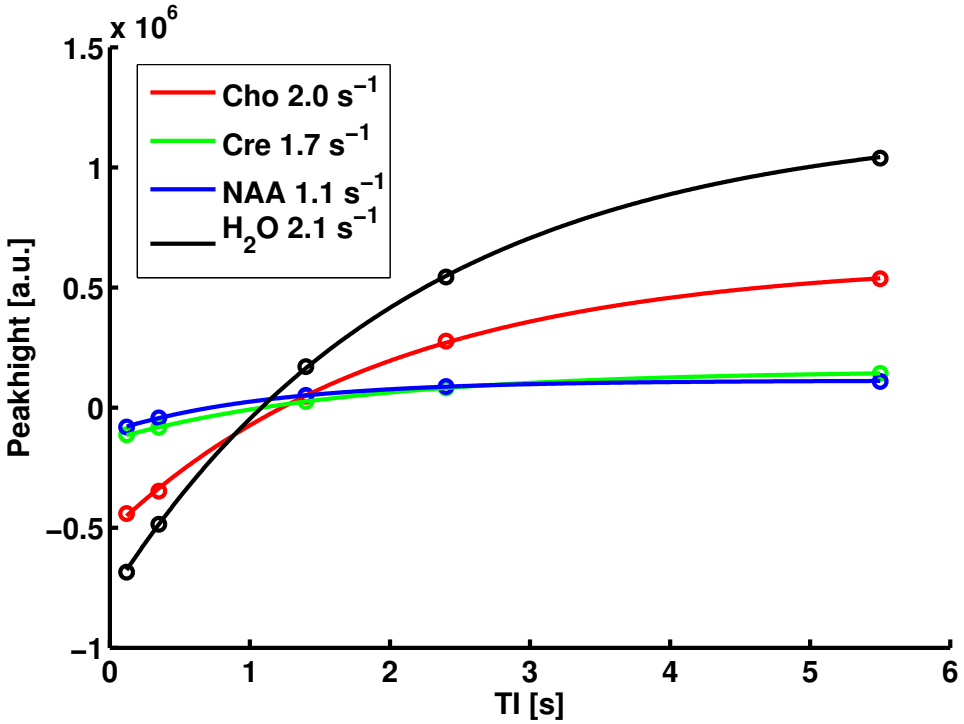


*Figure 2.3: Signal as a function of TI, together with fitted curve for Choline, Creatine, NAA and $H_2O$. Numbers after each metabolite are the fitted R1 values. The $H_2O$ signal values were divided by 20 in order to show all curves in one plot.*

Equations 2.6, 2.7 were fitted to the signal using a non linear least squares fitting method[79] implemented in MatLab. The fitted parameters were $M_0$, X and $R_1$. For the water suppressed metabolite $R_1$ measurements, the signal vs. time curves were fitted simultaneously for all three metabolites and equal inversion efficacy (X) was assumed. For the water relaxation measurements, a fixed inversion efficacy of -0.7 was used. An example of fitting the fitting employed is shown in figure 2.3.

The same measurement and fitting method was used for *in vivo* measurements of metabolite $R_1$s in the paper by Madsen et al[73] and in manuscript IV. Automatic peak fitting was tested but unfortunately the signal to noise of some of the inverted spectra was not sufficient to obtain robust results. The author therefore ended up manually annotating the peak and baseline positions of each spectrum.

### 2.3.2 Relaxivity measurements

In order to measure relaxivity for a given contrast agent, samples containing 25mM of choline, creatine and NAA were mixed with varying amounts of contrast agent (0 to 50µM). Signal as a function of TI for water (no water suppression) and the three metabolites (with water suppression) were measured for each sample and $R_1$ was fitted as described in the following. Samples with Bovine Serum Albumin (BSA) were also prepared in order to estimate the effects of protein binding. The slope of the concentration/$R_1$ curve is the $r_1$ relaxivity as depicted in figure 2.4.

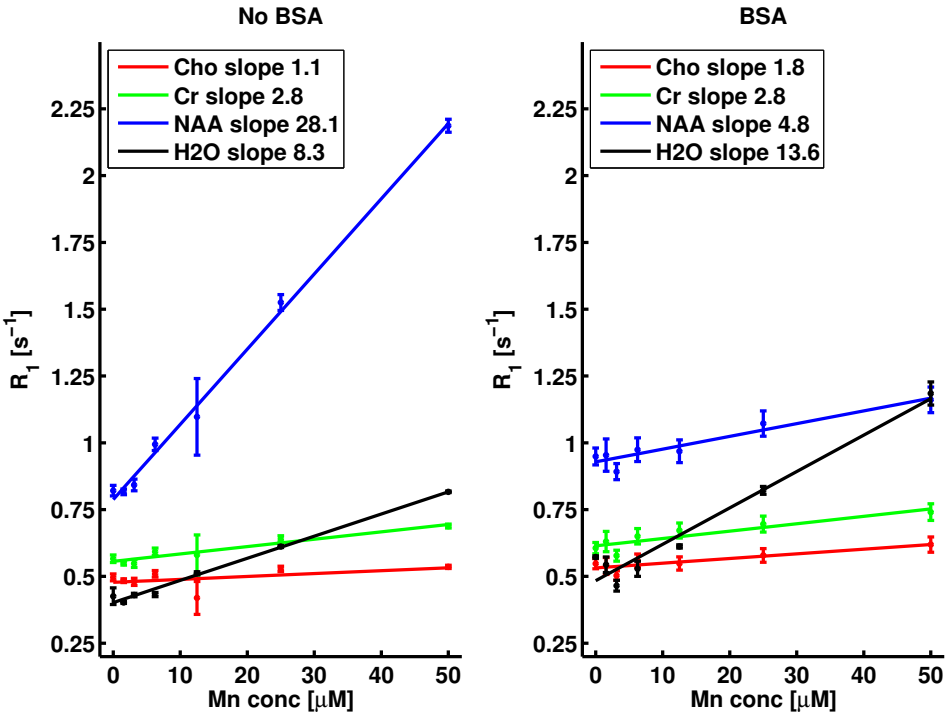


*Figure 2.4: Relaxivity plots for the non-protein (left) and the BSA-phantoms (right). $R_1$ for choline (cho), creatine (Cr), NAA and water are plotted as a function of the $Mn^{2+}$ concentration (µM). Bars are standard error of the fitted parameters.*

Figure 2.4 shows good linearity between contrast agent concentration and $R_1$, which was the case for all contrast agents. The results for each of the contrast agents will be presented in the next section.

## 2.4 Relaxivity of contrast agents at 4.7T

The measured relaxivities can illustrate some of the concepts introduced in the beginning of this chapter. The results of relaxivity measurements of Magnevist, Gadovist, and manganese on water, choline, creatine and NAA are shown in table 1 and the results will briefly be discussed based on the theory introduced previously.

| **Phantoms** | **$H_2O$** | **Choline** | **Creatine** | **NAA** |
|---|---|---|---|---|
| Magnevist | 4.4 (0.3) | 8.6 (0.2) ** ! | 3.9 (0.2) | 1.7 (0.3) ** |
| Magnevist BSA | 3.8 (0.3) | 7.8 (0.3) ** ! | 3.3 (0.4) | 1.0 (0.7) ** |
| Gadovist | 5.4 (0.4) | 2.4 (0.1) ** | 4.1 (0.2) ** | 3.7 (0.3) ** |
| Gadovist BSA | 5.6 (0.1) | 2.3 (0.2) ** | 3.7 (0.3) ** | 3.5 (0.3) ** |
| Mn | 8.3 (0.4) ! | 1.1 (0.8) ** | 2.8 (0.4) ** | 28.1 (0.8) ** ! |
| Mn BSA | 13.6 (1.3) ! | 1.8 (0.4) ** | 2.8 (0.6) ** | 4.8 (0.7) ** ! |

*Table 1: Relaxivities of Gadovist and Magnevist on metabolites with BSA and without BSA. Numbers in parenthesis are standard error of the fit.* Denotes statistically different from relaxivity of water (P<0.05) ** (P<0.005). ! denotes that the BSA and non BSA values are statistically different (P<0.05).*

### 2.4.1 Magnevist

The choline relaxivity for magnevist decreases slightly when BSA is added. Magnevist is anionic while choline is cationic. This means that increased inner-sphere relaxation can be expected in the absence of BSA. The cationic nature of the choline molecule will result in increased outer-sphere interaction with negative cations, causing the relaxation rate of the protons in the choline molecule to be increased compared to the other metabolites. In the presence of BSA, relaxivity of choline is slightly reduced, but it is still higher than the other metabolites suggesting that the ‘inner sphere’ interaction is reduced and the enhanced ‘outer sphere’ interaction of species with opposite charge remain.
The lowest relaxivity for Magnevist is for NAA, which is most likely explained by decreased interaction between the Magnevist and NAA because of their anionic nature. Creatine relaxivity lies between choline and

NAA relaxivity values which corresponding well with its zwitterionic nature.

### 2.4.2 Gadovist

None of the metabolites stand out as having either a very high or very low relaxivity with Gadovist, most likely due to the neutral nature of Gadovist.

### 2.4.3 Manganese

The water relaxivity for $Mn^{2+}$ increases in the samples with BSA. Free $Mn^{2+}$ cations in solution are able to interact with six $H_2O$ molecules (q=6). However, when albumin is present in the solution, albumin and $Mn^{2+}$ are complexed[80] reducing the number of water molecules that may interact with free $Mn^{2+}$ (q), potentially reducing the relaxation efficiency of $Mn^{2+}$. When bound, the motion of the $Mn^{2+}$ cations is slowed ($\tau_r$ decreases), enhancing the relaxation properties of the $Mn^{2+}$ cations. Consequently, the longitudinal relaxivity on water increases.
The NAA relaxivity of $Mn^{2+}$ is very high without BSA. This may be explained by inner-sphere interaction between the anionic NAA and the cationic $Mn^{2+}$. Similar to what was seen with Magnevist and choline, the anionic nature of NAA molecule will result in increased outer-sphere interaction with positive cations, causing increased relaxivity of NAA compared to the other metabolites. In the presence of BSA, NAA relaxivity is drastically reduced, but is still higher compared to the relaxivity of other metabolites suggesting a reduction of inner sphere interaction and that the enhanced outer sphere interaction remain. Moreover, the $Mn^{2+}$ cations were shown to least affect the longitudinal relaxivity of choline. This is in accordance with the fact that choline is positively charged consequently tending towards less strong interaction the positively charged $Mn^{2+}$ cations.

# Chapter 3 Measuring perfusion using MRI

It is important to distinguish blood flow and perfusion. Blood flow is a measure of how much blood flows through a vessel per time unit. The preferred unit for blood flow is ml per minute.

Perfusion is a measure of how much blood is available for exchange of oxygen, nutrients and waste products to the tissue. Therefore big vessels which run through the tissue, acting solely as 'pipes', should not be included in the perfusion measurement. Only arteriole, capillary and venolous blood flow should be included. Perfusion is measured as blood flow per unit time per unit tissue and the standard unit is ml per min per 100g of tissue.

As described in chapter 1 angiogenesis is a process in which new vessels are formed. For that reason the density of vessels in the tissue could be a good indicator for angiogenesis. Such a quantity does exist (microvascular density MVD) and can be measured using microscopy. MVD has been shown to correlate well with outcome and tumor grade[81]. Unfortunately, the spatial resolution of MRI (approx 100µm) does not allow MVD to be measured directly. A solution could be to measure flow in the vessels using MRI, but the tortuous structure of the vessels means that a given voxel within a tumor has blood flowing in multiple directions preventing correct flow estimates.

The purpose of angiogenesis is not flow per say but rather to exchange nutrients and deliver oxygen to the tumor cells. Thus, perfusion is an obvious choice for monitoring the efficiency of angiogenesis and perfusion

parameters have been correlated with e.g. MVD, to be further described in chapter 4.

In the following a brief introduction to the different methods which exist for quantifying perfusion and other vascular parameters will be given.

## 3.1 Introduction

As previously described, tumors become dependent on perfusion as they grow. When they reach a size of 1-2mm$^3$ the need for nutrients can no longer be met by passive diffusion and the tumor emits signaling molecules stimulating angiogenesis.

There are numerous ways to measure perfusion using MRI. Most include injection of an exogenous paramagnetic contrast agent which is injected through a vein.

In this thesis, I have used invasive methods that can provide better signal to noise and extra information (e.g. leakiness) compared to noninvasive methods. A brief attempt was made at implementing arterial spin labeling on the preclinical system but unfortunately hardware limitations hindered this method. For completeness, a brief introduction of two noninvasive methods will be given.

## 3.2 MR perfusion methods

### 3.2.1 Arterial spin labeling (ASL)

Arterial spin labeling is a non-invasive method which uses blood as an endogenous contrast agent. It was first introduced by Detre et al[82] and Williams et al[83] in 1992. Two separate images are acquired, one where blood supplying the tissue of interest is labeled using radio frequency pulses and one without labeling. The labeled blood exchanges with water in the tissue and changes its magnetization. The difference between the labeled and unlabeled images is perfusion weighted. The difference in signal is on the order of a few percent of the equilibrium signal which means that averaging is needed in order to measure a usable signal. ASL is quite sensitive to delays in the delivery of blood from the labeling area to the imaging volume due to $T_1$ relaxation during transit. As flow is generally

higher and distances smaller in rodents than humans this is less of an issue in preclinical experiments A good general introduction to ASL can be found in an article by Golay et al[84].

### 3.2.2 Blood Oxygen Level Dependant (BOLD)

BOLD is similar to arterial spin labeling in that blood is used as an endogenous contrast agent. Although with BOLD the measured signal is based on the oxygenation level of the blood. It was first described by Ogawa[85],[86] and Ogawa & Lee[87] in 1990 in rat brain studies with high magnetic field strength. Ogawa & Lee noticed that the imaged blood vessels yielded negative contrast on high resolution MRI images. BOLD has since been further developed and in the following a brief introduction to the theoretical background is provided.

Oxygenated hemoglobin is diamagnetic while deoxygenated hemoglobin is slightly paramagnetic. The paramagnetic effects of the deoxygenated hemoglobin induces susceptibility differences between the blood vessels and surrounding tissue resulting in loss of signal in $T_2$* weighted MR sequences. Consequently, if the concentration of oxygenated blood changes, the MR signal will change[88].
BOLD is often used for brain activation studies as an indicator for neural activity. When the neurons are activated energy consumption increases and waste products accumulate yielding an increase in brain perfusion. Whether the increase in perfusion is because of lack of oxygen or because of accumulation of waste products is unclear. The increase in perfusion is larger than the increase in metabolism, effectively meaning that the percentage of blood which is deoxygenated while passing through the tissue (oxygen extraction fraction) is decreased. As a result, the blood in active areas of the brain contain relatively less deoxygenated blood which results in a net increase in signal from the tissue[88].

BOLD does not measure quantitative perfusion or quantitative changes in perfusion but indicate areas where perfusion changes after some form of stimulation e.g changes in activation of the brain.

## *3.3 Invasive methods*

As paramagnetic contrast agents shorten both $T_1$ and $T_2$* the effects of the

contrast agent can be quantified using either $T_2$* weighted imaging (dynamic susceptibility contrast) or $T_1$ weighted imaging (dynamic contrast enhanced). When the change in signal has been converted to contrast agent concentration, the processing of the dynamic data is equal for both methods. A brief introduction to acquisition and processing of both types of imaging and how perfusion can be quantified is provided in the following.

### 3.3.1 Dynamic Susceptibility Contrast (dSC)

Dynamic Susceptibility Contrast is often used to measure perfusion using MRI. A paramagnetic contrast agent is injected into a peripheral vein and the MR signal is measured as a function of time. The intravascular contrast agent introduces local inhomogeneities in the magnetic field leading to faster dephasing of the spins resulting in loss of signal.

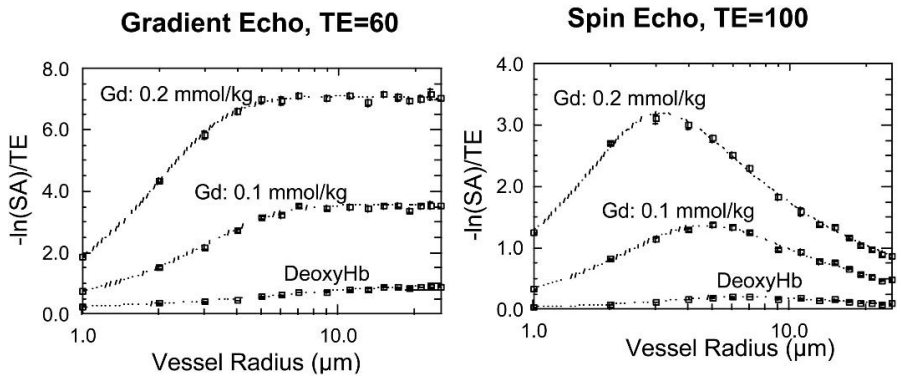


*Figure 3.1: The change in transverse relaxation rate as a function of vessel size for typical gadolinium dosages (single and double dose; 0.1 and 0.2 mmol/kg, respectively) and deoxyhemoglobin in spin echo (SE) and gradient echo (GE) sequences with typical TE values. Note the microvascular sensitivity of the SE sequence (in the range of capillary diameters), while GE sequences are equally sensitive to all vessel sizes. From Weisskoff*[90]

The first step in quantifying perfusion based on dSC is to convert the measured signal to contrast agent concentration. In most dSC studies it is assumed that the signal is approximately linearly related to the contrast agent concentration[89].

$$\Delta R_2(t) \propto C_t(t) \quad (3.1)$$

Both gradient echo (GE) and spin echo (SE) sequences have been used to measure perfusion. As seen in figure 3.1, SE sequences are primarily sensitive to capillaries while GE sequences are equally sensitive to all vessel sizes[90]. In addition, SE sequences require a larger dose of Gd-DTPA in order to get the same signal difference. For that reason GE sequences are typically used for measuring perfusion.

For a centric phase encoded spoiled gradient echo sequence the signal after injection of contrast agent can be expressed as[91]

$$S(t)=S_0\sin(\alpha)(1-e^{-TR\cdot(R_1+\Delta R_1(t))})\times e^{-TE\cdot(R_2+\Delta R_2(t))} \quad (3.2)$$

where S(t) is the signal as a function of time, $S_0$ is the signal before injection of contrast agent, TR the repetition time, TE the echo time, $\Delta R_1$ and $\Delta R_2$ are changes in the longitudinal and transversal relaxation times. In most cases $\Delta R_1$ is assumed to be very small and is omitted, but if the vessels in an area are permeable to the contrast agent, the extravascular contrast agent can have an effect on tissue R1 which will affect the measured signal. All vessels outside the brain are partly permeable to small contrast agents due to fenestrations in the vessels. Tumor vessels are extremely permeable due to big pores. In these regions, the contrast agent is able to enter the extracellular space resulting in an increased longitudinal relaxivity. This can increase the signal as seen in figure 3.2. Different solutions to this problem exist. In some cases the effects of extravascated contrast agent is modeled by modifying the acquisition[92], in other cases a predose of Gd-DTPA is given in order to reduce the $T_1$ shortening effects[93].

In manuscript II, a predose of Gd-DTPA was injected and the $\Delta R_1$ effects were therefore neglected. If $R_1$ and $R_2$ are assumed constant, equations 3.1 and 3.2 can be combined to give[89]

$$C_t(t)=-k\log(\frac{S(t)}{S_0})/TE \quad (3.3)$$

where k is a proportionality constant depending on a multitude of factors including the tissue, contrast agent (relaxivity), field strength and pulse sequence parameters. An example of a signal curve which is converted into a contrast agent concentration curve is shown in figure 3.2. Because of the k factor, quantitative perfusion measurements are impossible using $T_2$* bolus imaging. Some authors solve this problem by using a reference tissue e.g.

normal white matter which they assume have a known perfusion[89]. In other cases[93], such as in manuscript II, only relative blood flow and blood volume are reported, eliminating the need to estimate k.

As previously mentioned, a problem that still remains is that the relaxivity of the contrast agent, specifically its ability to affect $T_2$, is dependent on the tissue and vessel distribution[78].

A linear relationship between contrast agent concentration and signal decrease is often assumed as described in equation 3.1. As shown by van Oesch et al[94] this is not always the case for flowing blood. However, these effects can be eliminated by including phase information. Simonsen et al[95] showed linear relations *in vivo* though recent studies are questioning the validity of this linearity[96]. The manuscripts included in this thesis did not correct for non-linearities in the relation between signal intensity and contrast agent concentration.

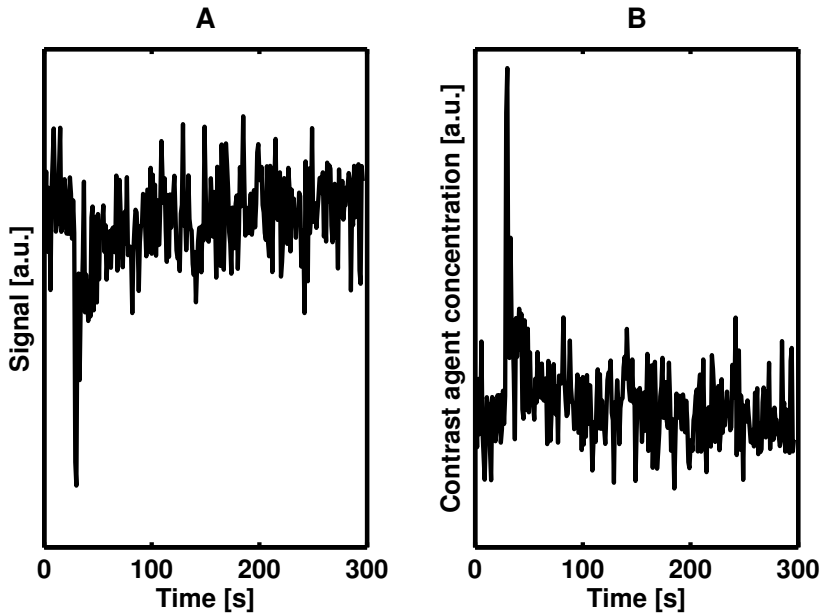


*Figure 3.2: Signal as a function of time for an artery is shown in A. The signal curve is converted to contrast agent concentration curve in B.*

In order to quantify perfusion an arterial input function is needed. Because of the swift changes in signal intensity in the arteries, a high temporal

resolution is needed to adequately sample the arterial input function. For humans, consensus is that the time between frames should maximally be a couple of seconds. However no such consensus exists for preclinical experiments. In clinical scanners, echo planar imaging (EPI) is typically employed allowing 10-15 slices to be acquired. On preclinical systems a spoiled flash sequence is typically used reducing the number of slices that can be acquired. We typically acquired one 2 mm slice with a time resolution of less than two seconds.

### 3.3.2 Dynamic contrast enhancement (dCE)

Dynamic contrast enhanced MRI has not been the method of choice for measuring perfusion. The is mainly due to limitations in time resolution and limited signal to noise in $T_1$W dynamic MRI scans. New technology (e.g. parallel imaging) has made it feasible to run dynamic MRI scans with a high temporal resolution while still acquiring adequate anatomical coverage in humans[97]. Because of the problems with obtaining $T_1$W images with high time resolution, $T_1$W measurements have classically been modeled using different kinetic modeling methods one of which will be described in section 3.4.4.

Perfusion has been measured using dCE employing many different methods. Unfortunately, there is currently no consensus for which method to use, hindering comparison of results between studies. A few studies have used inversion recovery acquisition, while most current studies use saturation recovery. For the purpose of this thesis, I will describe the steps involved in estimating perfusion based on a saturation recovery sequence.

For a saturation recovery sequence with centric phase encoding the signal equation can be written as follows[91]:

$$S(t) = S_0 \sin(\alpha)(1 - e^{-TD\cdot(R_1+\Delta R_1(t))}) \times e^{-TE\cdot(R_2+\Delta R_2(t))} \quad (3.4)$$

where $R_1$ and $R_2$ are reciprocal relaxation times before contrast injection, $\alpha$ is the flip angle and TD is the saturation delay. Usually $R_2$ is assumed constant and $\Delta R_2$ are omitted as a sequence with shortest possible echo time is used. $R_1$ can be fitted from a pre-contrast $R_1$ measurement with varying TDs. Because of noise, the subtraction might yield negative baseline values. The mean of the first few images (before contrast injection) is thus often subtracted from the time series data, eliminating the need to measure $R_1$. $S_0$

is sometimes omitted, assuming that the equilibrium magnetization is constant throughout the subject. This is not entirely true as $S_0$ depends on e.g. proton density and effective flip angle. In manuscript III of this thesis baseline subtraction was employed and the $S_0$ estimate from pre-contrast $R_1$ measurement was used in the signal equation.
If $R_2$ is assumed constant and $\Delta R_2$ is omitted, baseline is subtracted ($R_1$=0) and a linear relationship between contrast agent concentration and $\Delta R_1$ is assumed ($\Delta R_1 = r_1 C_t(t)$, where $r_1$ is longitudinal relaxivity of the contrast agent) then $C_t(t)$ can be found using the following equation:

$$C_t(t) \propto \frac{\Delta R_1}{r_1} = \left( -\log\left(1 - \frac{S(t)}{S_0 \cdot \sin\alpha}\right) \cdot \frac{1}{TD} \right) / r_1 \quad (3.5)$$

As every parameter is known and as the $T_1$ shortening effect is not affected by the orientation and structure of the vessels $C_t(t)$ can be accurately obtained using dCE MRI which makes it more feasible as a quantitative method than dSC MRI[60].

### 3.3.3 Arterial input function

For both dSC and dCE, obtaining a good arterial input function is of paramount importance. A short review of the problems in acquiring a precise arterial input function (AIF) and some solutions is presented in the following.

The arterial input function must be sampled adequately. In humans consensus is that the interval between images should maximally be a couple of seconds[89]. Because the bolus is dispersed and might be delayed while it traveling through the vasculature, the artery used to sample the AIF should be as close as possible to the tissue being imaged, e.g. in small vessels feeding the tumor instead of in a large vessel such as the descending aorta[98]. To obtain a good AIF close to the tissue of interest can be a challenge as the peripheral vessels are very small which can lead to partial volume effects. Calemente et al[99] solved the problem by using independent component analysis to automatically find local AIFs in the brain.

A delay of the of the $C_t(t)$ curve compared to the AIF will underestimate blood flow and overestimate mean transit time (MTT)[100]. The effects of delay can is easily eliminated by using block circulant

deconvolution[101] (method employed in manuscript II) or by shifting the time curve after finding the initial rise of contrast agent concentration. The dispersion effects are more difficult to correct for and requires vascular modeling[100].

Partial volume effects are difficult to avoid and can lead to either over- or underestimation of the AIF depending on the experimental conditions which may lead to over or underestimation of blood flow. Van Osch[102] et al published a paper on correction of the AIFs concluding that correction was possible for vessels that are aligned with the magnetic field.

The AIF for dSC images might be contaminated by $T_1$ effects while the AIF for dCE images might be contaminated by $T_2$* effects. Heilmann et al[103] developed a novel MR sequence in which $T_1$ and $T_2$* weighted images were acquired simultaneously making it possible to compensate for these effects. For dCE recent approaches has been dual echo[104,105] and combined $T_1$ and $T_2$* sequences[106,107] similar to the one Heilmann used to compensate for $T_2$* effects. The dSC sequence used in manuscript II was heavily $T_2$* weighted and no attempt to correct for $T_1$ effects were used except for administering a predose of contrast agent. The dCE sequence employed in manuscript III used the shortest possible echo time and a very small dose of contrast agent. Therefore $T_2$* contamination was assumed minimal.

## *3.4 Processing of dynamic MRI data*

As previously mentioned, the processing of dSC and dCE perfusion data is equal as soon as the MR signal has been converted to concentration of contrast agent over time. From the images an AIF is found either by automated methods or by manually selecting a pixel where the concentration of contrast agent increases rapidly and the concentration at the peak is high.

### 3.4.1 Blood volume

When both arterial and tissue concentrations have been acquired and no or little leakage of contrast agent is assumed, blood volume can be estimated as the ratio of the areas under the arterial and tissue time curves:

$$BV = \frac{\int_{-\infty}^{\infty} C_t(t)}{\int_{-\infty}^{\infty} C_a(t)} \quad (3.6)$$

If the arterial input function is not available, relative BV values can still be obtained by dividing the integrals of the tissue curves in the two areas.

When using the AIF recirculation of the contrast agent needs to be taken into account or incorrect estimates of blood volume may result. One solution is to fit the arterial curve with a gamma variate function to eliminate the recirculation part[108]. Another solution is to deconvolve the tissue curve with the arterial curve and use the integral of the deconvolved signal curve to determine BV instead[89]. This is often performed using singular value decomposition which will be introduced in the next section.

### 3.4.2 Blood flow

Consider an infinitely short lasting injection (delta function) giving arterial contrast agent concentration ($C_a$) at time 0. Tissue concentration as a function of time can then be formulated as[89]

$$C_t(t) = BF \cdot C_a \cdot R(t) \quad (3.7)$$

where BF is the blood flow and the residue function is termed R(t). R(t) describes the fraction of tracer in the vessel at time t after injection. R(0)=1 and R(∞)=0 assuming that the tracer is not bound and does not pool up in the tissue. The concentration of contrast agent is proportional to the amount of blood passing through the tissue per time unit.

In actuality, the contrast agent is injected into a peripheral vein and is not a delta function. It is broadened during the passage from vein to tissue and may be described as a sum of impulse response functions. Equation 3.7 then becomes a convolution[89]:

$$C_t(t) = BF \cdot C_a \otimes R(t) \quad (3.8)$$

In order to calculate BF from this equation, the impulse response must be found by deconvolution. Assuming that R(0)=1, BF is simply the first value of the impulse response while BV is the area under the deconvolved tissue curve. Due to noise, the deconvolution can be ill posed, meaning different solutions (different R(t)) exist for each pixel.

Deconvolution may be performed using different approaches. Most of these are model independent while others assume a specific shape of the residual function.

Model independent deconvolution - Fourier

One solution is to use the Fourier transform. The Fourier transform of two convolved functions equals the product of their separate transforms. This means that equation 3.8 can be solved as:

$$\begin{aligned} F\{BF\cdot R(t)\otimes C_a(t)\} &= F\{C_t(t)\}\Rightarrow \\ F\{BF\cdot R(t)\}\cdot F\{C_a(t)\} &= F\{C_t(t)\}\Rightarrow \\ BF\cdot R(t) &= F^{-1}\{\frac{F\{C_t(t)\}}{F\{C_a(t)\}}\} \end{aligned} \qquad (3.9)$$

where F{...} denotes the Fourier transform and $F^{-1}${...} denotes the inverse Fourier transform.

This approach is sensitive to noise and has problems with the discontinuity of the impulse response at t=0. There are ways of solving this[109,110], however the classical approach is to formulate equation 3.8 as a matrix equation.

Model independent deconvolution - SVD

If tissue and artery concentration is measured at equidistant time points, the tissue concentration can be discretized and changed to matrix formulation by:

$$C_t(t_j)=BF\int_0^{t_j} C_a(\tau)R(t_j-\tau)d\tau \approx BF\,\Delta t\sum_{i=0}^{j} C_a(t_i)R(t_j-t_i)$$

$$\begin{pmatrix} C_t(t_1) \\ C_t(t_2) \\ .. \\ C_t(t_N) \end{pmatrix} = BF\cdot\Delta t \begin{pmatrix} C_a(t_1) & 0 & .. & 0 \\ C_a(t_2) & C_a(t_1) & .. & 0 \\ .. & .. & .. & .. \\ C_a(t_N) & C_a(t_{N-1}) & .. & C_a(t_1) \end{pmatrix} . \begin{pmatrix} R(t_1) \\ R(t_2) \\ .. \\ R(t_N) \end{pmatrix} \qquad (3.10)$$

This is a standard equation and it is often solved by singular value decomposition. One disadvantage of the original SVD approach is that it tends to underestimate flow if the arterial input function and tissue curve are not well aligned. The structure of the vessels or pathology can cause a delay in the arrival of the bolus to the tissue. However this issue has been solved

by using block circulant SVD[111]. Using this method, the arterial curve is padded with zeros and shifted as shown below.

$$\begin{pmatrix} C_t(t_1) \\ C_t(t_2) \\ .. \\ .. \\ .. \\ C_t(t_N) \end{pmatrix} = BF \cdot \Delta t \begin{pmatrix} C_a(t_1) & 0 & 0 & 0 & 0 & C_a(t_N) & .. & C_a(t_2) \\ C_a(t_2) & C_a(t_1) & 0 & 0 & 0 & 0 & C_a(t_N) & .. \\ .. & C_a(t_2) & C_a(t_1) & 0 & 0 & 0 & 0 & C_a(t_N) \\ C_a(t_N) & .. & C_a(t_2) & C_a(t_1) & 0 & 0 & 0 & 0 \\ 0 & C_a(t_N) & .. & C_a(t_2) & C_a(t_1) & 0 & 0 & 0 \\ 0 & 0 & C_a(t_N) & .. & C_a(t_2) & C_a(t_1) & 0 & 0 \\ 0 & 0 & 0 & C_a(t_N) & .. & C_a(t_2) & C_a(t_1) & 0 \\ 0 & 0 & 0 & 0 & C_a(t_N) & .. & C_a(t_2) & C_a(t_1) \end{pmatrix} \begin{pmatrix} R(t_1) \\ R(t_2) \\ .. \\ R(t_N) \\ 0 \\ 0 \\ 0 \\ 0 \end{pmatrix} \quad (3.11)$$

This makes the SVD insensitive to delays between artery and tissue curves. Even tissue curves that come before the arterial input function are fitted correctly.

If the above equations are expressed as $\mathbf{c}=\mathbf{A}\cdot\mathbf{b}$ they can be solved for **b** (the elements of R(t) scaled by BF). By decomposing $\mathbf{A} = \mathbf{U} \cdot \mathbf{S} \cdot \mathbf{V}^T$, where **U** and **V** are orthogonal matrices and **S** is a nonnegative square diagonal matrix, the inverse can be expressed as $\mathbf{A}^{-1}=\mathbf{V}\cdot\mathbf{W}\cdot\mathbf{U}^T$, where **W** = 1/**S** along the diagonals and zero elsewhere. Values of **W** where **S** is less than a preset tolerance are set to zero to reduce oscillations (this method is also called truncated SVD - TSVD[112]). The residue function scaled by BF, **b** can be estimated by $\mathbf{b} = BF\ \mathbf{V}\cdot\mathbf{W}\cdot\mathbf{U}^t\cdot\mathbf{c}$. BF is estimated as the maximum value of **b**. The discontinuities at the beginning and end can give rise to amplification of leakage frequencies, which may give oscillations in the deconvolved signal. This problem can be solved by decreasing the tolerance or using an oscillation index and varying the tolerance until the oscillation index falls below a certain value[113].

In manuscript II, block circulant deconvolution was used with a preset tolerance which was the same for all pixels. Smith et al have shown that inverse Fourier transform and SVD provide equal results as long as the delay between the AIF and the tissue curve is not too severe[110]. Smith used classic deconvolution, however in manuscript II, block circulant deconvolution has been used, which should compensate for delays.

Model independent deconvolution – Tikhonov regularization

Tikhonov regularization is a well known and very common form of regularization[112,114]. It adds a side constraint ($\lambda^2\|\mathbf{L}b\|^2$, where **L** is a matrix and ‖ indicate vector norm) to stabilize the solution of an ill-posed problem.

L is chosen based on priori information (for example that the residue function should be smooth) and the Lagrange multiplier λ or the regularization parameter must be optimized. Instead of solving the original problem (by minimizing ||**A**·b – c||) an alternative more stable problem, is solved by minimizing a weighted combination of the residual norm and the side constraint.

$$b_\lambda = min\{||\mathbf{A}\cdot b - c||+\lambda^2||\mathbf{L}\cdot b||^2\} \quad (3.12)$$

The matrix **L** introduces a penalty if the solution b behaves in an undesirable way based on the a priori condition used. Various forms of **L** have been proposed but most commonly the first order difference operator ($\mathbf{L}_1$) is used to reduce oscilation[112,115]:

$$\mathbf{L}_1 = \begin{pmatrix} -1 & 1 & 0 & 0 & 0 \\ 0 & -1 & 1 & 0 & 0 \\ 0 & 0 & \ddots & \ddots & 0 \\ 0 & 0 & 0 & -1 & 1 \end{pmatrix} \quad (3.13)$$

The $\mathbf{L}_1$ has a tendency to overregularize dispersed residua functions too much, hence Calemente et al suggested a modified $\mathbf{L}_1$ matrix[116], that reduces the regularization of a number of initial points.

The key for optimal regularization is then to select the optimum regularization value λ. One of the simplest and most popular ways of doing so is to find the corner of the L-curve[112]. The L-curve plots the trade off between minimizing the residual norm ||**A**·b – c|| and the constraint norm ||**L**b||. When plotted on a log-log scale this curve usually has a distinct L-shape as shown in figure 3.3. At small λ values, the solution is dominated by the perturbation error in the vector c. The residual norm is small but the solution semi-norm varies dramatically (due to division by small singular values). This corresponds to the vertical part of the L-curve. At high λ values, the solution is dominated by the regularization error and ||**L**b|| changes little with λ. However, the data misfit (the residual norm) increases heavily. This corresponds to the horizontal part of the L-curve. It has been shown that the corner of the L-curve (found as the point in the L-curve with maximum curvature) gives an acceptable compromise between data misfit and regularization[112].

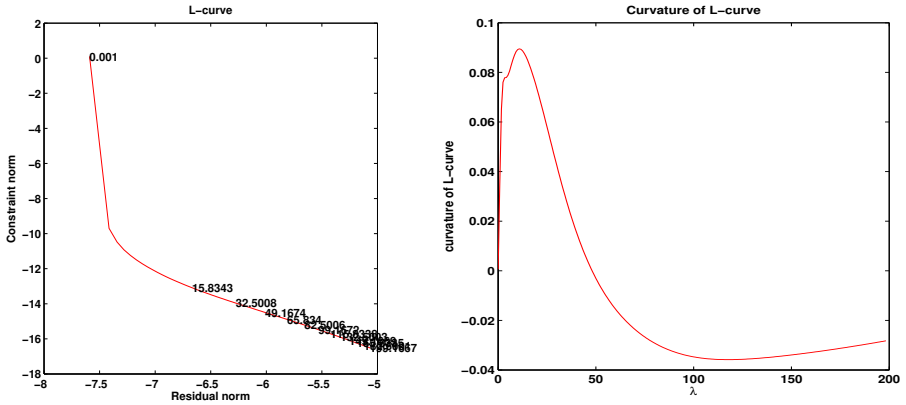


*Figure 3.3: Left: Log of residual norm plotted against log of the constraint norm for different λ values (0-200) for a ROI in manuscript 3. Numbers along the curve are the λ values. Right: Curvature of the L-curve. Optimal λ is selected as the maximum of the curvature and corresponds to the corner of the L-curve.*

The Tikhonov regularization with automatic selection of λ value based on the L-curve method was used in Manuscript III to minimize the effects of noise in the deconvolution.

Other model independent deconvolution methods

A statistical approach in which the kernel (residue function in formula 3.8) is optimized using a maximum likelihood approach has been suggested by Vonken et al[117]. In another approach Andersen et al used a Gaussian process to approximate the convolution kernel[118].

Model dependent approaches

The deconvolution techniques described do not make assumptions of vascular structure. Alternative methods exist which model tracer transport and retention. One possibility is to assume an exponential residue model by assuming that the microvasculature acts like a well-mixed compartment yielding an exponential residue function[119]. Most of the residue functions found by deconvolution appear to be mono-exponential but pathology or multiple compartments can change this which may lead to erroneous results.

### 3.4.3 Mean transit time

When blood flow and blood volume has been determined the mean time the tracer takes to traverse the vasculature can be calculated using the central volume theorem[120]:

MTT = BV / BF (3.14)

### 3.4.4 Vascular leakage (Patlaks method)

As previously described, tumor vessels are immature and have large gaps. This makes tumor vessels very permeable to contrast agents. The rate of leakage can be estimated, using a method which was formulated by Patlak et al in the 80s. The method has one critical simplifying assumption, namely that there is an 'irreversible' tissue region outside the vasculature, where the tracer is trapped for the duration of the experiment[121,122]. The working equation for this system is:

$$C_t(t) = K_i \int_0^t C_p(\tau)\,d\tau + v_d C_p(t) + v_a C_p(t) \quad (3.15)$$

where $C_p$ and $C_t$ are plasma and tissue concentrations, $K_i$ is the unidirectional transfer constant from vessel to interstitial fluid, $v_d$ is the fractional volume of plasma tracking tissue space and $v_a$ is the fractional volume of the plasma. Since $v_a$ and $v_d$ cannot be separated from the data they will be combined to $v_D$ ($V_D=V_d+V_a$).

Patlak et al linearized the problem as follows:

$$C_t(t) = K_i \int_0^t C_p(\tau)\,d\tau + v_D C_p(t) \Rightarrow$$

$$\frac{C_t(t)}{C_p(t)} = K_i \frac{\int_0^t C_p(\tau)\,d\tau}{C_p(t)} + V_D \quad (3.16)$$

By plotting $\frac{C_t(t)}{C_p(t)}$ against $\frac{\int_0^t C_p(\tau)\,d\tau}{C_p(t)}$ a linear plot is obtained (if the assumptions of the model are fulfilled) where the slope is $K_i$ and the y-

intercept is $V_D$. The x-axis of this plot is called 'stretch time'. In a later work[122] Patlak generalized the model to include effects of efflux from the 'irreversible' tissue compartment back into blood.

$$C_t(t) = K_i \int_0^t e^{-k_b(t-\tau)} C_p(\tau) d\tau + v_D C_p(t) \quad (3.17)$$

This is equivalent to the consensus model proposed by Tofts et al in 1999[123].

Ewing et al[124] tested three different models: no leakage, unidirectional leakage (3.16), and bidirectional leakage (3.17) in a 9L glioma model. They found the bidirectional leakage model to fit the data more correctly inside the tumor and that the unidirectional leakage model tended to overestimate $V_D$ and underestimate $K_i$. Correlation was nevertheless found between the $K_i$ obtained with the two models. For the early time points (up to 7.5 minutes), similar $K_i$ and $V_d$ were found. In manuscript III the original unidirectional Patlak method was applied resulting in good linearity in the timespan (10 min) we measured. However Ewing employed a different tumor model (9L glioma) using a macromolecular contrast agent (MMCM – Gadomer). Results may thus not be comparable.

## 3.5 Curvology

In some works no attempt is made to quantify perfusion or other parameters. Instead description of the shape of the MR signal curve is used to extract parameters related to pathology. This method has been termed curvology. Parameters extracted can be the arrival time (time from injection to signal starts to drop/increase), time to peak (time from bolus arrives till it reaches maximum value) and full width half maximum of the peak[89]. In a study by Brandt et al[125], in which the author was involved, this form of processing was employed in order to identify areas with blood brain barrier breakdown in meningitis. This was obtained by identifying pixels in which signal increased above a threshold. It was possible to distinguish rats treated with antibody from untreated rats as well as early from late infection.

# Chapter 4 Monitoring angiogenesis using MRI

In this chapter I will introduce the various methods which can be exploited to monitor angiogenesis using MRI. This overview is based on the excellent reviews by Barrett[126], Bhujwalla[59] and Padhani[60]. I have aimed to highlight the most important findings listed in these papers and relevant connections to the manuscripts published in this thesis.

## *4.1 Introduction*

Angiogenesis may be monitored multiple ways. One option would be to monitor circulating blood levels of angiogenic factors (e.g. VEGF) or circulating endothelial stem cells. Currently, measuring VEGF is not sensitive or specific enough. However, a study has shown correlation between circulating endothelial stem cells and treatment response[127].

The ”gold-standard” measurement of angiogenesis is the microsvascular density (MVD) quantifying the average number of microvessels within a microscopic field. This method does not indicate whether vessels are functional or hyperpermeable. Furthermore, it is invasive and biased according to where the sample is taken. As previously mentioned, tumors are very heterogeneous and angiogenesis is primarily present in the periphery. Imaging modalities can provide non-invasive means of detecting angiogenesis in the whole tumor. The ability to monitor angiogenesis non-

invasively over time allows treatment to be monitored and early detection of drug efficacy before size changes of the tumor are apparent. Furthermore, non-responding tumors can be identified and medical treatment revised.

Many modalities are able to provide information about vascular state including MRI, computed tomography (CT), positron emission tomography (PET), single photon emission-computed tomography (SPECT), ultrasound, and optical imaging. CT, PET and SPECT expose the patient to ionizing radiation making longitudinal monitoring problematic. CT provides high quality images with a high spatial resolution and gives a signal directly proportional to density facilitating easy processing. PET can provide noninvasive tumor perfusion estimates using $^{15}O$ labeled water but the modality requires a cyclotron on site because of the short half life of $^{15}O$ (minutes). PET and SPECT can measure radio-tracers at picomolar concentration. However, few tracers exist and at best they provide low spatial resolution[128]. There is ongoing development in this field but none of the new angiogenic agents are available clinically.

Ultrasound is safe for the patient but very operator dependent. Progress is being made with targeted micro bubbles as contrast agent[129].Being a couple of microns in diameter, they stay confined within the vasculature and hence give good measures of perfusion and blood volume but no indication of leakiness. Optical imaging is of limited use since the modality is only able to penetrate a few centimeters below the skin surface.
In light of these observations MRI stands out by not employing radiation exposure, being able to assess tumor size and stage, and offering multiple weightings in one single session. Information can be obtained with or without contrast agents as will be described in the following.

## *4.2 Noninvasive methods*

### 4.2.1 Arterial spin labeling (ASL)

ASL provides regional maps of blood flow which has been suggested as a marker for the degree of neovascularization within tumors due to the increased size and number of vessels. ASL could thereby provide a noninvasive way of monitoring angiogenesis indirectly by measuring blood flow and the method has been used to measure blood flow in brain

tumors[130]. Kimura et al[131] showed significant correlation between ASL signal intensity change and microvessel area from histology. ASL has also been used to measure blood flow as an outcome parameter in a 9L gliosarcoma rat model with differences in VEGF expression[132].

ASL has been utilized in many areas of the body e.g. showing vascular remodeling and angiogenesis within the ovary during the menstrual cycle[133]. Also renal cell carcinomas have been assessed. Boss et al[134] showed that the use of ASL was equivalent to contrast enhanced $T_1$ images for monitoring tumor recurrence following radio ablation therapy.

### 4.2.2 Blood Oxygen Level Dependent (BOLD)

BOLD has most widely been used for brain activation studies in which a specific task is performed and changes in the BOLD signal is used to indicate which areas of the brain are active during the performed task.

Applying BOLD methods to tumors is more difficult. In order to induce a change in the deoxy/oxyhemoglobin ratio, cancer studies use either inhaled 100% oxygen or carbogen (95% oxygen, 5% CO2) as a challenging method[135]. Though BOLD relies on the amount of signal produced by oxyhemoglobin there is a complex interaction between changes in blood volume, blood flow and tissue oxygen consumption rate. Most of the BOLD techniques compare signal before and after inhalation of a gas, however the BOLD response to carbogen is complex and its relationship to angiogenesis is not always clear. The effects of carbogen not only changes blood oxygenation but also causes blood vessels to dilate (increased CO2) increasing blood flow. There are different mechanisms that may increase the BOLD signal, including increased oxygenation or decreased deoxyhemoglobin due to increased flow. Blood flow can be estimated as it leads to decreased oxygen extraction from the tissue but it is difficult to distinguish this from reversible hypoxia. One solution is to use an alternative method for monitoring flow e.g. Doppler ultrasound. Alternatively, $T_2$* maps can be generated and kinetic modeling can be used to estimate the contributions of flow and deoxyhemoglobin[136].

Carbogen-BOLD has been used to study angiogensis in xenografted ovarian tumors at different stages[137], where BOLD was shown to map the heterogeneity of mature vessels in the tumor. In another study[138] BOLD was

able to predict vascular maturation by measuring the degree of reaction to induced hypercapnia. BOLD has also been used to monitor the efficacy of radio sensitizing tumors by increasing oxygenation prior to radiotherapy[136]. BOLD has been shown to be more rapidly reversible than contrast enhanced MRI, making it suitable for monitoring vascular disruptive treatments[139].

BOLD imaging has been used in many angiogenesis studies. Though an injection of contrast agent is not required, most studies use inhalation of carbogen gas mixtures which may not be available in a clinical setting and may cause patient discomfort. Reproducibility using this method is limited, but BOLD has great potential for monitoring areas of oxygenation within tumors.

## 4.3 Invasive methods

The vasculature within tumors is very heterogeneous. While some vessels have a high degree of maturity others have incomplete layers and show high permeability. Angiogenic vessels have gaps between endothelial cells, the endothelium and the basement membrane, making them hyper permeable to macromolecules[36]. This can be exploited using contrast enhanced MRI. Contrast agents that leak slowly through normal vasculature will quickly leak out of tumor vessels and give rise to differential enhancement. Dynamic contrast enhanced (dCE) MRI can be performed either using low molecular weight contrast media or high molecular weight contrast media. Gd-DTPA is the most widely used low molecular weight contrast agent.

As there are a multitude of ways to analyze dCE MRI scans, details will not be provided. However these methods can be categorized based on the size of the agents used and their specialization (e.g. specific binding). In general studies examining leakage parameters are based on $T_1$W imaging while studies investigating blood volume and perfusion are based on $T_2$*W imaging[60]. Recent developments in pulse sequences allow for rapid acquisition of $T_1$W images enabling quantification of blood volume and flow as well as leakage and distribution volume. This type of method was used in manuscript III where perfusion and leakage parameters were extracted from a single $T_1$W dynamic scan.

In the following $T_1$W imaging has been used unless explicitly stated otherwise.

### 4.3.1 Dynamic MRI with low molecular weight contrast agents

Following data acquisition, kinetic models can be applied to derive estimates of tissue perfusion and permeability based on the dynamic time curves.

dCE MRI parameters have been shown to correlate with vascular permeability within tumor tissue[97]. The technique has also been used to demonstrate the effect of anti-angiogenic drugs and can be used for early detection of treatment response. Morzola et[140] al showed decreased vessel permeability 24 hours after treatment using a drug targeting VEGF, FGF and PDGF (platelet derived growth factor) receptors. Wadam et al[141] showed a reduction in permeability and extracellular volume in patients with invasive breast cancer after injection of a VEGF antibody. Successful results have also been obtained with PTK/ZK, a VEGF receptor inhibitor acting on three separate VEGF receptors. Response to treatment has been shown as early as two days after treatment either by permeability parameters or initial area under the curve[142,143].

The effects of thalidomide in combination with carboplatin has been evaluated using $T_2$*W dynamic MRI and results were correlated to clinical status[144]. This research group also showed correlation between rCBV maps obtained using $T_2$*W bolus imaging and MVD[145]. Some $T_1$W studies have also shown correlation between dynamic parameters and MVD[146,147,148] while others have not[149,150]. VEGF expression and permeability have been shown to correlate by Knopp et al[151] though other groups have shown no correlation[149,152].

The results from animal studies can be used to guide the timings of DCE MRI in phase 1 studies. Galbraith et al used preclinical studies of the effects of Combretastatin to select the most optimal time point to monitor treatment in patients[153]. Other studies showed that anti-VEGF treatment can change micro vessel permeability as early as 90 min after first dose[154,155] although anti-VEGF drugs are thought to act over a much longer period. This information was later used to design human studies.

There is still a lack of consensus concerning what kinetic model should be used for analyzing dynamic MRI studies. However, DCE MRI seems to be the imaging technique of choice for monitoring clinical response in anti-angiogenic and antivascular trials.

### 4.3.2 Dynamic MRI with macromolecular weight contrast agents

Macromolecular contrast agents (MMCM) are in the range of 5-90 kDA and include both gadolinium and iron oxide based agents. They were originally designed for prolonged intravascular retention for use in MR angiography. The agents do not pass through normal endothelium and are more selective for pathological vasculature.

The increased size compared to the low molecular weight agents, yield different pharmacokinetics. Because low molecular weight contrast agents are freely diffusible, their estimates of permeability will be affected by the blood flow while MMCMs are minimally diffusible tracers reflecting permeability with a minimal flow contamination. MMCMs are ideal blood pool agents and can give a more accurate estimate of tumor blood volume. The leakiness ($K_i$) of MMCMs is inversely related to their molecular weight (mW). A doubling of the mW leads to a 25% decrease in $K_i$. Obviously the diameter of the molecules rather than their weight is important but generally weight and diameter follow each other.

Albumin-Gd (Albumin-(Gd-DTPA)) is a widely used MMCM in which Gd-DTPA is bound to albumin. The main problem is to obtain strong complex binding between $Gd^{3+}$ and albumin, allowing no free toxic gadolinium. This has been solved by using bifunctional chelates that link albumin to $Gd^{3+}$ with high binding affinity[156].

MS325 (or vasovist) is an agent which *reversibly* binds albumin. In humans it is bound to albumin with good affinity (approx 96% bound) [157] but the percentage bound decreases a lot in rats (76%) and mice (67%). Thus, the injected MS325 becomes a mixture of a blood pool agent and unbound Gd-DTPA limiting usability. However, the non specific binding does help to clear the compound from the body rapidly reducing the risk of toxicity from the gadolinium. The use of MS325 for angiogenesis imaging has yet to be tested in humans. Turetschek et al[158] have compared MS325 to albumin-Gd in a breast cancer model in mice but found no correlation between MS325 and MVD or tumor grade. Different results may be obtained in humans where the binding affinity is higher.

Albumin-Gd has been used to characterize microvessels in a wide range of tumors. Marzola et al[159] showed that Albumin-Gd correlates with MVD and immunhistochemistry and that it is similar to low molecular weight

dynamic MRI after treatment with VEGF inhibitors. Pham et al[154] showed large reduction in permeability and unchanged plasma volume in breast tumors after administration of an anti-VEGF antibody.

Another option for MMCM is liposomes in which a hydrophilic interior is surrounded by one or more phospholipid bilayers. They can incorporate either Gd or iron particles and are preferentially taken up by liver and spleen. Animal trials have shown good potential for imaging metastatic lymph nodes. Unfortunately it is very difficult to produce liposomes in uniform sizes.

Yet another class of MMCMs is dendrimers. These are synthetically produced, highly branched, spherical polymers which can be produced in uniform sizes. Dendrimers with sizes from 5-8 nm in diameter are able to selectively leak through hyperpermeable tumor vessels while larger dendrimer based agents demonstrate vascular enhancement with minimal leakage. They have been used to demonstrate early effects of radiation therapy on tumor permeability[160].

### 4.3.3 Iron containing MMCM

Iron oxide particles exist in various sizes and are often used as MMCM agents. To avoid aggregation of the agents a dextran coat is most often employed. Iron oxides are super paramagnetic predominantly shortenening $T_2$*. However, $T_1$ relaxation effects are also present. SPIO particles are are mainly degraded by phagocytic cells while USPIO are taken up more slowly.

USPIOs have been used to monitor angiogenesis in murine breast cancer models where $K_i$ showed correlation with tumor grade and histological MVD[161,162] using a $T_1$W method. Similar correlation was found in a colon carcinoma model[163]. Pathak[164] et al showed correlation between MVD and dSC MRI after administration of an iron containing MMCM using $T_2$*W determination of blood volume.

In manuscript I the SPIO Ferridex was used to quantify angiogenesis in matrigel chambers showing good correlation with an optical method.

### 4.3.4 Stem cells and targeted agents

As endothelial stem cells are thought to be involved in angiogenesis another approach is to label these and track their behavior. Even single cells may be detectable if labeled with iron oxide particles[165]. Anderson et al[166] injected labeled endothelial precursor cells and showed that they localized to the angiogenic portions of a tumor using $T_2$W imaging.

Ideally an MR contrast agent would target specific molecular markers present on angiogenic blood vessels. Many such markers are already known and some are being utilized in MRI. One advantage is that these markers are directly available to the blood enabling efficient delivery. The main problem for MRI is the low number of targets compared to the signal from unbound agent inside the vessels[167]. Thus, the binding has to be very specific and the elimination of unbound agent swift. Because of the low number of binding sites the MR sequences used to detect the agent have to be sensitive to small changes in the signal making PET and SPECT the more likely candidates for this type of detection. However Winter et al[168] selectively targeted an integrin associated with angiogenesis increasing signal in tumors by 126% predominately in the periphery. Mulder et al[169] used targeted liposomes and demonstrated signal enhancement in activated tumor endothelium. MRI targeted imaging may have limited usability at present but larger and more potent macromolecular contrast agents are under development which could increase sensitivity. Furthermore specialized coils and increased field strength may also contribute.

# Chapter 5 Aims

As previously described, angiogenesis is important in many kinds of pathologies as well as some normal biological processes. In this thesis, the main focus has been on angiogenesis in cancer.

The main aim has been to develop methods for monitoring the status, development, and consequences of tumor angiogenesis.

More specifically, the sub-aims were:

- To develop a technique to detect the development of angiogenesis and to quantify the effects of treatment using anti-angiogenic drugs on initial stages of angiogenesis.
- To enable monitoring the status of angiogenesis using MRI, in particular, measuring perfusion as well as tumor vessel permeability. This would enable studying the effects of treatment with anti-angiogenic drugs as well as to evaluating the efficacy of new drugs. Furthermore, methods for evaluating treatment response could be the result of such a method.
- To develop methods for optimizing the timing between treatment with anti-angiogenic agents and chemotherapy. It is well known that a 'normalization' window exist in which tumor vasculature becomes less permeable and perfusion increases after treatment which is why timing may be critical.

- To label cells using a contrast agent in order to permit the tracking of metastasis present due to angiogenesis in cancer. Most cell labeling methods rely on labeling cells *ex vivo.* However, for a transgenic tumor model (such as the one used in manuscript III) *ex vivo* labeling is not possible. Therefore, a further sub-aim was to develop *in vivo* cell labeling.

In the following a brief introduction to each manuscript will be given followed by revisiting the aims describing what was learned and what the future perspectives could be.

## *5.1 Manuscript I - In vivo angiogenesis assayed using MRI*

### 5.1.1 Summary

In this study, plexiglas cylinders were filled with Matrigel containing proangiogenic agents (VEGF and bFGF) and surgically implanted subcutaneously in nude mice. The mice were divided into two groups. One group was treated with 200 mg/kg Thalidomide daily (N=9, while the other group (N=11) acted as controls.

Twelve days after implantation the mice were scanned using MRI. Bolus passage of an SPIO (Endorem) was followed using a $T_2$* weighted dynamic sequence. In addition, pre- and post-contrast T2 maps were obtained using a multi-readout spin echo sequence. After MRI, the animals were sacrificed and the Matrigel chambers were imaged optically. Neovascularization was quantified by automatic detection of red pixels.

Good correlation between the change in $T_2$* and the optical method was found (P=0.005) validating the MRI method. Significant differences in vascularization were found between the Thalidomide and control group using both optical and MR methods.

### 5.1.2 Aims revisited

This study validated the possibility of monitoring initial development of angiogenesis *in vivo* and demonstrated that the effects of treatment could be quantified. In the future, this method may be used to study the effects of

new anti-angiogenic drugs. Compared to conventional methods, the MRI method allows for repeated measurements in each animal reducing the sample size necessary to obtain significant results. The MRI method could be used to investigate synergistic effects of chemotherapy combined with anti-angiogenic treatment and the optimal timing between treatments. One such example would be studying the uptake of a chemotherapeutic drug using e.g. $^{19}F$ or $^{13}C$ spectroscopy.

## *5.2 Manuscript II - Perfusion in brain tumors*

### 5.2.1 Summary

A partly intact blood brain barrier (BBB) or blood to tumor barrier can limit drug delivery to tumors. Therefore, this study evaluated $^{13}C$ spectroscopy as a method to detect chemotherapeutic drug ($^{13}C$ labeled temozolomide TMZ) uptake in a brain tumor model. Though TMZ was injected intra-peritoneally, it is delivered to the brain through the vasculature. In order to verify that it would be possible to deliver TMZ to the tumors, dynamic susceptibility contrast measurements were performed and relative blood volume and perfusion maps were obtained.

The perfusion measurements showed increased blood volume and perfusion in tumors compared to normal tissue, verifying that delivery of TMZ through the blood is possible. Because of selective BBB breakdown at the tumor site it was possible to qualitatively detect vascular permeability. This was achieved by subtraction of pre- and post-contrast $T_1$ measurements. Phantom experiments showed that it was possible to detect 100 µM TMZ *in vitro.* Finally $^{13}C$ TMZ was successfully detected in U87 brain tumor *in vivo.*

### 5.2.2 Aims revisited

While the primary goal of this study was to detect TMZ *in vivo,* dynamic MRI was used to verify that drug delivery could take place fulfilling the second sub-aim. Furthermore, qualitative estimates of vascular permeability were used as a sign of neovascularization. As previously described, the timing between administration of anti-angiogenic agents and chemotherapy may be critical and a model such as this would be ideally suited to follow

both drug uptake and vascular development after treatment.

## 5.3 Manuscript III - dCE MRI of breast tumors

### 5.3.1 Summary

In this study two different tumor stages were followed in a transgenic tumor model. The main advantage of using a transgenic model is that tumors form spontaneously mimicking the behavior of tumors in patients more than xenografted tumors. The PyMT model is ideal for studying angiogenesis as each tumor evolves through four different phases which have been described extensively. Two groups of mice were studied. One group was scanned in the hyperplastic stage (N=4) and another in the late tumor stage (N=4). Dynamic Contrast Enhanced MRI (dCE) was used to quantify both perfusion and permeability of the vessels.

All tumors were well perfused. Significant differences in the time it takes the contrast agent to traverse the vasculature (Mean Transit Time – MTT) were found between tumors and reference tissue as well as between the hyperplastic and late tumor stage. Vascular permeability and blood volume were decreased in late stage tumors compared to hyperplastic stage. The changes in permeability, blood volume, and MTT were speculated to be caused by maturation of the tumor vessels.

### 5.3.2 Aims revisited

This study was directly associated with the sub-aim of being able to monitor status of angiogenesis. The study showed significant differences in the vasculature of tumors at different stages. The methods employed in the study would be suitable for studying the effects of treatment with anti-angiogenic drugs and evaluating the efficacy of new drugs. Furthermore, the vascular effects of conventional therapy (e.g. chemotherapeutics or radiation) could be studied. In the future, the method should be validated using histology. It could prove of interest to combine this method with methods for detecting drug delivery (e.g. $^{19}F$ or $^{13}C$ spectroscopy).

## 5.4 Manuscript IV – In vivo cell labeling

### 5.4.1 Summary

In this study, the use of electroporation for *in vivo* cell labeling was evaluated. In order to verify the method, muscles in the hindleg of rats were electroporated after administration of either saline (n=5), Magnevist (n=4) or Gadovist (n=9). The concentration of contrast agent and the effects of electroporation were followed using $^1$H spectroscopy for up to 2 months after electroporation. $T_1$ of choline, creatine, lipid, and water were measured and relaxivity measurements were used to estimate the concentration of contrast agent. Furthermore, pesudo-concentrations of each metabolite over time were obtained.

Results showed significant reduction of $T_1$s for choline, creatine and water confirming that the contrast agent was internalized. The initial intracellular concentration of contrast agent was up to 1 mM. Contrast agent concentration decreased exponentially over time and seemed to reach a plateau value of approximately 0.2 mM. The $T_1$ values of metabolites and water were decreased up to 2 months after electroporation. The pseudo-concentration of choline and creatine was shown to be significantly decreased in electroporated compared to non-electroporated animals which would be consistent with tissue damage. Furthermore, $T_1$ of the saline electroporated animals was significantly higher than the control animals for the first couple of weeks following electroporation which is indicative of edema. The contrast agents are delivered into the cytoplasm via electroporation. Consequently, the study also shows that the choline and creatine resonances originate from metabolites within the cytoplasm since the contrast agents and metabolites must be in the same compartment to produce the observed relaxation effects

### 5.4.2 Aims revisited

This study has shown the feasibility of labeling cells *in vivo* using electroporation and that the labeling was detectable up to 2 months after electroporation. Therefore, *in vivo* cell labeling could be a feasible way of monitoring e.g. metastatic spread of cancer cells. However, the method still needs to be verified in tumors rather than the muscle cells labeled in this

study. Further, the muscle cells were non-dividing while in a growing tumor cells will divide diluting the contrast agent which in turn could lead to loss of labeling. However, the initial concentration of contrast agent (approx 1mM) is significantly higher than the detection limit for free Gd-DTPA 0.05mM[170] meaning that significant dilution can find place without loss of signal.

Electroporation was shown to have cellular effects (edema and metabolite depletion), which might affect the tumor cells more than the muscle cells and also contribute to the observed anti-cancer effects of electroporation. However, a recent study has used electroporation to deliver anti-vascular drugs to mouse breast tumors[171].

Apart from cell labeling, this approach could provide additional insight into the effects of contrast agents. Cells labeled using this method already have a high susceptibility which would limit the T2* effects of an injected Gd-DTPA bolus enabling studies of contrast agent properties and the use of higher contrast agent concentrations.

## 5.5 Conclusion

In this thesis several ways of monitoring angiogenesis have been used. Matrigel chambers were used to study initial development of angiogenesis and the effect of treatment with the anti-angiogenic drug Thalidomide. Using two separate perfusion measurement methods, the status of angiogenesis was monitored in U87 gliomas as well as in a transgenic mammary cancer model. Furthermore, delivery of the 13C labeled chemotherapeutic drug Temozolomide to U87 tumors was quantified using spectroscopy. Finally, a method for *in vivo* cell labeling using electroporation was developed. The cellular effects of electroporation as well as the persistence of the labeling were evaluated. These results indicate that the method may be of use in studying metastatic spread of cancer cells, although this has yet to be tested.

Most of the initial aims of this thesis were fulfilled. Future studies, based on the developed methods, should investigate the optimal timing between anti-angiogenic treatment and chemotherapy. Furthermore, the study of effects and efficacy of new anti-angiogenic agents have been enabled with the presented techniques. In addition, it would be very interesting to correlate

vascular parameters extracted using dynamic MRI with histology.

In this thesis several ways of monitoring angiogenesis and anti-angiogenic treatment have been developed. These methods could be used to gather further insight into the angiogenic process. Furthermore new forms of treatment can be evaluated, ultimately leading to patient benefit.

# References


1. Goldmann, E. The growth of malignant disease in man and the lower animals, with special reference to the vascular system. *Proc R Soc Med* 1-13(1907).
2. Algire, G. et al. Vascular reactions of normal and malignant tissues in vivo. I. Vascular reactions of mice to wounds and to normal and neoplastic transplants. *J Natl Cancer INst* **6**, 73-85(1945).
3. Jacobs, J. Combating cardiovascular disease with angiogenic therapy. *Drug Discovery Today* **12**, 1040-1045(2007).
4. Fan, Y. & Yang, G. Therapeutic Angiogenesis for Brain Ischemia: A Brief Review. *Journal of Neuroimmune Pharmacology* **2**, 284-289(2007).
5. Dhanabal, M. & Sethuraman, N. Endogenous angiogenesis inhibitors as therapeutic agents: historical perspective and future direction. *Recent Patents Anticancer Drug Discov* **1**, 223-36(2006).
6. Sarasin, A. An overview of the mechanisms of mutagenesis and carcinogenesis. *Mutation Research/Reviews in Mutation Research* **544**, 99-106(2003).
7. Hlatky, L., Hahnfeldt, P. & Folkman, J. Clinical Application of Antiangiogenic Therapy: Microvessel Density, What It Does and Doesn't Tell Us. *J. Natl. Cancer Inst.* **94**, 883-893(2002).
8. Carmeliet, P. & Jain, R.K. Angiogenesis in cancer and other diseases. **407**, 249-257(2000).
9. Ziche, M., Donnini, S. & Morbidelli, L. Development of new drugs in angiogenesis. *Curr.Drug Targets* **5**, 485-493(2004).
10. Leenders, W.P.J., Küsters, B. & de Waal, R.M.W. Vessel co-option: how tumors obtain blood supply in the absence of sprouting angiogenesis. *Endothelium* **9**, 83-7(2002).
11. Patan, S. et al. Vascular morphogenesis and remodeling in a human tumor xenograft: blood vessel formation and growth after ovariectomy and tumor implantation. *Circ Res* **89**, 732-9(2001).
12. Asahara, T. et al. Bone Marrow Origin of Endothelial Progenitor Cells Responsible

for Postnatal Vasculogenesis in Physiological and Pathological Neovascularization. *Circ Res* **85**, 221-228(1999).
13. Duda, D.G. et al. Evidence for incorporation of bone marrow-derived endothelial cells into perfused blood vessels in tumors. *Blood* **107**, 2774-2776(2006).
14. Asahara, T. et al. VEGF contributes to postnatal neovascularization by mobilizing bone marrow-derived endothelial progenitor cells. *The EMBO Journal* **18**, (1999).
15. Mazure, N.M., Brahimi-Horn, M.C. & Pouysségur, J. Protein kinases and the hypoxia-inducible factor-1, two switches in angiogenesis. *Curr Pharm Des* **9**, 531-41(2003).
16. Giuriato, S. et al. Sustained regression of tumors upon MYC inactivation requires p53 or thrombospondin-1 to reverse the angiogenic switch. *Proceedings of the National Academy of Sciences of the United States of America* **103**, (2006).
17. Sowter, H.M. et al. Expression and localization of the vascular endothelial growth factor family in ovarian epithelial tumors. *Lab Invest* **77**, 607-14(1997).
18. Yabkowitz, R. et al. Inflammatory Cytokines and Vascular Endothelial Growth Factor Stimulate the Release of Soluble Tie Receptor From Human Endothelial Cells Via Metalloprotease Activation. *Blood* **93**, 1969-1979(1999).
19. Fukumura, D. et al. Tumor Induction of VEGF Promoter Activity in Stromal Cells. *Cell* **94**, 715-725(1998).
20. Ferrara, N., Gerber, H. & LeCouter, J. The biology of VEGF and its receptors. *Nat Med* **9**, 669-676(2003).
21. Gospodarowicz, D., Abraham, J.A. & Schilling, J. Isolation and characterization of a vascular endothelial cell mitogen produced by pituitary-derived folliculo stellate cells. *Proc Natl Acad Sci U S A* **86**, 7311-5(1989).
22. Dvorak, H.F. et al. Vascular permeability factor/vascular endothelial growth factor, microvascular hyperpermeability, and angiogenesis. *The American Journal of Pathology* **146**, (1995).
23. Bikfalvi, A. Angiogenesis: health and disease. *Ann Oncol* **17 Suppl 10**, x65-70(2006).
24. Shweiki, D. et al. Vascular endothelial growth factor induced by hypoxia may mediate hypoxia-initiated angiogenesis. *Nature* **359**, 843-845(1992).
25. Augustin, H.G. Tubes, Branches, and Pillars: The Many Ways of Forming a New Vasculature. *Circ Res* **89**, 645-647(2001).
26. Armelin, H.A. Pituitary Extracts and Steroid Hormones in the Control of 3T3 Cell Growth. *Proceedings of the National Academy of Sciences of the United States of America* **70**, (1973).
27. Presta, M. et al. Fibroblast growth factor/fibroblast growth factor receptor system in angiogenesis. *Cytokine Growth Factor Rev* **16**, 159-78(2005).
28. McCarty, M.F. et al. Quantitative and qualitative in vivo angiogenesis assay. *Int J Oncol* **21**, 5-10(2002).
29. Baird, A., Mormède, P. & Böhlen, P. Immunoreactive fibroblast growth factor (FGF) in a transplantable chondrosarcoma: inhibition of tumor growth by antibodies to FGF. *J Cell Biochem* **30**, 79-85(1986).
30. Presta, M. et al. Basic fibroblast growth factor is released from endothelial extracellular matrix in a biologically active form. *J Cell Physiol* **140**, 68-74(1989).

31. Friedlander, M. et al. Definition of two angiogenic pathways by distinct alpha v integrins. *Science* **270**, 1500-2(1995).
32. Pepper, M.S. et al. Potent synergism between vascular endothelial growth factor and basic fibroblast growth factor in the induction of angiogenesis in vitro. *Biochem Biophys Res Commun* **189**, 824-31(1992).
33. Yoshiji, H. et al. Synergistic effect of basic fibroblast growth factor and vascular endothelial growth factor in murine hepatocellular carcinoma. *Hepatology* **35**, 834-42(2002).
34. Jain, R.K. Normalization of Tumor Vasculature: An Emerging Concept in Antiangiogenic Therapy. *Science* **307**, 58-62(2005).
35. Baluk, P. et al. Abnormalities of basement membrane on blood vessels and endothelial sprouts in tumors. *Am J Pathol* **163**, 1801-15(2003).
36. Hashizume, H. et al. Openings between Defective Endothelial Cells Explain Tumor Vessel Leakiness. *Am J Pathol* **156**, 1363-1380(2000).
37. Gerlowski, L.E. & Jain, R.K. Microvascular permeability of normal and neoplastic tissues. *Microvasc Res* **31**, 288-305(1986).
38. Kimura, H. et al. Fluctuations in red cell flux in tumor microvessels can lead to transient hypoxia and reoxygenation in tumor parenchyma. *Cancer Res* **56**, 5522-8(1996).
39. Jain, R.K. Transport of molecules in the tumor interstitium: a review. *Cancer Res* **47**, 3039-51(1987).
40. Wiig, H. et al. Interstitial fluid pressure in DMBA-induced rat mammary tumours. *Scand J Clin Lab Invest* **42**, 159-64(1982).
41. Tozer, G.M. et al. The relationship between regional variations in blood flow and histology in a transplanted rat fibrosarcoma. *Br J Cancer* **61**, 250-7(1990).
42. Falk, P. Differences in vascular pattern between the spontaneous and the transplanted C3H mouse mammary carcinoma. *Eur J Cancer Clin Oncol* **18**, 155-65(1982).
43. Hanahan, D. & Folkman, J. Patterns and Emerging Mechanisms of the Angiogenic Switch during Tumorigenesis. *Cell* **86**, 353-364(1996).
44. Ljungkvist, A.S.E. et al. Dynamics of tumor hypoxia measured with bioreductive hypoxic cell markers. *Radiat Res* **167**, 127-45(2007).
45. Zeh, H.J. & Lotze, M.T. Addicted to death: invasive cancer and the immune response to unscheduled cell death. *J Immunother* **28**, 1-9
46. Folkman, J. Seminars in Medicine of the Beth Israel Hospital, Boston. Clinical applications of research on angiogenesis. *N Engl J Med* **333**, 1757-63(1995).
47. Carmeliet, P. Angiogenesis in life, disease and medicine. *Nature* **438**, 932-936(2005).
48. Lentzsch, S. et al. Immunomodulatory analogs of thalidomide inhibit growth of Hs Sultan cells and angiogenesis in vivo. *Leukemia* **17**, 41-44(2003).
49. Stephens, T.D. & Fillmore, B.J. Hypothesis: thalidomide embryopathy-proposed mechanism of action. *Teratology* **61**, 189-95(2000).
50. Franks, M.E., Macpherson, G.R. & Figg, W.D. Thalidomide. *The Lancet* **363**, 1802-1811(2004).
51. Baguley, B.C. Antivascular therapy of cancer: DMXAA. *The Lancet Oncology* **4**, 141-148(2003).
52. Dahl, O., Borkamo, E.D. & Fluge, O. Current status of antivascular therapy and

targeted treatment in the clinic. *Int J Hyperthermia* **24**, 97-110(2008).
53. Pattillo, C.B. et al. Targeting of the antivascular drug combretastatin to irradiated tumors results in tumor growth delay. *Pharm Res* **22**, 1117-20(2005).
54. Kerbel, R. & Folkman, J. Clinical translation of angiogenesis inhibitors. *Nat Rev Cancer* **2**, 727-39(2002).
55. Segers, J. et al. Potentiation of cyclophosphamide chemotherapy using the anti-angiogenic drug thalidomide: Importance of optimal scheduling to exploit the [`]normalization' window of the tumor vasculature. *Cancer Letters* **244**, 129-135(2006).
56. Ma, J. et al. Pharmacodynamic-mediated Reduction of Temozolomide Tumor Concentrations by the Angiogenesis Inhibitor TNP-470. *Cancer Res* **61**, 5491-5498(2001).
57. Strijkers, G.J. et al. MRI contrast agents: current status and future perspectives. *Anticancer Agents Med Chem* **7**, 291-305(2007).
58. Lutz, A.M. et al. Detection of Synovial Macrophages in an Experimental Rabbit Model of Antigen-induced Arthritis: Ultrasmall Superparamagnetic Iron Oxide-enhanced MR Imaging. *Radiology* **233**, 149-157(2004).
59. Bhujwalla, Z.M., Artemov, D. & Glockner, J. Tumor angiogenesis, vascularization, and contrast-enhanced magnetic resonance imaging. *Top Magn Reson Imaging* **10**, 92-103(1999).
60. Padhani, A.R. MRI for assessing antivascular cancer treatments. *Br J Radiol* **76**, S60-80(2003).
61. Veldhuis, W.B. et al. Interferon-Beta Prevents Cytokine-Induced Neutrophil Infiltration and Attenuates Blood-Brain Barrier Disruption. *J Cereb Blood Flow Metab* **23**, 1060-1069(2003).
62. Weissleder, R. & Mahmood, U. Molecular Imaging. *Radiology* **219**, 316-333(2001).
63. Heyn, C. et al. In vivo MRI of cancer cell fate at the single-cell level in a mouse model of breast cancer metastasis to the brain. *Magnetic Resonance in Medicine* **56**, 1001-1010(2006).
64. Caravan, P. et al. Gadolinium(III) Chelates as MRI Contrast Agents: Structure, Dynamics, and Applications. *Chem Rev* **99**, 2293-352(1999).
65. Aime, S. et al. Insights into the use of paramagnetic Gd(III) complexes in MR-molecular imaging investigations. *J Magn Reson Imaging* **16**, 394-406(2002).
66. Raymond, K.N. & Pierre, V.C. Next generation, high relaxivity gadolinium MRI agents. *Bioconjug Chem* **16**, 3-8
67. Nunn, A.D., Linder, K.E. & Tweedle, M.F. Can receptors be imaged with MRI agents? *Q J Nucl Med* **41**, 155-62(1997).
68. Laus, S. et al. GdIII complexes with fast water exchange and high thermodynamic stability: potential building blocks for high-relaxivity MRI contrast agents. *Chemistry* **9**, 3555-66(2003).
69. de Lussanet, Q.G. et al. Dynamic Contrast-enhanced MR Imaging Kinetic Parameters and Molecular Weight of Dendritic Contrast Agents in Tumor Angiogenesis in Mice. *Radiology* **235**, 65-72(2005).
70. Wang, S.J., Brechbiel, M. & Wiener, E.C. Characteristics of a new MRI contrast agent prepared from polypropyleneimine dendrimers, generation 2. *Invest Radiol* **38**,

662-8(2003).
71. Geninatti Crich, S. et al. Magnetic Resonance Visualization of Tumor Angiogenesis by Targeting Neural Cell Adhesion Molecules with the Highly Sensitive Gadolinium-Loaded Apoferritin Probe. *Cancer Res* **66**, 9196-9201(2006).
72. Hazell, A.S. Astrocytes and manganese neurotoxicity. *Neurochem Int* **41**, 271-7(2002).
73. Madsen, K. et al. The effect of paramagnetic manganese cations on 1H MR spectroscopy of the brain. *NMR in Biomedicine* Accepted for publication
74. Federle, M. et al. Efficacy and safety of mangafodipir trisodium (MnDPDP) injection for hepatic MRI in adults: results of the U.S. Multicenter phase III clinical trials. Efficacy of early imaging. *J Magn Reson Imaging* **12**, 689-701(2000).
75. Shapiro, E.M., Skrtic, S. & Koretsky, A.P. Sizing it up: Cellular MRI using micron-sized iron oxide particles. *Magnetic Resonance in Medicine* **53**, 329-338(2005).
76. Bowen, C.V. et al. Application of the static dephasing regime theory to superparamagnetic iron-oxide loaded cells. *Magn Reson Med* **48**, 52-61(2002).
77. Bjørnerud, A. & Johansson, L. The utility of superparamagnetic contrast agents in MRI: theoretical consideration and applications in the cardiovascular system. *NMR Biomed* **17**, 465-77(2004).
78. Pathak, A.P., Rand, S.D. & Schmainda, K.M. The effect of brain tumor angiogenesis on the in vivo relationship between the gradient-echo relaxation rate change (DeltaR2*) and contrast agent (MION) dose. *J Magn Reson Imaging* **18**, 397-403(2003).
79. Marquardt, D.W. *An algorithm for least-squares estimation of nonlinear parameters*. **11**, 431-441(1963).
80. Scheuhammer, A.M. & Cherian, M.G. Binding of manganese in human and rat plasma. *Biochim Biophys Acta* **840**, 163-9(1985).
81. Mazur, G. et al. Angiogenesis measured by expression of CD34 antigen in lymph nodes of patients with non-Hodgkin's lymphoma. *Folia Histochem Cytobiol* **42**, 241-3(2004).
82. Detre, J.A. et al. Perfusion imaging. *Magn Reson Med* **23**, 37-45(1992).
83. Williams, D.S. et al. Magnetic resonance imaging of perfusion using spin inversion of arterial water. *Proc Natl Acad Sci U S A* **89**, 212-6(1992).
84. Golay, X., Hendrikse, J. & Lim, T.C.C. Perfusion Imaging Using Arterial Spin Labeling. *Topics in Magnetic Resonance Imaging February 2004* **15**, 10-27(2004).
85. Ogawa, S. et al. Oxygenation-sensitive contrast in magnetic resonance image of rodent brain at high magnetic fields. *Magn Reson Med* **14**, 68-78(1990).
86. Ogawa, S. et al. Brain magnetic resonance imaging with contrast dependent on blood oxygenation. *Proc Natl Acad Sci U S A* **87**, 9868-72(1990).
87. Ogawa, S. & Lee, T.M. Magnetic resonance imaging of blood vessels at high fields: in vivo and in vitro measurements and image simulation. *Magn Reson Med* **16**, 9-18(1990).
88. Logothetis, N.K. The neural basis of the blood-oxygen-level-dependent functional magnetic resonance imaging signal. *Philos Trans R Soc Lond B Biol Sci* **357**, 1003-37(2002).
89. Ostergaard, L. Cerebral perfusion imaging by bolus tracking. **15**, 3-9(2004).

90. Weisskoff, R.M. et al. Microscopic susceptibility variation and transverse relaxation: theory and experiment. *Magn Reson Med* **31**, 601-10(1994).
91. Larsson, H.B.W. et al. Myocardial perfusion modeling using MRI. *Magnetic Resonance in Medicine* **35**, 716-726(1996).
92. Uematsu, H. et al. Measurement of the vascularity and vascular leakage of gliomas by double-echo dynamic magnetic resonance imaging: a preliminary study. *Invest Radiol* **37**, 571-6(2002).
93. Boxerman, J.L., Schmainda, K.M. & Weisskoff, R.M. Relative cerebral blood volume maps corrected for contrast agent extravasation significantly correlate with glioma tumor grade, whereas uncorrected maps do not. *AJNR Am J Neuroradiol* **27**, 859-67(2006).
94. van Osch, M.J.P. et al. Measuring the arterial input function with gradient echo sequences. *Magn Reson Med* **49**, 1067-76(2003).
95. Simonsen, C.Z. et al. CBF and CBV measurements by USPIO bolus tracking: reproducibility and comparison with Gd-based values. *J Magn Reson Imaging* **9**, 342-7(1999).
96. Kiselev, V.G. Transverse relaxation effect of MRI contrast agents: a crucial issue for quantitative measurements of cerebral perfusion. *J Magn Reson Imaging* **22**, 693-6(2005).
97. Padhani, A.R. & Husband, J.E. Dynamic Contrast-enhanced MRI Studies in Oncology with an Emphasis on Quantification, Validation and Human Studies. *Clinical Radiology* **56**, 607-620(2001).
98. Calamante, F. Bolus dispersion issues related to the quantification of perfusion MRI data. *J Magn Reson Imaging* **22**, 718-22(2005).
99. Calamante, F., Mørup, M. & Hansen, L.K. Defining a local arterial input function for perfusion MRI using independent component analysis. *Magn Reson Med* **52**, 789-97(2004).
100. Calamante, F., Gadian, D.G. & Connelly, A. Delay and dispersion effects in dynamic susceptibility contrast MRI: simulations using singular value decomposition. *Magn Reson Med* **44**, 466-73(2000).
101. Ona Wu, L.Ø. Tracer arrival timing-insensitive technique for estimating flow in MR perfusion-weighted imaging using singular value decomposition with a block-circulant deconvolution matrix. *Magnetic Resonance in Medicine* **50**, 164-174(2003).
102. van Osch, M.J.P., van der Grond, J. & Bakker, C.J.G. Partial volume effects on arterial input functions: shape and amplitude distortions and their correction. *J Magn Reson Imaging* **22**, 704-9(2005).
103. Heilmann, M. et al. Simultaneous dynamic T 1 and measurement for AIF assessment combined with DCE MRI in a mouse tumor model. *Magnetic Resonance Materials in Physics, Biology and Medicine* **20**, 193-203(2007).
104. Kim, E. et al. Simultaneous acquisition of perfusion and permeability from corrected relaxation rates with dynamic susceptibility contrast dual gradient echo. *Magn Reson Imaging* **22**, 307-14(2004).
105. Vonken, E.P. et al. Simultaneous quantitative cerebral perfusion and Gd-DTPA extravasation measurement with dual-echo dynamic susceptibility contrast MRI. *Magn Reson Med* **43**, 820-7(2000).

106. de Bazelaire, C. et al. Combined T2* and T1 measurements for improved perfusion and permeability studies in high field using dynamic contrast enhancement. *Eur Radiol* **16**, 2083-91(2006).
107. Zhuo, J., Poston, R. & Gullapi, R. Minimizing echo time dependence in the assessment of perfusion parameters from multiecho T1–T2* sequences. 1121
108. Thompson, H.K. et al. Indicator transit time considered as a gamma variate. *Circ Res* **14**, 502-15(1964).
109. Alsop, D. & Schlaug, G. The Equivalence of SVD and Fourier Deconvolution for dynamic suscebtibility contrast analysis. *Proc Intl Soc Mag Reson Med.* **9**, 1581(2001).
110. Smith, A.M. et al. Whole brain quantitative CBF and CBV measurements using MRI bolus tracking: comparison of methodologies. *Magn Reson Med* **43**, 559-64(2000).
111. Wu, O. et al. Tracer arrival timing-insensitive technique for estimating flow in MR perfusion-weighted imaging using singular value decomposition with a block-circulant deconvolution matrix. *Magn Reson Med* **50**, 164-74(2003).
112. Hansen, P. Analysis of discrete ill-posed problems by means of the L-curve. *SIAM Rev* **34**, 561-580(1992).
113. Gobbel, G.T. & Fike, J.R. A deconvolution method for evaluating indicator-dilution curves. *Phys Med Biol* **39**, 1833-54(1994).
114. Tikhonov, A. Solution of incorrectly formulated probles and the regularization method. *Soviet Math Dokl* **4**, 1035-1038(1963).
115. Belge , M., Kilmer, M. & Miller, E. Efficient determination of multiple regularization parameters in a generalized L-curve framework. *Inverse Problems* **18**, 1161-1183(2002).
116. Calamante, F., Gadian, D.G. & Connelly, A. Quantification of bolus-tracking MRI: Improved characterization of the tissue residue function using Tikhonov regularization. *Magn Reson Med* **50**, 1237-47(2003).
117. Vonken, E.P. et al. Maximum likelihood estimation of cerebral blood flow in dynamic susceptibility contrast MRI. *Magn Reson Med* **41**, 343-50(1999).
118. Andersen, I.K. et al. Perfusion quantification using Gaussian process deconvolution. *Magn Reson Med* **48**, 351-61(2002).
119. Larson, K.B. et al. Tracer-kinetic analysis for measuring regional cerebral blood flow by dynamic nuclear magnetic resonance imaging. *J Theor Biol* **170**, 1-14(1994).
120. Stewart, G. Researches on the circulation time in organs and on the influences which affect it. Parts I-III. *J Physiol* **15**, 1-89(1894).
121. Patlak, C.S., Blasberg, R.G. & Fenstermacher, J.D. Graphical evaluation of blood-to-brain transfer constants from multiple-time uptake data. *J Cereb Blood Flow Metab* **3**, 1-7(1983).
122. Patlak, C.S. & Blasberg, R.G. Graphical evaluation of blood-to-brain transfer constants from multiple-time uptake data. Generalizations. *J Cereb Blood Flow Metab* **5**, 584-90(1985).
123. Tofts, P.S. et al. Estimating kinetic parameters from dynamic contrast-enhanced T(1)-weighted MRI of a diffusable tracer: standardized quantities and symbols. *J Magn Reson Imaging* **10**, 223-32(1999).
124. Ewing, J.R. et al. Model selection in magnetic resonance imaging measurements of

vascular permeability: Gadomer in a 9L model of rat cerebral tumor. *J Cereb Blood Flow Metab* **26**, 310-320(2005).
125. Brandt, C.T. et al. Impact of bacteremia on the pathogenesis of experimental pneumococcal meningitis. *J Infect Dis* **197**, 235-44(2008).
126. Barrett, T. et al. MRI of tumor angiogenesis. *J Magn Reson Imaging* **26**, 235-49(2007).
127. Goon, P.K.Y. et al. Circulating Endothelial Cells, Endothelial Progenitor Cells, and Endothelial Microparticles in Cancer. *Neoplasia (New York, N.Y.)* **8**, (2006).
128. Rohren, E.M., Turkington, T.G. & Coleman, R.E. Clinical Applications of PET in Oncology. *Radiology* **231**, 305-332(2004).
129. Ellegala, D.B. et al. Imaging Tumor Angiogenesis With Contrast Ultrasound and Microbubbles Targeted to {alpha}v{beta}3. *Circulation* **108**, 336-341(2003).
130. Silva, A.C., Kim, S.G. & Garwood, M. Imaging blood flow in brain tumors using arterial spin labeling. *Magn Reson Med* **44**, 169-73(2000).
131. Kimura, H. et al. Perfusion imaging of meningioma by using continuous arterial spin-labeling: comparison with dynamic susceptibility-weighted contrast-enhanced MR images and histopathologic features. *AJNR Am J Neuroradiol* **27**, 85-93(2006).
132. Moffat, B.A. et al. Inhibition of Vascular Endothelial Growth Factor (VEGF)-A Causes a Paradoxical Increase in Tumor Blood Flow and Up-Regulation of VEGF-D. *Clin Cancer Res* **12**, 1525-1532(2006).
133. Tempel, C. & Neeman, M. Spatial and temporal modulation of perfusion in the rat ovary measured by arterial spin labeling MRI. *J Magn Reson Imaging* **9**, 794-803(1999).
134. Boss, A. et al. Morphological, contrast-enhanced and spin labeling perfusion imaging for monitoring of relapse after RF ablation of renal cell carcinomas. *Eur Radiol* **16**, 1226-36(2006).
135. Ogawa, S. et al. Functional brain mapping by blood oxygenation level-dependent contrast magnetic resonance imaging. A comparison of signal characteristics with a biophysical model. *Biophysical Journal* **64**, (1993).
136. Rijpkema, M. et al. BOLD MRI response to hypercapnic hyperoxia in patients with meningiomas: correlation with Gadolinium-DTPA uptake rate. *Magn Reson Imaging* **22**, 761-7(2004).
137. Gilead, A., Meir, G. & Neeman, M. The role of angiogenesis, vascular maturation, regression and stroma infiltration in dormancy and growth of implanted MLS ovarian carcinoma spheroids. *Int J Cancer* **108**, 524-31(2004).
138. Gilad, A.A. et al. Functional and molecular mapping of uncoupling between vascular permeability and loss of vascular maturation in ovarian carcinoma xenografts: the role of stroma cells in tumor angiogenesis. *Int J Cancer* **117**, 202-11(2005).
139. Jiang, L. et al. Comparison of BOLD contrast and Gd-DTPA dynamic contrast-enhanced imaging in rat prostate tumor. *Magn Reson Med* **51**, 953-60(2004).
140. Marzola, P. et al. In Vivo Assessment of Antiangiogenic Activity of SU6668 in an Experimental Colon Carcinoma Model. *Clin Cancer Res* **10**, 739-750(2004).
141. Wedam, S.B. et al. Antiangiogenic and Antitumor Effects of Bevacizumab in Patients With Inflammatory and Locally Advanced Breast Cancer. *J Clin Oncol* **24**, 769-777(2006).

142. Mross, K. et al. Phase I clinical and pharmacokinetic study of PTK/ZK, a multiple VEGF receptor inhibitor, in patients with liver metastases from solid tumours. *Eur J Cancer* **41**, 1291-9(2005).
143. Thomas, A.L. et al. Phase I study of the safety, tolerability, pharmacokinetics, and pharmacodynamics of PTK787/ZK 222584 administered twice daily in patients with advanced cancer. *J Clin Oncol* **23**, 4162-71(2005).
144. Cha, S. et al. Dynamic Contrast-enhanced T2*-weighted MR Imaging of Recurrent Malignant Gliomas Treated with Thalidomide and Carboplatin. *AJNR Am J Neuroradiol* **21**, 881-890(2000).
145. Cha, S. et al. Dynamic, contrast-enhanced perfusion MRI in mouse gliomas: correlation with histopathology. *Magn Reson Med* **49**, 848-55(2003).
146. Kiessling, F. et al. Comparing dynamic parameters of tumor vascularization in nude mice revealed by magnetic resonance imaging and contrast-enhanced intermittent power Doppler sonography. *Invest Radiol* **38**, 516-24(2003).
147. Schlemmer, H. et al. Can pre-operative contrast-enhanced dynamic MR imaging for prostate cancer predict microvessel density in prostatectomy specimens? *Eur Radiol* **14**, 309-17(2004).
148. Buckley, D.L. et al. Microvessel density of invasive breast cancer assessed by dynamic Gd-DTPA enhanced MRI. *J Magn Reson Imaging* **7**, 461-4
149. Su, M. et al. Correlation of dynamic contrast enhancement MRI parameters with microvessel density and VEGF for assessment of angiogenesis in breast cancer. *J Magn Reson Imaging* **18**, 467-77(2003).
150. Hulka, C.A. et al. Dynamic echo-planar imaging of the breast: experience in diagnosing breast carcinoma and correlation with tumor angiogenesis. *Radiology* **205**, 837-42(1997).
151. Knopp, M.V. et al. Pathophysiologic basis of contrast enhancement in breast tumors. *J Magn Reson Imaging* **10**, 260-6(1999).
152. Ah-See, M., Padhani, A.R. & Taylor, N. Evaluation of VEGF expression within breast cancer biopsies & tumour microvasculature assessment by multi-functional dynamic contrast-enhanced MRI. *The 4th European Breast Cancer Conference (EBCC-4)* (2004).
153. Galbraith, S.M. et al. Combretastatin A4 Phosphate Has Tumor Antivascular Activity in Rat and Man as Demonstrated by Dynamic Magnetic Resonance Imaging. *J Clin Oncol* **21**, 2831-2842(2003).
154. Pham, C.D. et al. Magnetic resonance imaging detects suppression of tumor vascular permeability after administration of antibody to vascular endothelial growth factor. *Cancer Invest* **16**, 225-30(1998).
155. Gossmann, A. et al. Dynamic contrast-enhanced magnetic resonance imaging as a surrogate marker of tumor response to anti-angiogenic therapy in a xenograft model of glioblastoma multiforme. **15**, 233-240(2002).
156. Schmiedl, U. et al. Albumin labeled with Gd-DTPA. An intravascular contrast-enhancing agent for magnetic resonance blood pool and perfusion imaging. *Acta Radiol Suppl* **374**, 99-102(1990).
157. Lauffer, R.B. et al. MS-325: albumin-targeted contrast agent for MR angiography. *Radiology* **207**, 529-38(1998).

158. Turetschek, K. et al. MRI assessment of microvascular characteristics in experimental breast tumors using a new blood pool contrast agent (MS-325) with correlations to histopathology. *J Magn Reson Imaging* **14**, 237-42(2001).
159. Marzola, P. et al. Early Antiangiogenic Activity of SU11248 Evaluated In vivo by Dynamic Contrast-Enhanced Magnetic Resonance Imaging in an Experimental Model of Colon Carcinoma. *Clin Cancer Res* **11**, 5827-5832(2005).
160. Kobayashi, H. et al. Application of a Macromolecular Contrast Agent for Detection of Alterations of Tumor Vessel Permeability Induced by Radiation. *Clin Cancer Res* **10**, 7712-7720(2004).
161. Turetschek, K. et al. MR imaging characterization of microvessels in experimental breast tumors by using a particulate contrast agent with histopathologic correlation. *Radiology* **218**, 562-9(2001).
162. van Dijke, C.F. et al. Mammary carcinoma model: correlation of macromolecular contrast-enhanced MR imaging characterizations of tumor microvasculature and histologic capillary density. *Radiology* **198**, 813-8(1996).
163. de Lussanet, Q.G. et al. Gadopentetate Dimeglumine versus Ultrasmall Superparamagnetic Iron Oxide for Dynamic Contrast-enhanced MR Imaging of Tumor Angiogenesis in Human Colon Carcinoma in Mice. *Radiology* **229**, 429-438(2003).
164. Pathak, A.P. et al. MR-derived cerebral blood volume maps: issues regarding histological validation and assessment of tumor angiogenesis. *Magn Reson Med* **46**, 735-47(2001).
165. Arbab, A.S. et al. Comparison of transfection agents in forming complexes with ferumoxides, cell labeling efficiency, and cellular viability. *Mol Imaging* **3**, 24-32(2004).
166. Anderson, S.A. et al. Noninvasive MR imaging of magnetically labeled stem cells to directly identify neovasculature in a glioma model. *Blood* **105**, 420-425(2005).
167. Miller, J.C. et al. Imaging Angiogenesis: Applications and Potential for Drug Development. *J. Natl. Cancer Inst.* **97**, 172-187(2005).
168. Winter, P.M. et al. Molecular Imaging of Angiogenesis in Nascent Vx-2 Rabbit Tumors Using a Novel {alpha}{nu}{beta}3-targeted Nanoparticle and 1.5 Tesla Magnetic Resonance Imaging. *Cancer Res* **63**, 5838-5843(2003).
169. Mulder, W.J.M. et al. MR molecular imaging and fluorescence microscopy for identification of activated tumor endothelium using a bimodal lipidic nanoparticle. *FASEB J* **19**, 2008-10(2005).
170. Langereis, S. et al. Evaluation of Gd(III)DTPA-terminated poly(propylene imine) dendrimers as contrast agents for MR imaging. *NMR Biomed* **19**, 133-41(2006).
171. Wells, J.M. et al. Electroporation-enhanced gene delivery in mammary tumors. *Gene Ther* **7**, 541-7(2000).

# Manuscript I *In vivo* angiogenesis assayed using MRI

An MR compatible *in vivo* assay, designed to evaluate the effects of vascular-targeted drugs, has been developed and compared with a validated optical-based method. Plexiglas cylinders containing Matrigel and pro-angiogenic agents were implanted sub-cutaneously in nude mice and treated with the anti-angiogenic agent thalidomide. Using quantitative $T_2$ measurements obtained before and after administration of iron oxide contrast agent, significant anti-angiogenic effects of the drug where shown clearly demonstrating the feasibility of the approach. A dynamic contrast enhanced MRI method based on $T_2$* effects did not show significant differences when compared to control animals. This study clearly shows the feasibility and potential of the developed Matrigel-based system to provide a simple, reproducible *in vivo* assay that may be used to assess a wide range of angiotherapeutic agents using minimally invasive MR methods.

## *I.1 Introduction*

Angiogenesis, defined as the process of developing new blood vessels from pre-existing vasculature, is a critical process in cancer development. Beyond a volume of 1 $mm^3$, tumours require new blood vessel formation[1,2], for continued tumour development. Whilst angiogenesis is essential for tumour growth, it also appears to increase the probability of tumour cells entering the circulation leading to metastatic spread of the disease. The

angiogenic process is therefore an obvious target for anti-cancer strategies and this has led to the development of a relatively new class of vascular targeted agents: angiotherapeutics. The development of new blood vessels is promoted by an array of matrix molecules, accessory cells and soluble mediators that may be released by host cells or by tumour cells themselves. Hence, there are a multitude of possible targets and, therefore, strategies for developing vascular-targeted anti cancer agents. As a result, there are many endogenous and synthetic angiotherapeutic agents under development and in clinical trials.

In the early stages of drug development, potential angiotherapeutic agents may be identified using *in vitro* screening methods. However, when compared to the development of other classes of drugs, *in vivo* assessment is a particularly important step in the pre-clinical evaluation of potential agents. A critical review[3] has emphasized the essential role of *in vivo* systems to test the efficacy of both pro- and anti-angiogenic agents. The highly complex nature of cytokine interactions and vascular responses make *in vivo* assays an essential step in the evaluation of new agents.

Although implanted animal tumours provide a means of assessing the action of angiotherapeutics, a simple reproducible *in vivo* model of non-tumour vessel development would provide a system of significant value. Matrigel plug implant systems have been developed previously to address the limitations of *in vitro* assays and are becoming an essential component of *in vivo* assays[4,5,6]. Matrigel systems have been previously used as 'metabolic Boyden chambers' where MRI and MRS methods have been used successfully to study cell invasion *in vitro*[7,8]. Consequently, this study has utilized the simplicity of the Matrigel system together with the magnetic properties of the gel, where long $T_2$ values would provide maximal sensitivity to both cellular infiltration and superparamagnetic contrast agent effects. MR techniques allow a longitudinal study with the same subject serving as its own control hence the combined use of Matrigel with MR could provide a potentially powerful approach for assessing a wide variety of agents.

To demonstrate the feasibility of the approach, the anti-angiogenic effects of thalidomide on the vascularisation of Matrigel, preloaded with pro-angiogenic cytokines, was investigated using contrast enhanced MR methods. The anti-angiogenic mechanism of action of thalidomide is not yet

fully understood. At pharmacological doses, thalidomide has modest or no effect on proliferation of endothelial and malignant cells *in vitro*[9,10,11,12,13]. Inhibition of angiogenesis induced by bFGF as well as VEGF in a cornea micropocket assay is independent of anti-inflammatory effects and suppression of TNF-$\alpha$ production by thalidomide[14]. It has been proposed that thalidomide may down regulate the formation $\alpha_v\beta_3$ and $\alpha_v\beta_5$ integrins (required for bFGF and VEGF-driven angiogenesis[15]) by DNA intercalation of GC-rich promoter regions in the genes of the individual integrin subunits[16], which would affect endothelial cell migration. Whilst down regulation of the $\beta_3$ subunit has been demonstrated[17], another study found that thalidomide did not modulate $\alpha_v\beta_3$ expression[18]. Decreased levels in patient plasma[19], embryos[11], and conditioned medium from endothelial cell culture[13] indicate that thalidomide may inhibit production of bFGF and/or VEGF, possibly also by DNA intercalation[20]. Despite the incomplete understanding of how thalidomide exerts its action, it remains a potent anti-angiogenic agent and was selected for this study.

Building upon previous preliminary data with the Matrigel system, a superparamagnetic iron oxide contrast agent was applied to assess the effects of the angiotherapeutic. The preliminary studies showed that the high vascular permeability associated with the cytokines designed to promote angiogenesis made the extracellular contrast agent GdDTPA less appropriate than a blood-bourne iron oxide particle[21]. Consequently, the kinetics of contrast agent induced changes in signal intensity using a $T_2$* weighted sequence were investigated. In addition, standard $T_2$ measurements, acquired before and after iron oxide administration, were used to minimize 'blooming' from $T_2$* effects potentially increasing the accuracy of the measurements. Data were then compared to a validated optical-based assay. This study shows that using dynamic iron oxide induced changes in signal intensity, the anti-angiogenic effects of thalidomide can be demonstrated, validating the methodology.

## *I.2 Materials and Methods*

### I.2.1 Matrigel chamber preparation

Matrigel chambers were assembled from 14 mm diameter Millipore diffusion chamber rings with side hole (Millipore Corp., Billerica, USA)

and two nylon meshed membranes punched from 180µm pore size Nylon Net Filter (Millipore Corp., Billerica, USA) as described previously . M Cement (Millipore Corp., Billerica, USA) was used to attach the membranes to the diffusion chamber. Assembled chambers, with an approximate volume of 0.2 $cm^3$, were sterilized by irradiation. Recombinant human bFGF (Sigma-Aldrich, Vallensbaek, Denmark) and recombinant murine VEGF (Sigma-Aldrich, Vallensbaek, Denmark) were reconstituted according to manufacturers recommendations. Growth Factor Reduced Matrigel (BD Biosciences, San Diego, CA) was thawed overnight on ice, and a stock solution of Matrigel containing 750 ng/ml of bFGF and 250 ng/ml of VEGF was prepared, aliquoted into appropriate portions and frozen. On the day prior to each chamber implantation, a portion of the Matrigel solution was thawed overnight on ice. The Matrigel mixture was drawn up into a syringe, and briefly warmed by hand to speed up the solidification process after injection. Carefully, the mixture was injected through the side hole into the chambers, using a 27-gauge needle and allowed to solidify. Care was taken to prevent the air flow of the laminar airflow hood from drying out the chambers.

### I.2.2 Animals, chamber implantation and thalidomide administration

Male nude NMRI mice (Taconic M&B, Lille Skensved, Denmark), 6 weeks of age, were kept in individually ventilated SealSafe cages (Scanbur BK A/S, Karlslunde, Denmark) with free access to sterile food and water. Lighting was controlled in a 12-hour light/dark cycle. Following an acclimatization period of 1 week, animals were anesthetized using a saline solution containing xylazine 1 mg/kg (Rompun®, Bayer, Kgs. Lyngby, Denmark) and ketamine 10 mg/kg (Ketalar®, Pfizer, Sollentuna, Sweden). An incision of approximately 1.5 cm length was made transversally in the neck region of each mouse, and a subcutaneous pocket on both flanks was formed by blunt dissection. A chamber was inserted into each pocket, and the incision closed with non-resorbable suture (Ethicon 6-0, Ethicon, Norderstedt, Germany). The location of the incision removed from the actual implantation site minimised any effects of mechanical stress by the rigid chambers on the wounds. Thalidomide (Sigma-Aldrich, Vallensbaek, Denmark) was added to a sterile 0.5% carboxy methyl cellulose solution to a concentration of 10 mg/ml. The mice were randomized into two groups.

One group (N=9) were treated with daily i.p. injections of thalidomide at a dose of 200 mg/kg, while animals in the control group (N=11) were not treated. Twelve days after implantation, the mice were imaged by MR.

### I.2.3 Magnetic Resonance Imaging

Magnetic resonance imaging was performed using a 4.7T Varian Inova system utilising a home built volume and surface coil. Animals were anaesthetized using a sub-cutaneously injected mixture of hypnorm/dormicum/atropine. Animals were then positioned within the magnet with a surface coil placed over the chamber implanted in the right flank. On three occasions, air bubbles trapped within the Matrigel matrix had significant detrimental effects on image quality and the coil was subsequently repositioned over the left flank. Following the acquisition of scout images, quantitative $T_2$ measurements were performed on a single 0.8mm slice, carefully positioned mid-way within the implant. Quantitative $T_2$ measurements were performed using a spin echo sequence with multiple readouts, (MA=128x128, 30x30 mm FOV, TR=3s, TE=15-180 in steps of 15 ms ($T_2$ pre). Mice were injected with 0.4 mg of Endorem (Guerbet, Denmark) via a cannulated tail vein and the bolus was followed using a $T_2$* weighted gradient echo flash sequence (MA=128x128, FOV=30x30 mm, TR=20ms, TE=5.2ms, FL=20degrees, 150 frames). Post-contrast $T_2$ measurements ($T_2$ post) were also performed. $T_2$ maps were calculated using non-linear least squares fitting applying the Levenberg-Marquardt method[22].

### I.2.4 MRI analysis

*in vivo*, Matrigel without infiltration has a $T_2$ of approx 60 ms, therefore pixels with a $T_2$ below 45 ms were considered to contain blood vessels and therefore infiltration. In order to estimate functional vessels the $T_2$ post images were subtracted from the $T_2$ pre images and pixels with a $T_2$ difference of 6ms or more were considered to contain functional blood vessels.

For the dynamic MRI images, the mean of the last 45 images were subtracted from the mean of the first 45 images and a signal difference threshold was selected based on visual inspection of the time series.

### I.2.5 Optical Quantification

Following MR examination, chambers were excised immediately after sacrificing the mouse, placed on a white surface and photographed from both sides using an Olympus SC-40 microscope (Olympus, Melville, NY) fitted with a ring lighting system and a Leica DC-150 digital camera (Leica, Bannockburn, IL). Using image processing software (Paint Shop Pro 8.1, Jasc Software, Eden Prairie, MN), a region of interest on each chamber was selected, corresponding to the area of the chamber within the inner border of the Plexiglas diffusion chamber ring, and the remaining part of the image darkened to black. By applying a specially defined filter to detect the number of red pixels, all the masked images were quantified using Sigma Scan Pro 5.0 (SPSS Science, Chicago, IL). The filter was constructed beforehand to select all colours of red hue and manually adjusted to correctly select red areas on a series of test optical images of Matrigel chambers to ensure specific adaptation to our imaging setup. The optical data was transferred to a spreadsheet and the percentage of red pixels within the inner border of the Plexiglas diffusion chamber was calculated.

### I.2.6 Statistics

The non-parametric Mann-Whitney *U*-test was used to test differences between groups, p-values below 0.05 were considered statistically significant. Simple correlation was used to compare the two methods (red pixel count and different MRI methods).

## *I.3 Results and Discussion*

Chambers were well tolerated with little adhesive tissue reaction observed when the chambers were removed. No macroscopic signs of inflammation were observed.

Representative examples of the different optical and MR parameters acquired (optical imaging, pre, post and difference $T_2$ as well as gradient echo dMRI) are shown in Figure I.1. Note that the red area of the optical image corresponds well with the dark area seen on $T_2$ pre and $T_2$ post images. As shown for animal (B), there is also good agreement between $T_2$ diff, and dMRI. Approximately 50% of the mice showed good agreement between $T_2$ diff and dMRI difference images in the untreated mice, while for

the thalidomide treated mice approximately 75% showed good agreement.

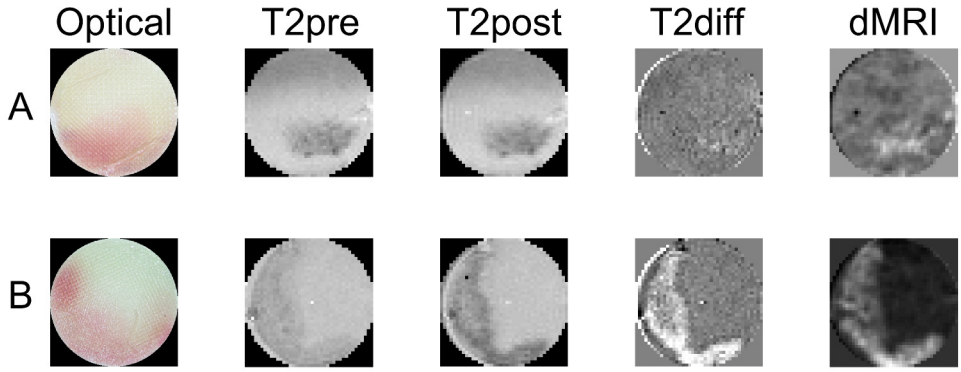


*Figure I.1: Example of different optical and MR images obtained for two different mice. Note that the red area in the optical image corresponds well with the dark area in $T_2$pre and $T_2$post. In B there is also good agreement with $T_2$diff and dMRI.*

Figure I.2 shows time curves from a chamber in which it is possible to identify three distinct regions based on the time curves. The red ROI has a very quick wash in of contrast and then shows slow clearance,

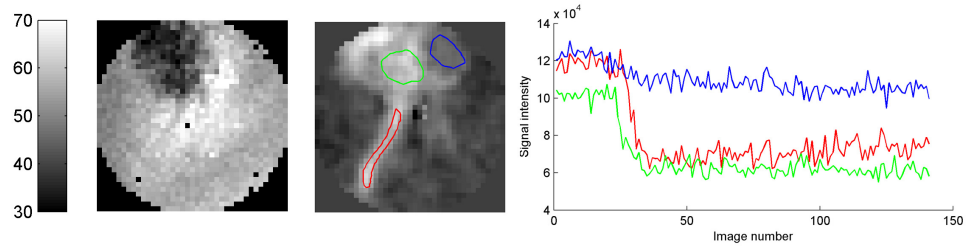


*Figure I.2: Quantitative $T_2$ map showing values post contrast (left) together with dMRI difference image (GE flash, TR/TE=20/5.2 ms, flip angle 20 degrees, 150 acqs). The image shown is the difference between the mean of the 25 first and last images. (middle). Tissue curves for the ROIs shown in the middle is shown on the right. A large infiltration is seen in the upper left corner. A large vessel is clearly visible on the dMRI difference map (middle). Some correspondence between post contrast $T_2$ map (left) and dMRI difference (middle) is seen. As shown in the time curves (right) three distinct regions could be identified. The red region appears to be a vessel where washout makes the signal return towards baseline after the initial dip caused by injection of contrast agent. The green and blue regions of interest show areas of differing vascularization.*

characteristics typical of a blood vessel. The green ROI shows slower wash in of contrast agent and no sign of clearance which would fit well with an area with tissue infiltration and leaky vessels. The blue ROI has the same characteristics as the green ROI but with less signal reduction which might be explained by low vascularization.

For all modalities the percentage of vessels/infiltration was quantified as described in materials and methods. The results of this quantification is shown in figure I.3. As shown in the figure both $T_2$ pre and $T_2$ post overestimate the percentage of vessels compared to the optical method while $T_2$ diff and dMRI are closer to the values of the optical method. All modalities showed statistically significant differences between untreated and treated animals except for the dMRI difference method.

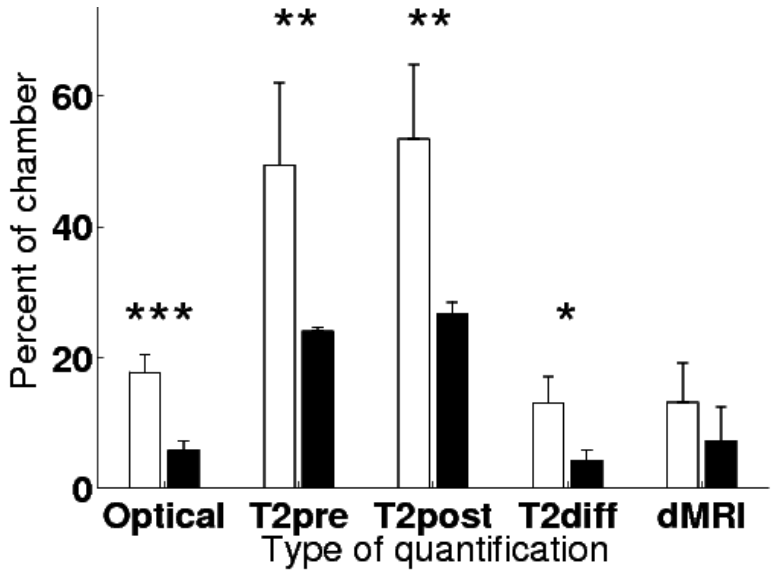


*Figure I.3: Percentage of chamber quantified as blood vessels using the types of quantification. Error bars indicate standard error of the mean.* Indicates significant differences with P<0.05, ** P<0.01, *** P<0.001*

Table 1 shows the correlation between the different MR modalities and the optical method for the scanned chamber as well as for the mean of both chambers. The results show that there is only good correlation (P<0.05) for

the $T_2$ difference method.

| | **Scanned chamber** | **Both chambers** |
|---|---|---|
| **$T_2$ pre** | 0.685 | 0.671 |
| **$T_2$ post** | 0.352 | 0.450 |
| **$T_2$ diff** | 0.005 ** | 0.012 * |
| **dMRI** | 0.129 | 0.098 |

***Table 1*** *P values for correlation between the chambers which were MR scanned and the optical images of the scanned chamber or both chambers. * Indicates significant differences with P<0.05, ** P<0.01*

Four MR derived parameters were measured. Three of the four showed significant difference between the control and treated group (Figure I.3).

When compared with the previously validated 'red pixel' methodology only $T_2$ diff values, indicative of functional blood vessels, were found to be correlated with the number of red pixels. Correlation of the red pixel measurements with $T_2$ diff values are consistent with the 'haemoglobin measurements' reflecting blood volume within the same ROI. The potential advantages of using MRI to measure blood delivery and not just haemoglobin, via the red pixel measurement, do not appear to have been realised previously. Furthermore, $T_2$ pre and $T_2$ post measurements appear to overestimate the percentage of vessels in each chamber probably due to the inclusion of avascular inflammatory tissue.

Thalidomide inhibits *in vitro* tube formation[11,23], and *in vivo* angiogenesis in matrigel assays[11,23]. In this study, thalidomide significantly decreased red coloration in the Matrigel chambers. Thalidomide inhibits *in vitro* endothelial cell migration[13,24] ; and is in accord with our previous observation that two substances with anti-angiogenic activity in the Matrigel chamber also inhibited EC migration *in vitro*[6,25], supporting the view that inhibiting endothelial cell migration is a central element of *in vivo* anti-angiogenic effects. Thalidomide (200mg/kg) was a more potent inhibitor of angiogenesis in the Matrigel Chamber assay than the established anti-angiogenic agent bevacizumab[25], an antibody that binds human VEGF. Although this could be related to bevacizumab being ineffective against the VEGF contribution from the murine tumor stroma,

the results presented here still demonstrate a powerful anti-angiogenic effect of thalidomide, detectable by optical and by MRI methods.

## I.4 Conclusion

Studying angiogenesis within the implanted chambers offers several advantages in terms of MRI; the ROI is very clearly defined, the implant is initially avascular with a long $T_2$ and it is not necessary to consider pre-existing vascularisation. Longitudinal studies are relatively simple to conduct as only simple rigid body realignment of acquired images will be required. Quantification by the optical / red-pixel method at the final timepoint is much faster than histological analysis of the tumor, making it easier to confirm the results by an alternative method. The dMRI difference maps show the initial effects of the contrast agent while the $T_2$ maps show the extent of tissue infiltration and steady state effects. The MR findings also appear consistent with the mechanism of action of thalidomide.
Here, a new approach to evaluate angiogenic responses in the Matrigel chamber assay using MRI has been presented. The use of a non-invasive evaluation method makes the Matrigel chamber assay a powerful tool to study angiogenic processes, which previous, invasive evaluation methods such as histology and measurement of red coloration do not permit. Optical measures of haemoglobin, as used previously in the *in vivo* Matrigel assay, may report on the extent of 'vascular infiltration' rather than viable/patent vasculature. Hence continuous observation of angiogenesis in Matrigel chambers over time, where individual animals may be followed longitudinally and act as their own controls, has the potential to contribute significantly to the understanding of the angiogenic process and its modulation by exogenous agents. The ability to use non-invasive MR methodology makes the Matrigel MR assay a potentially valuable tool in the routine assessment of a wide range of vascular targeted agents.

## Acknowledgements

Financial support from the Alfred Benzon Foundation and the University of Copenhagen is gratefully acknowledged. We would also like to thank Mogens Spang-Thomsen for his advisory assistance and Helle Simonsen, Lise Vejby Søgaard, Bente Møller, Jette Christiansen and Henrik Hasseldam for their technical support.

# Manuscript II Perfusion in brain tumors

The partly intact blood-brain barrier (BBB) and/or blood-brain tumor barrier (BTB) results in poor drug delivery into brain tumors making drug delivery to brain tumors a challenging problem, and the noninvasive detection of drug delivery critically important. In this study, *in vivo* magnetic resonance spectroscopy (MRS) was used to detect an anticancer agent, temozolomide (TMZ), *in vivo* in murine xenotransplants of the U87MG human brain cancer.

Dynamic MRI with the low molecular weight contrast agent, GdDTPA, was used to evaluate tumor vascular parameters. Carbon-13 labeled TMZ ([$^{13}$C]TMZ, 99%) was intraperitoneally administered at a dose of 15.5 μmol (3 mg/mouse) during the course of *in vivo* MRS experiment. Heteronuclear multiple-quantum coherence (HMQC) MRS of brain tumor was performed before and after i.p. administration of [$^{13}$C]TMZ.

Dynamic MRI experiments demonstrated slower recovery of MRI signal following intravenous bolus injection of GdDTPA, higher vascular flow and volume obtained by $T_2$*-weighted MRI as well as enhanced uptake of the contrast agent in the brain tumor in comparison to the normal brain obtained by $T_1$-weighted MRI. These data demonstrate partial breakdown of the BBB/BTB and good vascularization in U87MG xenografts. A [$^{13}$C]TMZ peak was detected at 3.9 ppm by HMQC from a selected volume of about 1.0 cm$^3$ within the brain tumor with a HMQC pulse sequences.

This study has clearly demonstrated noninvasive detection of [$^{13}$C]TMZ in

xenografted U87MG brain tumor with MRS. Noninvasive tracking of antineoplastic agents using MR spectroscopy will have a significant impact on brain tumor chemotherapy.

## II.1 Introduction

Malignant brain tumors have poor prognosis. This is due, in part, to poor drug delivery and the correspondingly limited therapeutic response caused by a partly intact blood-brain barrier (BBB), blood-brain tumor barrier (BTB), and reduced tumor blood flow[26]. Temozolomide (TMZ) is a relatively new alkylating agent that has been successfully used for chemotherapy of glioblastoma multiforme and anaplastic astrocytoma. The ability to monitor concentrations of the therapeutic agent within the tumor noninvasively over the course of chemotherapy is important to improve therapeutic strategies and/or to evaluate patient response to the treatment.

Magnetic resonance imaging (MRI) and spectroscopic imaging (MRSI) have a significant potential such applications. They can provide detection of the drug molecules as well as functionally monitor the anticancer effects of therapy repeatedly, with high spatial resolution, and no radiation exposure during the longitudinal course of therapy. TMZ is a good candidate for noninvasive monitoring by MRS because this compound can be labeled with a $^{13}C$ isotope in the methyl position, and can be detected *in vivo* with $^{13}C$ MRS at clinically relevant concentrations[27]. We previously demonstrated MR measurement of the intratumoral spatial distribution of carbon-13-labeled TMZ ([$^{13}C$]TMZ) in xenografted human breast carcinomas in mice using a heteronuclear multiple-quantum coherence (HMQC) pulse sequence[28] with gradient selection of coherence[29]. Since TMZ is currently approved for use in brain tumors, preclinical studies with a brain tumor model is a necessary step for clinical translation of the method. One major problem is that concentrations of the drug in brain tumors is generally lower than that in breast tumor models because of poor drug delivery. Combined with a less efficient MR setup for brain MRI/MRS due to the reduced filling factor of the RF resonator, this results in significantly reduced sensitivity of MRS to detect drug delivery in brain tumors. TMZ was successfully detected by HMQC *in vitro* at a concentration of about 100 µg/ml (0.5 mM [$^{13}C$]) with a signal-to-noise ratio (SNR) of about 11 for a nominal spatial resolution of 2.5 mm in-plane

(15.6 $mm^3$). A TMZ peak was also detected in *in vivo* HMQC spectra of a xenografted breast tumor post-intra peritoneal injection of [$^{13}$C]TMZ at a total dose of 45 mg/kg with the same nominal voxel size. In this study, to provide a necessary gain in detection sensitivity required for *in vivo* detection of [$^{13}$C]TMZ in brain tumor models, we performed a single-voxel spatially localized HMQC spectroscopy using outer-volume suppression[30], for spatial localization. To our knowledge, this is the first report for direct detection of drug molecules in xenografted brain tumors using an MR technique.

Quantitative measurement of tumor vascular parameters such as tumor vascular volume and vascular permeability-surface area product in preclinical models is typically performed using dynamic MRI with high molecular weight contrast agents, such as a conjugate of GdDTPA with albumin (albumin-GdDTPA)[31]. However, preliminary results obtained for brain tumor xenografts demonstrated a negligibly low uptake of albumin-GdDTPA in brain tumors as reported previously[32]. Also, high molecular weight MR contrast agents are currently not approved for clinical use. Conventional clinically approved low molecular weight MR contrast agents, such as GdDTPA, are more likely to distribute in brain tumors, and quantitative parameters of tumor vascularization that control drug delivery to the tumor can be obtained from the MR contrast agent kinetics in the tumor.

In this study, a combination of bolus tracking and contrast-enhanced dynamic MRI following two consecutive intravenous injections of low molecular weight contrast agent, GdDTPA, was used to extract vascular parameters of the tumor, such as vascular volume, blood flow, and an effective volume transfer constant for the contrast agent[33]. Noninvasive detection of TMZ in brain tumor-bearing mice following intra peritoneal administration of [$^{13}$C]TMZ was performed using an inverse detection HMQC pulse sequence with outer-volume suppression for volume selection.

## *II.2 Materials and Methods*

### II.2.1 Materials

[$^{13}$C]TMZ (99% $^{13}$C at the methyl position) was obtained from Cambrige Isotope Laboratories, Inc. (Andover, MA, U.S.A.).

3-(Trimethylsilyl)propionic-*2*,*2*,*3*,*3*-$d_4$ acid sodium salt (TSP) was obtained from Sigma-Aldrich Co. (St. Louis, MO, U.S.A.). Magnevist (GdDTPA) was obtained from Bayer Healthcare Pharmaceuticals, AG (Leverkusen, Germany). All other chemicals were of reagent grade, and were obtained commercially. Double-tuned volume coil ($^{1}$H/$^{13}$C) for 9.4T Bruker Biospec horizontal bore animal MR scanner was developed and built by Resonant Research LLC (Baltimore, MD, U.S.A.).

### II.2.2 Cell lines and animals

Human malignant glioma U87MG cell lines were grown in Eagle's minimum essential medium (EMEM) with 1% penicillin, streptomycin, and 10% fetal bovine serum at 37°C with 5% $CO_2$. Approval from the institutional animal care and use committee preceded all animal experiments in the present study. U87MG cells were inoculated intracranially in immune suppressed male SCID mice (body weight of approx. 22 g) that were purchased from NCI (Bethesda, MD, U.S.A.). Briefly, $1 \times 10^5$ cells in 2 μL of Hanks' solution were implanted by intracranial injection using stereotactic guidance. The skull was exposed, and a burr hole was drilled through the skull 2 mm lateral and 3 mm anterior to the bregma. Tumor cells were injected over 5 min into the brain parenchyma at a depth of 2.5 mm. After inoculation, the scalp was sutured. Three weeks following cell inoculation, animals with tumor sizes of over 3 mm were used for MR experiments. At least three mice were used for the experiments.

### II.2.3 In vitro MR study

MRI and MRS studies were performed with a horizontal bore Bruker Biospec 9.4T MR scanner equipped with 121 mm shielded gradient systems. The Paravision 3.0.2 program (Bruker Biospin GmbH) was used as acquisition software. A temozolomide phantom was prepared with 100

μM [$^{13}$C]TMZ in saline in a 15 mL plastic tube. [$^{13}$C]TMZ signals were measured using an inverse-detection HMQC pulse sequence with echo time (TE) = 20 msec; repetition time (TR) = 1500 msec; number of acquisition (NA) = 2048; dummy scan = 8. Three-dimensional volume selection was performed with a series of 6 slice-selective semi-adiabatic sech pulse (pulse width = 1 msec, excitation slice thickness of 16 mm) used for outer-volume suppression. A composite-pulse decoupling sequence, WALTZ-16 ($\gamma B_2$ = 1 kHz) set at $^{13}$C resonance frequency of [$^{13}$C]TMZ of 49 ppm, was used for broad-band decoupling of $^{13}$C during acquisition.

### II.2.4 In vivo MR study

Mice were initially anesthetized with ketamine/acepromazine mixture (50 mg/kg and 5 mg/kg, respectively, in saline) via intraperitoneal injection, and immobilized in a plastic cradle positioned within the double-tuned $^{1}$H/$^{13}$C RF coil, and the tail vein was catheterized for GdDTPA injection before placing the probe in the magnet. A second catheter was placed i.p. for injection of [$^{13}$C]TMZ solution. A 100 mM cylindrical TSP phantom was place on the head of the mouse, and used as an external reference. For the duration of MR experiment, animal was kept under gas anesthesia with 1% isoflurane in the flow of air (1 mL/min). Body temperature was maintained at 37°C by heat generated from a pad circulating with warm water. Mouse respiration was monitored with a dedicated small animal physiology monitoring system attached to the MR scanner.

Contrast-enhanced dynamic MRI — A slow injection of 30 μL of GdDTPA solution (167 mM in saline) over 3 sec was performed during $T_1$-weighted MRI scan of the mouse brain. Briefly, a saturation recovery snapshot-FLASH pulse sequence with an excitation pulse flip angle of 10 degrees, an TE of 1.245 msec, and three $T_1$ saturation recovery delays (250, 500, and 1,000 msec) were used, and an $M_0$ map with a recovery delay of 10 sec was acquired once prior to administration of GdDTPA solution. Either two or three slices were selected with the slice thickness of 2 mm. $T_1$ sequence was repeated 64 times, and GdDTPA was injected after 4 scans that provided pre-contrast as well as post-contrast quantitative $T_1$ maps. A second bolus injection of 40 μL of GdDTPA was performed during $T_{2*}$-weighted fast low-angle shot (FLASH) MRI scan to characterize vascular volume and perfusion in xenografted brain tumor and mouse normal brain. Acquisition

parameters were as follows: TE = 3.5 msec; TR = 333 msec for 3 slices, and 500 msec for 2 slices for temporal resolution of 1 sec per multislice image. The same slices were selected as for $T_1$-weighted acquisition, and acquisition sequence was repeated 300 times. For both experiments, in-plane spatial resolution of 0.125 mm ($128 \times 64$ matrix zero filled to $128 \times 128$, field of view = $16 \times 16$ mm) was used.

HMQC $^{13}C/^{1}H$ MRS — After completing dynamic MRI experiments, the probe tuning to $^{1}H$ and $^{13}C$ was rechecked, and tri-planar scout images were acquired to determine the position of the imaging slices. Initially, RF pulse power was adjusted to optimize HMQC spectroscopy of the TSP phantom. An outer-volume suppression with 6 slice selective sech pulse was implemented to select a cubic region of interest using graphical prescription routine. An automatic and manual shimming routines using a point-resolved spectroscopy (PRESS) method were consecutively used to shim the region of the TSP phantom and the tumor region of the mouse brain. HMQC MRS of brain tumor was performed before and after i.p. administration of [$^{13}C$]TMZ. Acquisition parameters were as follows: TE = 20 msec; TR = 1500 msec; NA = 256; sweep width (sw) = 4960 Hz; dummy scan = 8. Similar to the *in vitro* study, the HMQC pulse sequence was used for indirect $^{1}H/^{13}C$ MRS, and adiabatic pulse (sech, 1 msec) and a WALTZ-16 composite-pulse decoupling sequence were used for voxel selection by outer-volume suppression and broad-band $^{13}C$ decoupling, respectively. [$^{13}C$]TMZ (15.5 mM) was injected via i.p. catheter every 10 min up to a total of 1.0 mL. After acquisition, animals were sacrificed, and extracted brain tissues were individually immersed in cold formalin for 2 hrs, then 30% sucrose overnight for hematoxylin-eosin staining (Supplemental data; S. Figure 1).

### II.2.5 Data analysis

A MatLab™ (The MathWorks Inc.) script was used for the analysis of vascular parameters, and a custom-written software in the IDL™ programming environment (Research Systems Inc.) and CSX3 software developed by Dr. Peter B. Barker (The Johns Hopkins University) were used for the analysis of MRS data. Calculation of vascular parameters was performed using block circulant deconvolution with manual localization of a suitable arterial input function (criteria high peak and low time to peak)[34] .

The concentration of contrast agent is proportional to $\Delta R_2$, but the proportionality constant is specific for tissue, magnetic field, and contrast agent. As the proportionality constant is unknown, only relative CBV and CBF values are reported in this study.

## *II.3 Results*

### II.3.1 In vitro MR study

A single voxel spatially localized spectrum of a [$^{13}$C]TMZ phantom

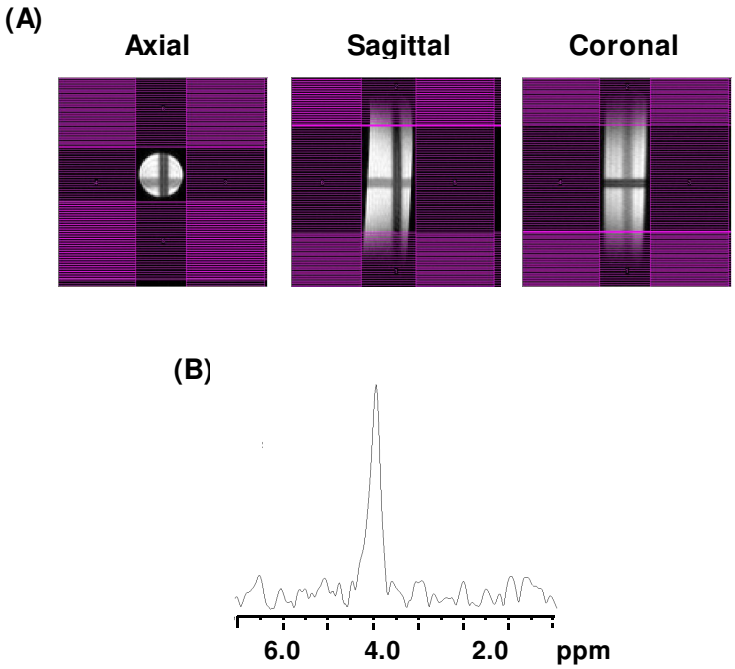


*Figure II.1: MR spectroscopy of 100µM [$^{13}$C]TMZ phantom using HMQC pulse sequence with adiabatic refocusing pulse. (A) Tri-planar images of TMZ phantom. Pink areas indicate the region of outer-volume suppression applied by adiabatic pulse (sech, 1 ms). Measurement volume is about 1.2 cm3. (B) Spectrum obtained from 100 µM [$^{13}$C]TMZ phantom. TE/TR = 20/1500 msec, NA = 2048, dummy scan = 8. Temporal resolution = 51 min. SNR = 26.8.*

prepared in a plastic 10 mm diameter tube is shown in Figure II.1.

Selection of the region of interest (ROI) with a volume of approximately 1.2 $cm^3$ was performed by a combination of 6 slice-selective semi-adiabatic hyperbolic secant (sech) pulses[30]. As shown in Figure II.1, we could reliably detect 100 µM of [$^{13}$C]TMZ in 1.2 $cm^3$ voxel *in vitro* in the phantom. The measured SNR was 26.8, and the acquisition time was 51 min. Complete suppression of the bulk water signal at 4.7 ppm was achieved in these *in vitro* experiments. For typical *in vivo* acquisition parameters with a relaxation delay of 1.5 sec and total acquisition time of 30 min with 1024 scans, the SNR was proportionately reduced to about 12.5 (data not shown). *In vitro* studies with a [$^{13}$C]TMZ phantom demonstrated the feasibility of this technique to detect [$^{13}$C]TMZ peak at 3.9 ppm *in vivo* in a xenografted U87MG brain-tumor model.

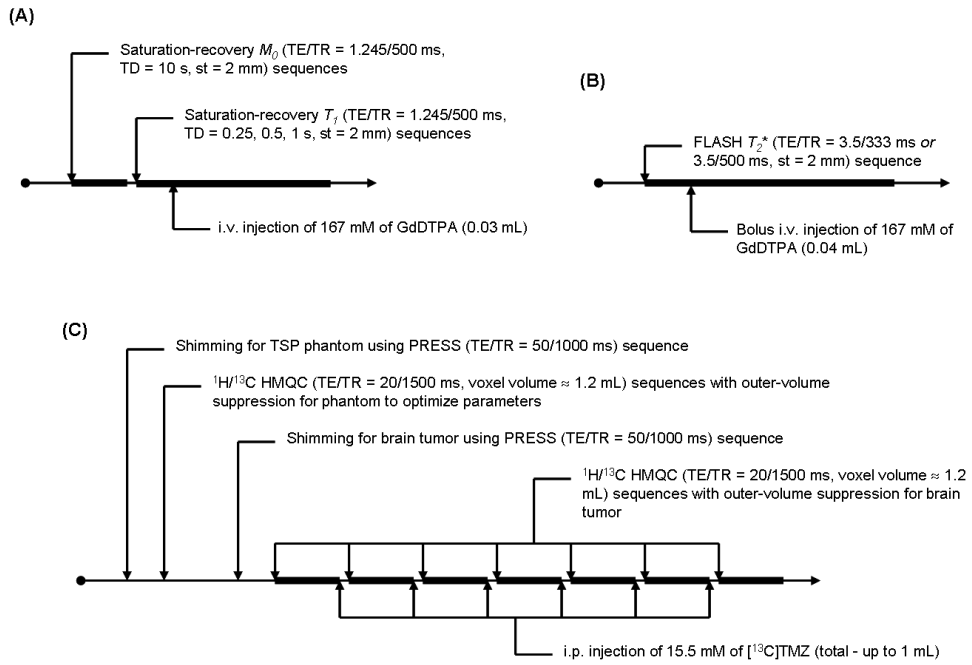


*Figure II.2: Experimental protocols for in vivo MRI/MRS studies. (A) $T_1$-weighted saturation-recovery MRI. (B) $T_2$-weighted FLASH MRI. (C) $^1$H/$^{13}$C HMQC MRS.*

### II.3.2 In vivo MRI for vascular parameters in xenografted U87MG brain tumors

Experimental protocols for MRI/MRS studies are summarized in Figure Error: Reference source not found. Experiments started with the first GdDTPA injection and the acquisition of quantitative $T_1$ maps from the tumor region of the brain (Figure Error: Reference source not foundA). $T_1$ measurement studies were followed by the bolus tracking experiment (Figure Error: Reference source not foundB), which demonstrated that the initial drop in $T_{2*}$-weighted MR signal quickly recovered in the normal brain while slow recovery was detected in brain tumors (Figure II.3). This is a common phenomenon typically observed in normal brain and brain

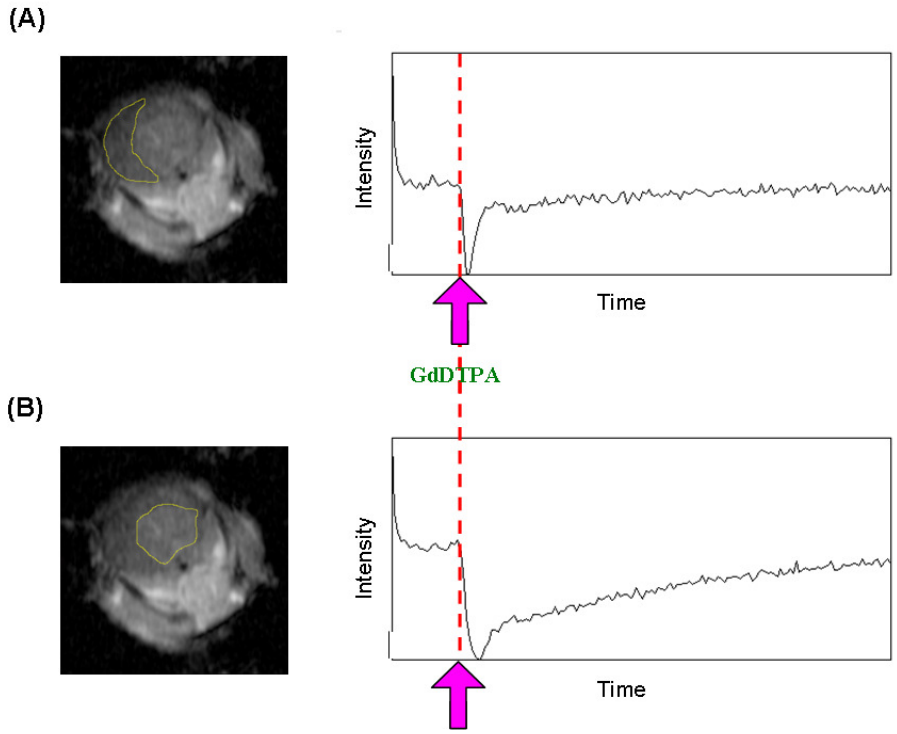


*Figure II.3: Changes in signal intensities of (A) normal brain, and (B) U87MG-xenografted tumor in mouse brain as shown in yellow regions in each image following GdDTPA injection. Images and intensity profiles are a representative of five experiments. Movie files are provided in supplemental data (S. Figure 2).*

tumors[35,36] . Complete or partial breakdown of BTB, and/or BBB in the tumor, and impaired tumor vascularization are two major factors contributing to this effect[36]. Typical reconstructed images of $\Delta R_1$ differences, cerebral blood flow (CBF), and cerebral blood volume (CBV) are presented in Figure II.4. Relative tumor blood flow (rTBF) (rTBF = TBF / CBF) and relative tumor blood volume (rTBV = TBV / CBV) values reconstructed from these maps are shown in Figure II.5. Both TBF and TBV were relatively higher than those in normal brain tissue, which indicates that U87MG tumors are well vascularized, have sufficient blood flow, and that permeability of the BBB and/or BTB within the tumor was significantly compromised.

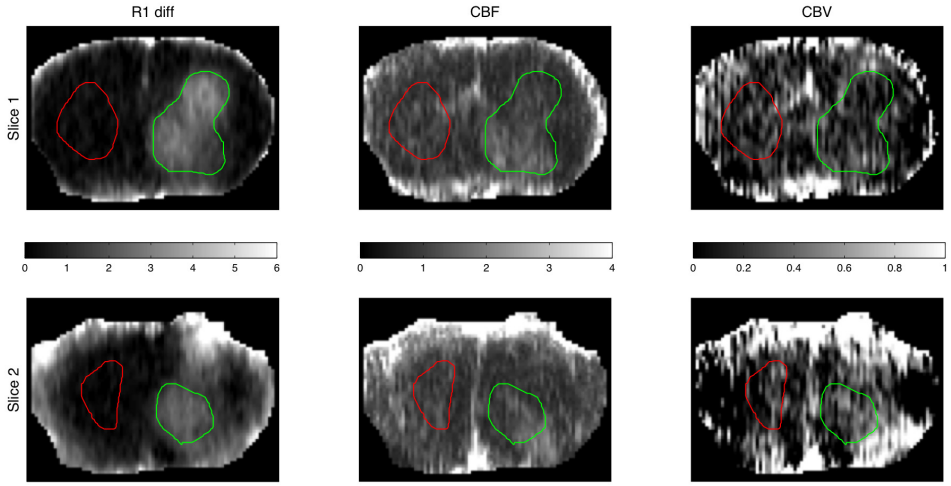


*Figure II.4: Images from one of the animals showing visible tumors. Left: R1 difference maps. Middle: Relative CBF maps. Right: Relative CBV maps. CBF and CBV were divided by the mean of the normal area. Green ROIs represent a region of the tumor tissue, and red ROIs represent a region of the normal brain tissue.*

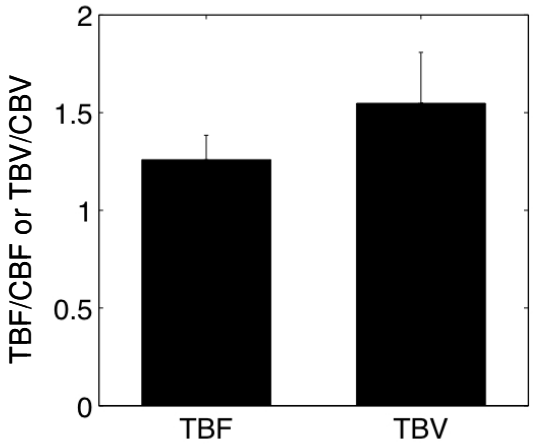


*Figure II.5: Ratios of TBF/CBF and TBV/CBV in the animals showing visible tumors. Bars represent standard error of the mean.*

### II.3.3 In vivo MRS of TMZ in xenografted U87MG brain tumor

After completing dynamic MRI studies with GdDTPA enhancement, inverse detection HMQC spatially localized single volume spectroscopy was performed as outlined in Figure Error: Reference source not foundC. Initially all acquisition parameters were adjusted for a cylindrical phantom filled with 100 mM TSP solution that was positioned next to the animal skull as shown in Figure II.6A. An indirect $^{1}H/^{13}C$ spectrum of methyl carbons of TSP is shown in Figure II.6B. Initial shimming (both automatic and manual) was performed for the TSP phantom region and a single TSP peak was clearly detected at 0 ppm with a composite-pulse decoupling sequence, WALTZ-16 ($\gamma B_2$ = 1 kHz) applied to the carbon-13 RF channel. Three-dimensional volume selection was performed as shown in Figure II.6C with 6 slice selective sech pulses. [$^{13}$C]TMZ peak was detected in the proton spectrum at around 3.9-4.0 ppm, and a natural abundance lipid peak was registered at 1.3 ppm. [$^{13}$C]TMZ peak was consistently detected in three tumor-bearing mice following i.p. injection of [$^{13}$C]TMZ, and reached its maximum amplitude at 30-50 min post initial injection of [$^{13}$C]TMZ. As for *in vitro* studies, an excellent suppression of the bulk water peak at 4.7 ppm was achieved in *in vivo* experiments using the HMQC acquisition

technique with gradient selection of coherences[29]. The detection of [$^{13}$C]TMZ peak in U87MG xenografted tumors was attributable to (i) the partial breakdown of BBB and (ii) well-vascularized character of U87MG xenografts, as demonstrated by dynamic MRI. This experiment corroborated the feasibility of noninvasive detection of delivery of $^{13}$C-labeled drug molecules to brain tumor using spatially-selective inverse detection HMQC-based MRS.

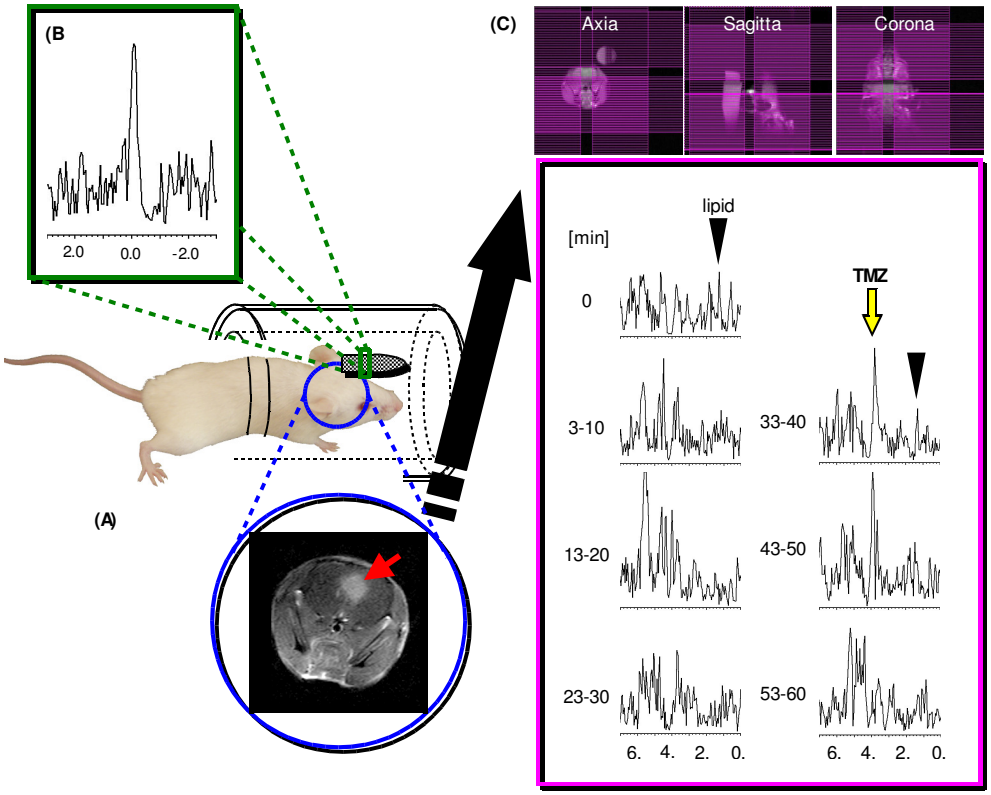


*Figure II.6: Illustration of the experimental setup for in vivo MRS, and spectra of the external reference, TSP, and the mouse brain pre- and post-intra peritoneal administration of [13C]TMZ at a total dose of 15.5 µmol. Pink areas in tri-planar images indicate the region of outer-volume suppression applied by adiabatic pulse (sech, 1 msec). Spectra of TSP and mouse brain are a representative of three experiments.*

## II.4 Discussion

Non-invasive detection of [$^{13}$C]TMZ in brain tumor by MRS allows repeated monitoring of TMZ during the course of therapy, which can provide a better opportunity to optimize the treatment plan by elucidation of the relationship between TMZ delivery and antitumor activity when combined with MRI. Although $O^6$-methylguanine-DNA methyltransferase (MGMT) is known to be associated with TMZ resistance, our preclinical animal studies with human breast cancer xenografts showed practically unchanged MGMT expression levels in tumors treated with TMZ[37]. In addition, minimal involvement of MGMT in TMZ resistance in glioma was reported by Bocangel et al.[38]. Similarly, there is no involvement of traditional multidrug resistance (MDR) drug-efflux pump mechanisms in TMZ resistance[39]. It was conceivable that changes in vascular parameters in tumor resulted in poor response to chemotherapy[37], which might be directly linked to delivery issue. The dynamic MRI results demonstrate that the U87MG tumors are well vascularized, which is also supported by an early report[40]. Furthermore, the $R_1$ difference maps show at least partial breakdown of the BBB. The rTBF/rTBV values (1.26/1.55) obtained are in good agreement with experimental results obtained for the high-grade gliomas in a recent arterial spin labeling (ASL)/dynamic susceptibility contrast (DSC) study[41]. Another study using only ASL showed decreased TBF and TBV in U87MG tumors in mice[42]. The inconsistency might be explained by differences in magnetic susceptibility between the tumor and normal brain tissue, which can be caused by differences in angiogenic state, vascular architecture, hematocrit and other factors[43]. The $T_1$ effect of GdDTPA leaking into the tissue via partly broken BBB or TBB can be a problem in DSC studies. In this study, the $R_1$ measurements were performed prior to DSC, and the gadolinium injected for the $R_1$ maps acted as a preloading for the DSC measurement which should minimize $T_1$ effects[44],[45].

We were able to detect [$^{13}$C]TMZ by HMQC at the volume of nearly 1.0 cm$^3$ in mouse brain tumor. To extrapolate our results to human studies, we also detected *N*-acetyl aspartate (NAA) peak in normal mouse brain (voxel size of 0.064 cm$^3$) as well as in normal human brain at 3.0T (voxel size of 16 cm$^3$) (Supplemental data; S. Figure 3). From a comparison of both SNR of NAA peak in mouse/human normal brain and SNR of [$^{13}$C]TMZ peak in

mouse brain tumor and phantoms, it should be possible to detect [$^{13}$C]TMZ peak in human brain tumors at concentrations of about 100 nM, which is close to the reported maximal concentration of TMZ in plasma (about 10 μg/mL) and cerebrospinal fluid (about 50 nM)[46]. These results support the potential feasibility of MRI technology for direct detection of the brain tumor chemotherapy in clinical settings.

The technique used here is designed to monitor drug delivery, and not for acquisition of spatial distribution unlike the previous report[29]. The limitations of spatial distribution of drugs in brain tumors are attributed to insufficient drug delivery and relatively small tumor size compared to other solid tumors. This study has clearly demonstrated noninvasive detection of [$^{13}$C]TMZ in xenografted U87MG brain tumor with MRS. Although it is also possible to use the pharmacokinetics of an appropriate surrogate marker of drug delivery, such as GdDTPA, with MRI to follow and predict the delivery pattern of the drug to the tumor, this method has limited feasibility for brain tumors with partly functional TBB. Unlike MR contrast agents, many anticancer agents used for brain cancer therapy including TMZ can penetrate BBB, and their pharmacokinetics in the tumor can be vastly different from the surrogate molecules such as GdDTPA. The major advantage of MRS is the direct monitoring of drug molecules, in this case, TMZ. We envision that noninvasive monitoring of [$^{13}$C]TMZ in brain tumors by spatially-selective inverse detection HMQC-based MRS will lead to more effective strategies for brain tumor therapy.

## *II.5 Acknowledgments*

The authors are very grateful to Dr. Bachchu Lal for his teaching of brain tumor cell inoculation. The authors thank Dr. Zaver M. Bhujwalla and Dr. Arvind P. Pathak for their helpful discussions and critical reading the manuscript.

## II.6 Supplementary figures

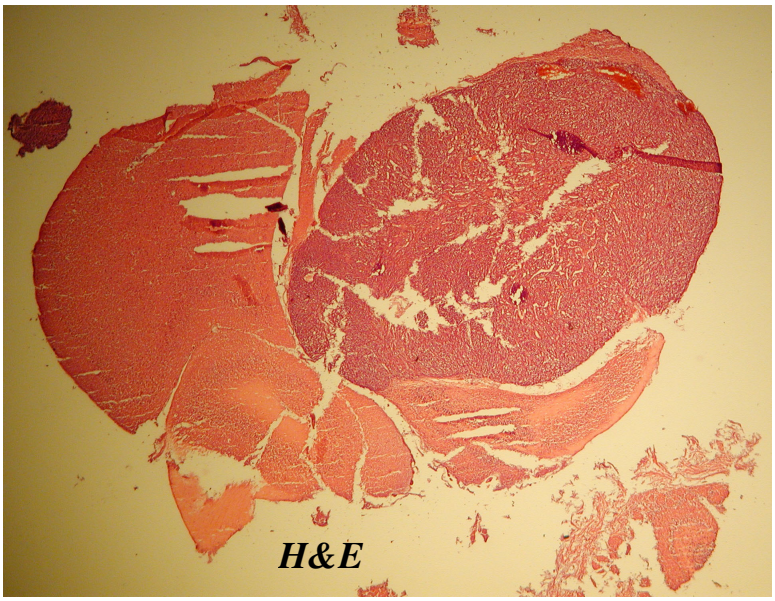


*S_Figure 1: Brain tissue section stained with hematoxylin and eosin. Brain tissue was carefully removed from the skull, and extracted brain tissues were immersed in formalin, followed by 30% sucrose as a cryoprotectant. Each brain was embedded in Tissue-Tek® O.C.T. Compound (Sakura Finetek U.S.A., Inc.), frozen with liquid nitrogen, and stored -80□C until microscopy. Nikon Eclipse E400 upright microscope equipped with Nikon super-high-pressure mercury lamp and SPOT Insight™ digital camera (Diagnostic Instruments, Inc.) was used for microscopy. 2X Lens. Tissue slice thickness = 10µm*

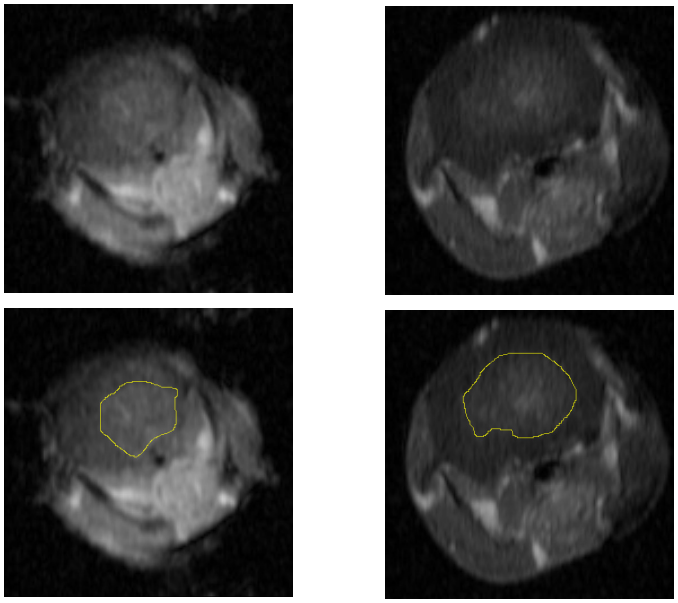

*S_Figure 2: Changes in signal intensities of normal brain and U87MG xenografted brain tumor following bolus i.v. injection of 167 mM of GdDTPA (0.04 mL). Images were acquired using $T_2$-weighted FLASH sequences. Images were reconstructed using IDL™ program Tumor regions are outlined in yellow. One representative slice was extracted from two or three slices in each animal, and movies are two representatives of five animals.*

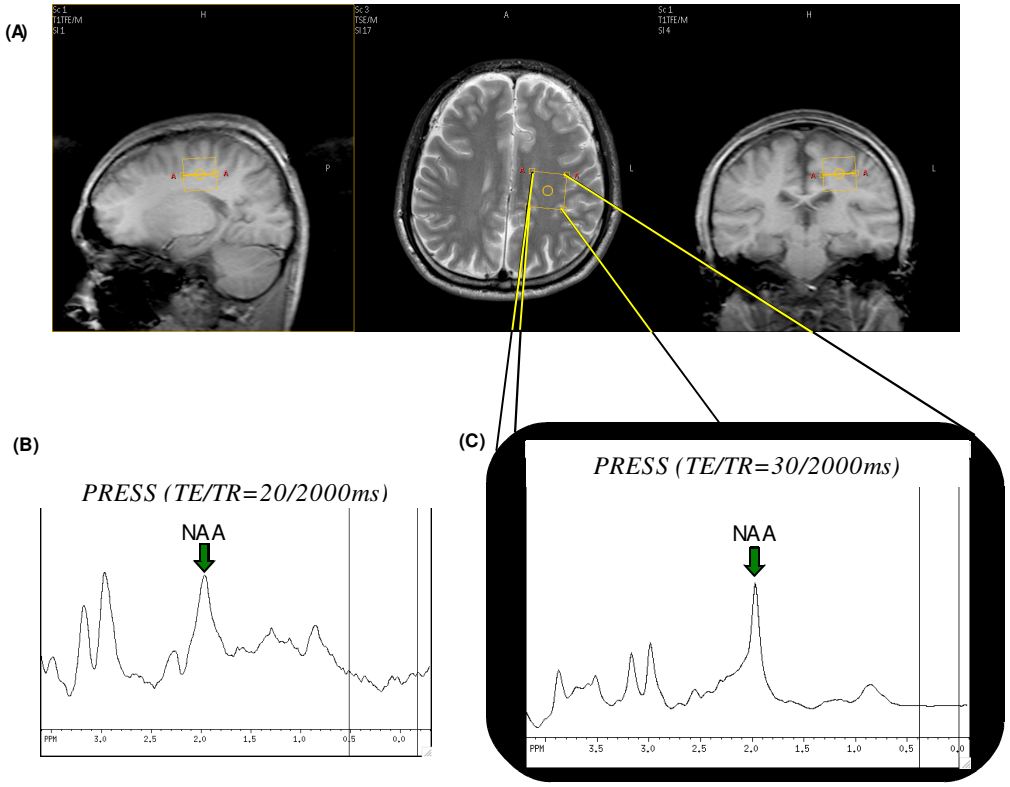


*S_Figure 3: Comparison of internal standard peaks of N-acetyl aspartate (NAA) in normal mouse brain and healthy human brain. (A) Tri-planar images of healthy human brain with a 2.5x2.5x2.5 cm cubic voxel indicators. (B) NAA peak obtained from a normal mouse brain acquired by point-resolved spectroscopy (PRESS) sequence (TE/TR = 20/2000 msec) at Bruker 9.4T spectrometer. A voxel size was about 0.064 $cm^3$. SNR was calculated to be 9.5. (C) NAA peak obtained from a healthy human brain acquired by PRESS sequence (TE/TR = 30/2000 msec). A voxel size was about 16 cm3. SNR was calculated to be 98. A STEAM (Stimulated echo acquisition mode, TE/TR = 20/2000 msec) sequence was also tried for MRS of NAA in a human subject, and SNR was calculated to be 42 (data not shown). The same NA was used in all experiments. An MRS experiment for a human subject was performed at Philips clinical 3.0T scanner, and an 8-element SENSE™ head coil (Philips Medical Systems, Andover, MA, U.S.A.) was used. Prior to the experiment, a written informed consent was obtained from a subject.*

# Manuscript III dCE MRI of breast tumors

Perfusion and vascular permeability have been studied in a transgenic mammary cancer model (PyMT) at two different stages, the initial hyperplastic and the late carcinoma stage. This was achieved by using Tikhonov deconvolution and Patlaks method. It was shown that $T_1$ weighted contrast enhanced MRI can be used to estimate perfusion and leakage parameters from a single scan.
All tumors were well perfused. Significant differences in the time it takes the contrast agent to traverse the vasculature (Mean Transit Time – MTT) were found between tumors and reference tissue as well as between the hyperplastic and late tumor stage. Vascular permeability and blood volume were significantly decreased in late stage tumors compared to hyperplastic stage. The changes in permeability, blood volume and MTT may indicate vascular maturation over time.

## *III.1 Introduction*

As a tumor reaches a size of 1-2mm$^3$ its need for oxygene can no longer be met by passive diffusion. The tumor therefore emits signaling molecules which stimulate surrounding vessels to grow into the tumor. It has been shown that the microvascular density (MVD) of a tissue is a good indicator of angiogenesis[47]. Unfortunately the spatial resolution of MRI does not allow MVD to be measured directly and the tortoisity of tumor vessels make flow measurements impractical. A better method for quantifying

angiogenesis with MRI is to measure perfusion. It is important to distinguish blood flow and perfusion. Blood flow is a measure of how much blood flows through a vessel per time unit. Perfusion is a measure of how much blood is available for exchange of oxygen, nutrients and waste products to the tissue. The purpose of angiogenesis is not flow per say but rather to exchange nutrients and deliver oxygen to the tumor cells. Thus, perfusion is an obvious choice for monitoring the efficiency of angiogenesis.

Tumor vessels are more permeable to contrast agents than normal vessels[48]. The permeability is a consequence of big pores between endothelial cells and a lack of basal membrane. At different stages of tumor development the distribution of endothelial cells may change. Hence, permeability of the vessels can be used to estimate the maturity of the vessels.
In the transgenic model originally described by Guy et al[49]. in 1992, the oncoprotein expression (polyoma middle T antigen (PyMT) is under the control of mouse mammary tumor virus LTR (MMTV LTR). The expression of PyMT is therefore restricted to the mammary epithelium. PyMT is a membrane-attached protein and encoded by the small DNA polyoma virus. PyMT is not expressed in human cells. However, it acts as a potent oncogene because its products binds to and co-opts several signal transduction pathways, which are altered in human breast cancers[50]. The PyMT model mimics many processes found in progression of human breast cancer. It does not only mimic the morphological pattern but also the expression of biomarkers associated with poor prognosis.
PyMT induces a stepwise progression into malignancy similar to that of human breast cancer, featuring hyperplasia (normal/benign), adenoma (ductal carcinoma in situ), early to late carcinoma with stromal invasion (locally invasive carcinomas), and late carcinoma with distant metastasis. The stages have been described in detail by Lin et al[51] and Maglione et al[52]. Multiple mammary tumors are present at the hyperplastic stage (4-6 weeks of age) where the mice develop palpable mammary tumors that involve the entire mammary fat pad. These carcinomas are generally highly fibrotic, with dense connective tissue separating individual nests of tumor cells. The following stage of adenoma is characterized by cellular proliferation which fills and expands closely packed acini and ducts and, increasing the size of primary tumor (7-9 weeks of age). Most of the tumor appears to have an intact basement membrane. Although tumors at the hyperplastic

stage have very few leukocytes in the surrounding stroma, some adenoma lesions do contain foci of leukocytic infiltration in the vicinity of the tumor. These infiltrates are composed of neutrophils, macrophages and fibroblasts. An increased vascularity is also observed at these sites.
The early carcinoma stage (9-11 weeks of age) is characterized by greater cytological atypia and the identification of early stromal invasion. In these areas of transition to malignancy, the tumor cells now appear pleomorphic, showing a moderate variation in nuclear morphology, size, and shape. There is also a high density of leukocytic infiltration surrounding the tumor acini. Late carcinomas (12-14 weeks of age) consist of solid layers of malignant cells with marked variation in cell shape, size, and nuclear morphology. The invasive tumor cells are associated with a reactive stroma, which consists of fibroblasts and leukocytes.
This development with these stages makes the PyMT model an excellent model in which progression of mammary cancer can be studied. It is also a good model in which important principles of tumorgenesis can be understood.
A range of different studies have correlated dynamic MRI parameters with angiogenic markers. Wedam et al[53] and Gossmann et al[54] showed a decrease in permeability and vascular volume after treatment with an anti-VEGF agent. In other studies permeability[55], and blood volume[56] have been correlated with MVD. Dynamic MRI has also been used to distinguish benign from malignant tumors[57,58].
The aim of this study was to explore the development of a spontaneous tumor model. More specifically the aim was to compare perfusion and permeability parameters at the hyperplastic and late carcinoma stages using dynamic contrast enhanced MRI.
The studied parameters were perfusion (BF), permeability ($K_i$), plasma volume($V_p$), distribution volume ($V_d$), and mean transit time (MTT). $V_p$ is the volume of blood plasma confined to the vessel. $V_d$ is the total volume in which the contrast agent can be distributed. MTT is the average time it takes for a contrast agent molecule to traverse the vasculature. These parameters were obtained using Tikhonov deconvolution[59] and Patlaks method[60]. In order to perform both an aquarate arterial input function (AIF) is required, which means that the slice selected for dynamic MRI should contain both tumor and vessels.

## III.2 Materials and methods

### III.2.1 Animal procedures

All procedures were conducted in accordance to the Danish Animal Experiments Inspectorate (2007/561/1353). Two groups of female PyMT mice (n=4 in each group) were anaesthetized with 5% isoflurane and a tail vein catheter was inserted. (Needle size 25 G, catheter size 0.4 mm ID 0.8 mm OD (Astra)). Group 1: age 5-6 weeks, weight was approximately 20-25 g. Group 2: age 12-14 weeks, weight was approximately 30-35 g. During MR examination the animals were kept anesthetized using 0.8% isoflurane in a mixture of 0.25 l/min oxygen and 0.75 l/min air.
All animals were kindly provided by Dr. Lars H. Engelholm from the Finsens Laboratory, Copenhagen University Hospital, Rigshospitalet.

### III.2.2 Magnetic resonance imaging

All imaging was performed using a home built volume quadrature coil with an inner diameter of 40mm in an experimental 4.7T Varian Inova system suitable for imaging small animals.
All images were acquired using a 35x35 mm field of view. After initial scout and planning images, three 2mm axial angiograms were acquired using a 2D time of flight gradient echo sequence (TR/TE 13/8.5 ms, matrix 128x128). Based on the scout and angio images a suitable slice including both tumors and vessels was selected for dynamic MRI.
High resolution $T_1$W images were acquired before contrast injection (TR/TE 300/14ms, matrix 256x256, Five 2 mm slices, 2 avg) and were used to verify the selection of the dynamic MRI slice.
A saturation recovery gradient echo sequence was used to measure initial $T_1$ before bolus and subsequent dynamic imaging of the first pass of the bolus through the tumor tissue. A 90 degree prepulse followed by gradient spoilers was used and after a saturation delay (TD) the echoes were read out using centric phase ordering and 30 degree flip angle. TR/TE were 18/3.7ms. The scan matrix was 128x64 and the field of view (FOV) 35x35mm resulting in an inplane resolution of 0.27x0.55mm. One 2 mm slice was acquired. For precontrast $T_1$ determination saturation delay was varied (TD=150,300,450,600,750,900,1050,1200,1350,1500,1650,1800, 2500,4000ms) and data acquired with 5 averages.

The passage of the bolus was followed for 10 minutes using a TD of 150ms and 1 average with a time resolution of 1.3s. After the first 50 frames 0.0019 mmol Magnevist (equivalent to 0.0625 mmol/kg for a 30g mouse) was injected in the tail vein of the mouse. Immediately following the dynamic scan postcontrast $T_1$W images were acquired.
In order to relate the change in MR signal to concentration of contrast agent, single point estimates of $\Delta R_1$ were performed during bolus passage. In order to achieve this basis $T_1$ and $M_0$ were measured prior to contrast agent injection.

### III.2.3 Processing

The signal as a function of time for a gradient echo sequence with a 90 degree prepulse can be formulated as:

$$s(t)=M_0\sin(\alpha)\left(1-e^{-TD\cdot\left(R_1+\Delta R_1(t)\right)}\right),\ \ \Delta R_1(t)=r_1\cdot C_t(t) \quad [1]$$

where s(t) is the signal as a function of time, $M_0$ is the equilibrium magnetization, α is the flip angle, $r_1$ is the relaxivity of the contrast agent, and Ct(t) is concentration of contrast agent as a function of time.
The relaxivity of Gd-DTPA at 4.7T was set to 3.8 $s^{-1}$ $mM^{-1}$ based on relaxivity measurements on the same scanner (unpublished data). Equal relaxivity was assumed for the intravascular compartment as well as tissue. Precontrast $R_1$ and $M_0$ were fitted using equation 1 with $\Delta R_1=0$ using nonlinear least squares fitting method[22] implemented in Matlab (The MathWorks Inc). $C_t(t)$ was found using equation 1 as previously described[61,62].
Regions of interest (ROIs) were drawn in each tumor and a reference ROI was drawn in muscle. The regions were drawn using the high resolution pre and postcontrast $T_1$W images and were confirmed using $R_1$ and $M_0$ maps. A pixel for extraction of the AIF was manually selected based on rapid increase of the MR signal following contrast agent injection, large maximum peak and quick washout of the contrast agent.

Permeability
Vascular permeability for Gd-DTPA was mapped pixelwise using Patlaks method[60] assuming that the Gd-DTPA is 'trapped' in the tissue during the duration of the experiment. Values from all ROIs were pooled and histograms generated. Each histogram was divided by the number of points

included in the histogram and converted to percentage.
The working equation for Patlaks method is:

$$C_t(t) = K_i \int_0^t C_p(\tau)d\tau + v_p C_p(t) \quad (2)$$

Where $C_p$ is the concentration of contrast agent in the vessels (AIF).
It can be linearized as follows:

$$\frac{C_t(t)}{C_p(t)} = K_i \frac{\int_0^t C_p(\tau)d\tau}{C_p(t)} + V_p \quad (3)$$

If the assumptions of the model hold, $\frac{C_t(t)}{C_p(t)}$ can be plotted against $\frac{\int_0^t C_p(\tau)d\tau}{C_p(t)}$ and the slope of the plot will equal the unidirectional transfer constant $K_i$, whilst the intercept will equal the plasma distribution volume $V_p$. When fitting $V_p$ and $K_i$ the initial 150 points were excluded until linearity was obtained.

Perfusion

Blood flow (BF) and distribution volume ($V_d$) were obtained after averaging each ROI. Averaging was used to increase signal to noise of the $C_t(t)$ curves. Furthermore, Tikhonov deconvolution is computationally requiring which means that pixel by pixel estimates of BF and $V_d$ were not practical. Deconvolution was performed as described by Larsson et al[63]. In short the tissue curves were deconvolved with the AIF using Tikhonov regularization[59] with automatic selection of regularization degree based on the curvature of the L-curve. The result of the deconvolution is a fitted tissue curve ($C_t(t)$) as well as the residue impulse function multiplied by perfusion. The residue impulse function describes the amount of tracer which is left in the vasculature as a function of time. Ideally the initial value of the residue funtion is 1 and the last value 0.
Perfusion (BF) was calculated as the maximum value of the flow times residue impulse function, while MTT was calculated as the area under the residue impulse function. Distribution volume was then calculated based on

the central volume theorem as BF x MTT.
Statistical significance was tested using students T-test and a significance threshold of 0.05. $K_i$, $V_p$, BF, $V_d$ and MTT values from each tumors stage were compared to the reference tissue (muscle). Further, hyperplastic and late carcinoma stage were compared.

## *III.3 Results*

Permeability and plasma volume

Permeability $K_i$ and plasma volume $V_p$ were calculated using Patlaks method. All $K_i$ and $V_p$ values from hyperplastic and late stage tumors, as well as the values from the muscles as control were pooled. Based on the pooled values histograms of their distribution were generated. Each histogram was divided by the number of points it was based on, so the Y-axis indicates percentage of pixels at the given X-value.

Figure III.1 shows histograms of permeability and plasma volume for muscle, hyperplastic and late carcinoma stages.
Hyperplastic stage tumors show a more homegenous distribution of $K_i$ than late stage carcinomas. This is also reflected in the mean and median values which are higher for the hyperplastic stage (figure III.2). Permeability for muscle is quite uniform and is similar to permeability of the late stage tumors.
The plasma volumes for muscle are quite uniform compared to both tumor types. The hyperplastic stage tumors show two distinct distributions of $V_p$. The late stage tumors show one lower distribution. Figure III.2 display the mean permeability and plasma volume in the different tissue ROIs.

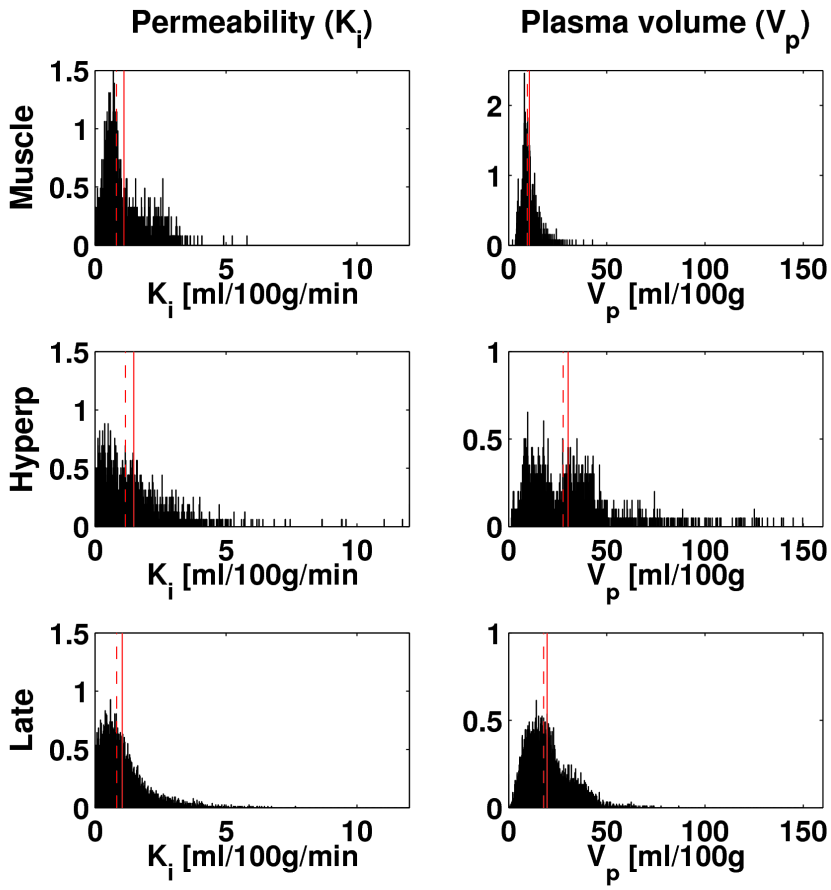


*Figure III.1: Histograms of permeability and plasma volume for the different ROIS. All $K_i$ and $V_p$ values from hyperplastic and late stage tumors, as well as the values from the muscles as control were pooled. The percentage of points is displayed as a function of $K_i$ or $V_p$ value. The vertical lines indicate median (dashed) and mean (solid) values.*

The permeability of hyperplastic stage tumors (1.5±0.04ml/100g/min) is increased compared to muscle (1.1±0.02ml/100g/min) and late stage tumors (1.0±0.01ml/100g/min) and both differences are significant with P-values <0.001. There is a significant difference between late stage tumor permeability and muscle (P<0.02). The plasma volume for both hyperplastic (30±0.5 ml/100g) and late stage tumors (20±0.1 ml/100g) is significantly larger (P-values <0.001) than the plasma volume for muscle (11±0.1 ml/100g). The plasma volume of the late stage tumors is significantly lower (P<0.001) than in the initial hyperplastic stage.

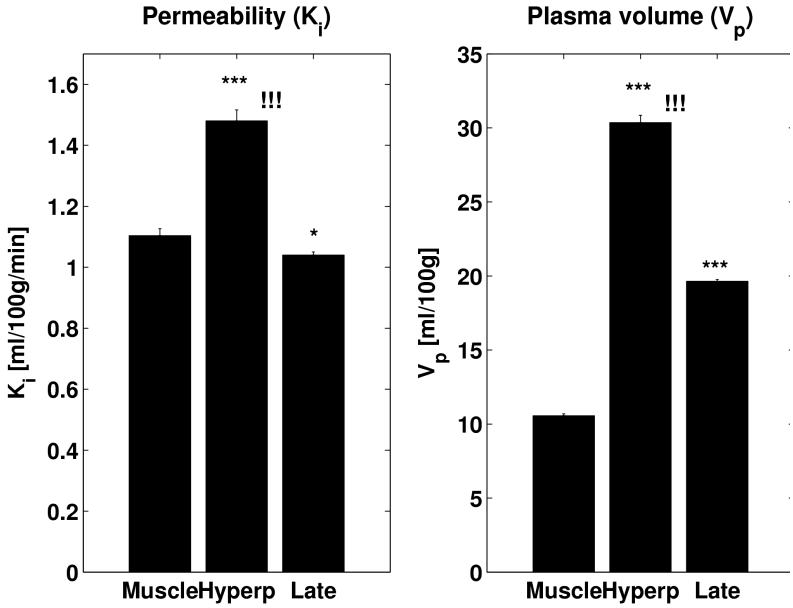


*Figure III.2: Permeability ($K_i$) and plasma volume ($V_p$) in the different ROIs. Bars are standard error of the mean (SEM). * indicates significant difference from muscle with P<0.05, *** indicates P<0.001 . !!! indicates significant difference between hyperplastic and late stage with P<0.001.*

Perfusion, distribution volume and MTT

Figure III.3 show BF, $V_d$ and MTT as a function of tissue type.

Perfusion values were 7±1 ml/100g/min in muscle, 86±25 ml/100g/min in hyperplastic stage tumors and 82±6 ml/100g/min in late carcinomas. Perfusion is significantly different in both tumor stages compared to muscle (P<0.01).

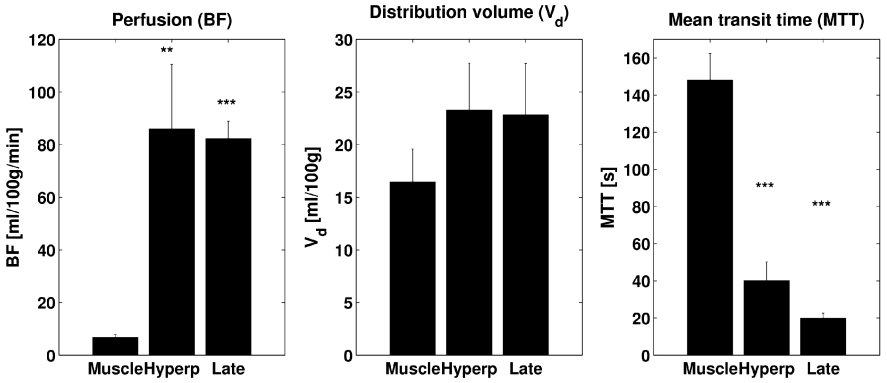


*Figure III.3: Mean perfusion, distribution volume and transit time for the different groups. Bars are SEM. ** denotes significantly different than muscle P<0.01, *** P<0.001.*

Both tumor types have a larger distribution volume (23±4/23±5 ml/100g) than muscle (16±3ml/100g), although not significantly different (P>0.2). MTT values were 148±14s for muscle, 40±10s for hyperplastic and 20±3s for late carcinoma stages. MTT is significantly lower than muscle for both hyperplastic and late stage tumors (P<0.001). Late stage tumors have shorter MTT than early stage tumors. If it is assumed that late stage tumors have shorter MTT than early stage tumor, a one-tailed T-test can be applied and result in signifcant difference (P<0.05, not indicated in the figure).

Representative examples

Figure III.4 displays representative examples of $T_1$ weighted images pre and post contrast together with parametric maps of $K_i$ and $V_p$. Hyperplastic stage tumors are less well defined and smaller than late stage tumors. Permeability is larger in the initial stage than in the late stage whilst blood volume is approximately the same.

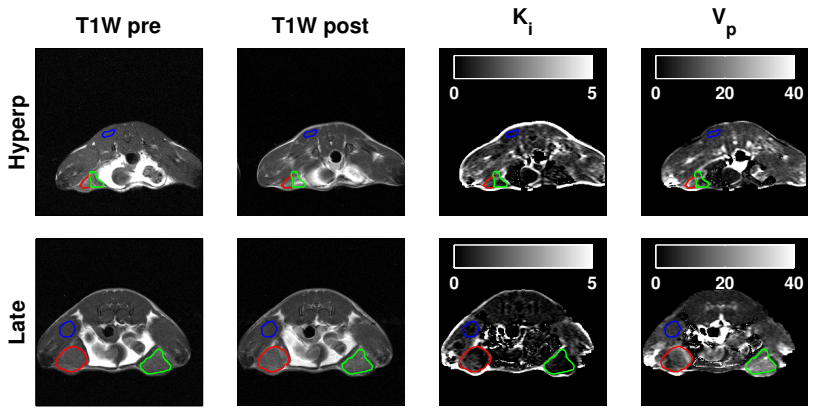


*Figure III.4: Example images and parametric maps of two animals from hyperplastic and late stage groups, respectively. $T_1$ weighted images are shown pre- and post-contrast. Parametric maps of $K_i$ and $V_p$ are displayed. The scale for $K_i$ and $V_p$ is 0-5 ml/100g/min and 0-40 ml/100g respectively. ROIs indicating tumors (red and green) and muscle (blue) are overlaid on the images.*

Figure III.5 shows $C_t$ as a function of time together with the fitted perfusion curve in the top row. The second row shows the residue function as a function of time. Representative pixels from each of the different ROIs are shown in the bottom row together with $K_i$ (slope) and $V_p$ (intercept). The same animals were used as examples in figure III.4 and III.5.

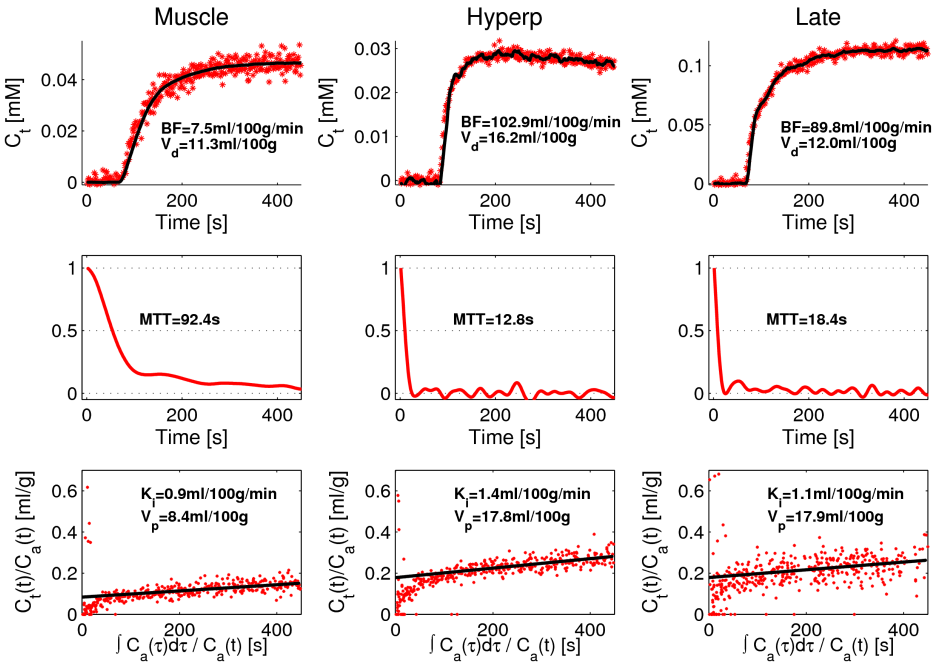


*Figure III.5: Perfusion, residue impulse function and Patlak plots for the different ROIs shown in figure 1. Top row: $C_t(t)$ as a function of time together with fitted perfusion curve. Middle row: Residue impulse function of time together with MTT. Bottom row: Patlak plots from a representative pixel within each ROI together with estimated $K_i$ and $V_p$. Each plot is from the same animals as shown in figure III.4.*

## III.4 Discussion

The PyMT transgenic mice is a transgenic breast cancer model that exhibits a high frequency of pulmonary metastasis and the tumor formation in this model has a short latency. This mouse model has been used extensively because it shares many characteristics with human breast tumors. First, tumors develop with high penetrance and show gradual loss of estrogen and progesterone receptors[51]. Second, the multistage progression from hyperplasia to a full-blown malignancy is represented in MMTV-PyMT mice.

The process of formation of new blood vessels plays a crucial role in local

tumor growth. In the PyMT model of mammary cancer the angiogenesis precedes transformation of mammary hyperplasia to malignancy[51,52]. Tumor progression is characterized by an initial ‘‘avascular phase’’ when the tumors are small and usually lacking activity with diffusion being the major way to support their metabolic needs. In the subsequent ‘‘vascular phase,’’ the development of a unique tumor vasculature is required for the increased metabolic demand of tumors that have grown beyond a certain size.
The microvasculaturity has been extensively investigated in tumor whole-mounts from the PyMT model[52]. In short, the blood vessels associated with atypical foci has larger diameters, a more irregular distribution and display more tortuous courses. The number of vessels decreases relative to the epithelial area during tumor development. The hyperplasia and the tumors are not equally perfused which is supported by the presence of necrotic areas in the early and late stages of carcinoma[51,64].
In this study we have used a $T_1$W dynamic contrast enhanced method to measure perfusion and leakage parameters. We have shown that it is possible to obtain quantitative permeability and plasma volume maps from first pass dynamic MRI scans in PyMT breast tumors using two different methods (Figures III.4&III.5). The distribution of permeability was different for hyperplastic and late stage tumors (Figure III.1 left column). Hyperplastic tumors show a larger heterogeneity in permeability and have a higher median and mean permeability than the late stage tumors. This may indicate elimination or maturation of immature vessels over time which would also explain the reduction in plasma volume as shown in figure III.3. The permeability values obtained in this study are low compared to the permeability measured in human breast tumors[58,54]. However, the human studies typically use low time resolution measurements and Tofts generalized model which fits both the early inflow and late efflux phases[33]. We used a unidirectional leakage model assuming that Gd-DTPA primarily leaks out of the vessel and does not return within the study period. Because of the high time resolution employed this assumption should be valid, according to Ewing et al[65]. Ewing found that unidirectional fitting tended to underestimate $K_i$ and overestimate $V_p$ for the late/low time resolution measurements, compared to bidirectional fitting. During the first 5-8 minutes the correlation between results obtained using uni- and bidirectional fitting were good.
To our knowledge, this study is the first to quantify perfusion and permeability in the PyMT tumor model. The permeability values we find

are close to what Larsson et al[66] found in human brain cancers with low permeability using the same method. Normal brain is different from mammary tissue because of the blood brain barrier. When the blood brain barrier is broken down during tumorgenesis the tumor tissue resembles body tumors such as mammary carcinomas.
Larssons group found that $V_d$ is expected to be larger than $V_p$ for permeable vessels as $V_d$ includes the extracellular leakage space. This association was seen for muscle in which $V_d$ is 16 ml/100g/min and $V_p$ is 11 ml/100g/min. This difference is significant ($P<0.001$). In late tumors, the differences between $V_p$ and $V_d$ are not significant which verifies the finding of low permeability in the two tumor groups. It would be very interesting to compare future measurements of permeability and blood volume with histology estimates of MVD and vascular permeability to validate the method.
The tumors are well perfused (figure III.3) and no significant differences in BF or $V_d$ were found between hyperplastic and late stage tumors. MTT was lower for late stage tumors than for hyperplastic stage tumors. Maturation of the vessel bed or elimination of immature vessels may explain the observed reduction in MTT.
We measured perfusion values of 86 ml/100g/min for hyperplastic stage and 82 ml/100g/min for late stage carcinomas, which is in good agreement with the Makket et al who found a perfusion of 84ml/100g/min in human breast cancers. We found a plasma distribution volume of 23 ml/100g in both typers, were Makket found 32 ml/100g. MTT was measured to 40s in hyperplastic stage and 20s in late stage tumors. Here Makket found a MTT of 28s which is comparable to our findings in late stage tumors.
Makket also estimated permeability based on the ratio between late and early stage plateau in the residua curve[67]. We have not used this method, but very few of the residue impulse functions displayed a second plateau which confirms the low permeability found using Patlaks method.
The angiogenesis of breast cancer has been examined with MRI in both preclinical models and in patients. As mentioned in the introduction perfusion MRI has been widely used to detect angiogenesis and the results have been correlated with conventional angiogenesis markers (VEGF and MVD).
Galbraith et al[68] used preclinical studies of the effects of Combretastatin to select the most optimal time point to monitor treatment in patients. Other studies showed that anti-VEGF treatment can change microvessel

permeability as early as 90 min after first dose although anti-VEGF drugs are thought to act over a much longer period[69,54]. This information was later used to design human studies. Similarly, our results could provide a basis for early diagnosis of cancer and distinguishing tumor stages in the clinic.

## *III.5 Conclusion*

We show that $T_1$ weighted dynamic contrast enhanced images can be used to estimate perfusion and leakage parameters from a single scan. It is further shown that early tumors are more permeable to Gd-DTPA and that the MTT is longer in hyperplastic than late stage tumors. These results indicate that the vessels in PyMT tumors mature over time making them less permeable and that this decline in permeability results in a decrease in MTT. Dynamic contrast enhanced MRI in animals holds great promise for gaining new knowledge about the effects of anti-angiogenic drugs and to monitor the development and maturation of angiogenic vessels during tumorgenesis.

# Manuscript IV *In vivo* cell labeling

## *IV.1 Introduction*

The permeability of cell membranes may be temporarily increased by exposing cells to pulsed high electric fields. When the trans-membrane potential induced by the pulsed field exceeds a certain threshold, a molecular rearrangement of the cell membrane occurs leading to the formation of trans-membrane pores, dramatically increasing cell permeability to ions and even macromolecules. Depending on the electric field applied, the process may be reversible and the pores can resolve with the permeability returning to its original value. This process, known as electroporation, has become an established *in vitro* technique used to introduce DNA or therapeutic genes into cells[70]. This technique has been used in treatment of many diseases including cancer, multiple sclerosis and inflammation following organ transplantation. It is also undergoing clinical testing as a means of enhancing delivery of chemotherapeutic drugs[71,72]. Preclinically it has been used to deliver anti-angiogenic drugs to tumors[73].

Electroporation has also been used to label cells *ex vivo* for cell tracking using magnetic resonance imaging[74,75,76,77]. The ability of electroporation to deliver extracellular paramagnetic contrast agents intracellularly[78] makes it possible to probe the compartmentalization of MR detectable metabolites. This is possible due to the relaxation effects of a paramagnetic gadolinium containing chelate on the metabolite protons. Unlike water molecules,

which are in fast exchange across the cell membrane, metabolites will undergo relaxation enhancement only if the contrast agent and metabolite are within the same (sub)cellular compartment. Consequently, since electroporation will deliver the contrast agent into the cytoplasm, and in the absence of extracellular contrast agent, metabolite relaxation will only occur if the metabolite is also within the cytoplasm.

*In vivo*, the aplication of a pulsed electric field produces unwanted effects on the electroporated tissue. Several studies have adressed the toxicity of electroporation on muscle tissue[79,80,81] using magnetic resonance imaging (MRI) methods. Consequently, in this study we have also investigated the effects of electroporation on MR spectroscopic detectable metabolites in the absence of contrast agent. Furthermore, we have investigated electroporation-induced intracellular delivery of clinically used MR contrast agents using MRI and MRS, exploring the effects of intracellular contrast

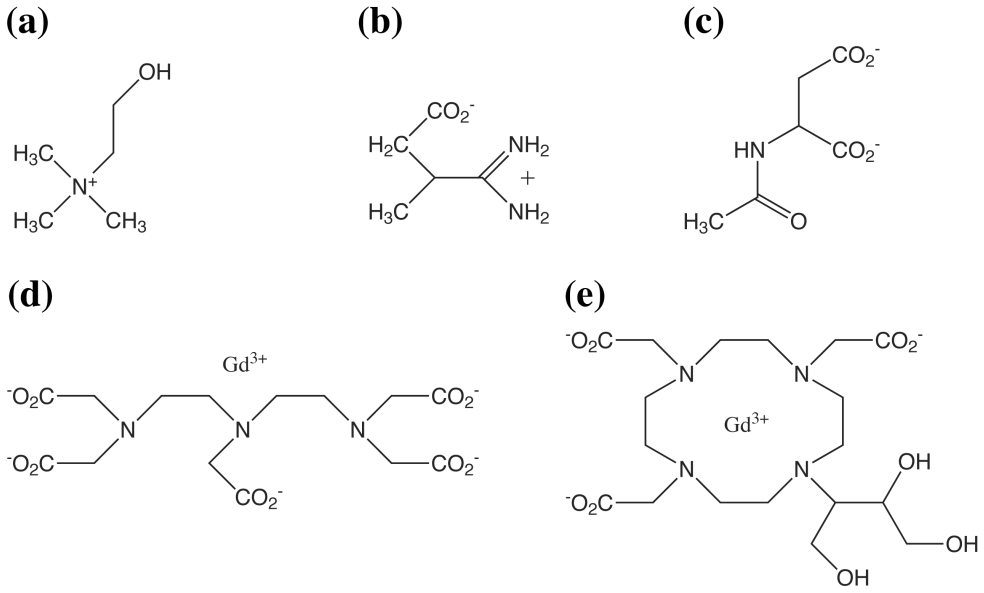


*Figure IV.1: Chemical structures, in charged form, of the metabolites: (a) choline (b) creatine (c) N-acetyl aspartate and contrast agents: (d) Gd-DTPA (Magnevist) and (e) Gd-BT-DO3A (Gadovist). Note that choline possesses an overall positive charge whilst zwitterionic creatine has both positive and negative charges and N-acetyl aspartate has two negatively charged carboxylate groups. Gd-DTPA is negatively charged whilst Gd-BT-DO3A is a neutral molecule.*

agent on MR relaxation of metabolites. Using *in vitro* relaxivity measurements on the three most commonly detected metabolites: choline, creatine, N-acetylaspartate together with water, the intracellular concentrations of the clinically used contrast agents: Magnevist (Gd-DTPA) and Gadovist (Gd-BT-DO3A) (figure IV.1) may be approximated and a measure of the *in vivo* half lives of the contrast agents obtained. In summary, this study aims to investigate the effects of intracellularly trapped contrast agent on MR detectable metabolites, probing their intracellular compartmentalization. In addition, the concentration and half life of intracellular contrast agent trapped in muscle has been estimated and the *in vivo* effects of electroporation on rat muscle have been investigated using $^{1}$H MRS.

## *IV.2 Materials and Methods*

### IV.2.1 Electroporation

Male Sprague Dawley rats (Taconic, Lille Skensved, Denmark) (weight 355+/-52g) were anastesized using a mixture of Hypnorm (VetaPharma Ltd, Leeds, UK), Dormicum (Midazolam (5 mg/ml), Hameln pharmaceuticals, Hameln, Germany) and Atropin (Hospital pharmacies of Denmark, Copenhagen, Denmark). The hind leg was fixated and a tail vein catheter was inserted.
The animals were electroporated five minutes after intra venous injection of contrast agent or saline as follows. A home built array of two rows of four needles (27G) were inserted into the rat hind leg. The needles were separated by 2 mm and the rows by 9 mm. The needle arrays were positioned approximately perpendicular to the long axis of the muscle fibres. 8 pulses of 800 V/cm were applied for 100 µs at 1Hz using a Cyto Pulse PA-4000 Electroporation device (Cyto Pulse Sciences, Glen Burnie, MD, USA). These parameters have previously been shown by Gehl et al[82] to provide optimum intracellular delivery of a metal chelate into muscle tissue. Two separate experiments were performed. In a pilot experiment, four rats were administered, via the cannulated tail vein, 1 ml of Magnevist (0.5M Gd-DTPA, Bayer/Schering, Denmark) 5 minutes prior to electroporation. Following the pilot experiment, a more concentrated contrast agent (Gadovist, 1M Gd-BT-DO3A, Schering, Berlin, Germany) was used

instead. In the main experiment each animal was injected with either: 1 ml of isotonic saline (N=5), 1 ml of Gadovist (N=3) or 1 ml of Gadovist which was diluted 1 to 1 in isotonic saline (N=6) prior to electroporation. The diluted (0.5M) Gadovist was used to compare directly with (0.5M) Magnevist.

### IV.2.2 Magnetic Resonance Imaging and Spectroscopy

All measurements were obtained using a home built volume transmit coil with an inner diameter of 8.5 cm in combination with a 2.5 cm diameter surface receive coil in an experimental 4.7T Varian Inova system suitable for imaging small animals. The electroporated leg was stretched and fixated inside the coil so that the muscle fibers in the leg were aligned approximately parallel to the field.

The animals which were injected with Magnevist (pilot experiment) were scanned 1 day and 1 week after electroporation. The rest of the animals (main) were scanned five times from 1-2 days up to 1 month post-electroporation. Two animals were also scanned two months after electroporation. Seven control (non-electroporated) animals were scanned as controls.

The area of electroporation was identified using a $T_1$W spin echo sequence (TR/TE 360/14 ms, 20 coronal 1 mm slices, FOV 45x45 mm, Matrix 128x128) and a 4x4x4 mm voxel was positioned in the electroporated area (see figure IV.2).

An inversion recovery PRESS sequence was used which included the following RF pulses. A 400µs hard inversion pulse and 90 and 180 degree sinc pulses of 1000 and 1700µs respectively. CHESS water suppression with 15ms gauss pulses was used. TE/TE2 was 10/7 ms.

Water $T_1$ values were obtained using the following parameters: TR = 10 s, 3 averages, 25 inversion times ranging from 100 ms to 5000 ms. Furthermore water $M_0$ was estimated in a scan with no inversion and 3 averages.

Metabolite $T_1$s were measured using CHESS water suppression and the following parameters: TR= 6 s, 100 averages, 5 inversion times 150, 300, 450, 800 and 1400 ms. Furthermore metabolite $M_0$ was estimated in a scan with no inversion a TR of 10 s and 100 averages.

### IV.2.3 Relaxivity measurements

The relaxivity of Magnevist and Gadovist for each of the three most commonly observed *in vivo* metabolites: Cho, Cre and NAA were measured in phantoms containing 25 mM of each metabolite. Two samples were prepared, for each contrast agent, one without bovine serum albumin (BSA) and one with 5% BSA. The BSA was used to estimate the influence of protein binding on relaxivity values and potentially obtain a relaxivity value that is more likely to resemble that observed *in vivo*. Each sample was mixed with varying concentrations of contrast agent (50, 25, 12.5, 6.25, 3.13, 1.56 and 0 µM).
$T_1$ relaxation times of each sample were measured with (30 averages) and without water suppression (10 averages) using the same inversion recovery PRESS sequence as used *in vivo* with the following parameters. TR/TE/TE2=7000/55/15 ms, TI=120,350,1400, 2400,5500 ms, voxel size 4x4x4 mm.

### IV.2.4 Processing

In vivo T1 measurements

All spectra were manually annotated. The following metabolites were visible: cho, total creatine (phosphocreatine and creatine), Intramuscular lipid (methylene) CH2 and (methyl) CH3 groups. In some spectra not all metabolites were visible (due to experimental differences in shim and SNR) and were consequently not annotated. Due to the sensitivity of the MR system, cho was only visible in two control animals.

$T_1$ fitting was performed using a non-linear least squares fitting algorithm[22], which was implemented in MatLab (The Mathworks, Inc). The normal inversion recovery signal equation was modified. Firstly, the effect of non-ideal inversion was included (X). In addition, the difference in magnetisation immediately before inversion, due to varying TI without changing TR, was taken into account (M(0)). The resulting signal equation is shown in equations 1+2.

$$Signal \propto M_0 + \left(M(0) - M_0\right) \cdot e^{-\frac{TI}{T_1}} \quad (1)$$

$$M(0) = M_0 \cdot X \cdot \left(1 - e^{\frac{-(TR-TI)}{T_1}}\right) \quad (2)$$

M(0) is the magnetization immediately after the inversion and X is the inversion efficacy. Typical values lie between -0.7 and -0.9. $T_1$, $M_0$, and X were fitted while the other parameters where known.
Significance between groups was tested using the non parametric wilcoxon rank sum test. Each observation was compared to the saline electroporated groups at the same time point and control animals. A P value of 0.05 or less was considered significant.

In vivo concentration measurements

Metabolite concentrations were estimated by dividing the height of each metabolite in the $M_0$ measurement with the height of the unsuppressed water signal.

In vivo contrast agent concentrations

Contrast agent concentrations over time were estimated from the measured $T_1$ values of water, choline and creatine over time. The concentration of contrast agent was calculated using equation 3 where $T_{1E}$ is the $T_1$ measured in the electroporated animals, $T_{1C}$ is $T_1$ measured in control animals and the relaxivity is the $T_1$ relaxivity measured in phantoms with BSA.

$$[CA] = \frac{\left(\frac{1}{T_{1E}} - \frac{1}{T_{1C}}\right)}{Relaxivity} \quad (3)$$

Relaxivity measurements

The peakhight of each metabolite, in each sample at each TI, was measured using an automatic peak detection method written in MaLab. $T_1$ was fitted using the same method as for the *in vivo* measurements, however the inversion efficiacy (X) was assumed to be equal for all metabolites. The relaxivity for each contrast agent was calculated by fitting a straight line to contrast agent concentration vs $1/T_1$. The error of the fit for the $T_1$ fitting was included as a parameter to the linear fit so that values with high error of fit are given less significance in determining the slope of the line.

Significant differences in relaxivity were tested using a students T-test.

## *IV.3 Results*

### IV.3.1 Relaxivity measurements

The relaxation efficience of Gadovist and Magnevist for each metabolite was studied in phantoms with and without BSA. The results are shown in table 1.

| **Longitudinal relaxivity values ($s^{-1}mM^{-1}$)** | | | | | |
|---|---|---|---|---|---|
| **Phantoms** | **$H_2O$** | **Creatine ($-CH_2$)** | **Choline ($-CH_3$)** | **Creatine ($-CH_3$)** | **NAA ($-CH_3$)** |
| Gadovist | 5.4 (0.4) | 8.2 (0.5) ** | 2.4 (0.1) ** | 4.1 (0.2) ** | 3.7 (0.3) ** |
| Gadovist BSA | 5.6 (0.1) | 8.2 (0.6) ** | 2.3 (0.2) ** | 3.7 (0.3) ** | 3.5 (0.3) ** |
| Magnevist | 4.4 (0.3) | 5.5 (0.5) * | 8.6 (0.2) ** ! | 3.9 (0.2) | 1.7 (0.3) ** |
| Magnevist BSA | 3.8 (0.3) | 4.1 (0.9) | 7.8 (0.3) ** ! | 3.3 (0.4) | 1.0 (0.7) ** |

*Table 1: Metabolite relaxivities for Gadovist and Magnevist with and without BSA.* Denotes statistically different from relaxivity of water (P<0.05). ** P<0.005).! Denotes that these values are statistically different (P<0.05). For P<0.07 all Magnevist metabolites are significantly different between BSA and non-BSA.*

The relaxivities range from 1.0 to 8.2. Most of the metabolite relaxivity values are statistically different from the water relaxivity values. For Gadovist, relaxivity values are not significantly affected by the presence of BSA. Whilst there is a tendency that BSA affects all Magnevist relaxivities (P<0.07), only the choline difference is statistically significant (P<0.05).

### IV.3.2 Imaging

Figure IV.2 shows representative images from individual animals following each treatment at different time points after electroporation. The blue square indicates the location of the spectroscopy voxel. Bright pixels are visible in the saline image after 1-2 days but the rest of the saline images show no enhancement. In the 1-2 day images there are small “holes” in the bright area corresponding to the needle tracks. All electroporated animals show an increase in signal intensity corresponding to the electroporation site. Visual inspection of the images revealed that the electroporated area in the Gadovist animals appeared both brighter and larger than in the Magnevist electroporated animals. It is also apparent that the effect of the entrapped contrast agent is visible up to 2 months after electroporation.

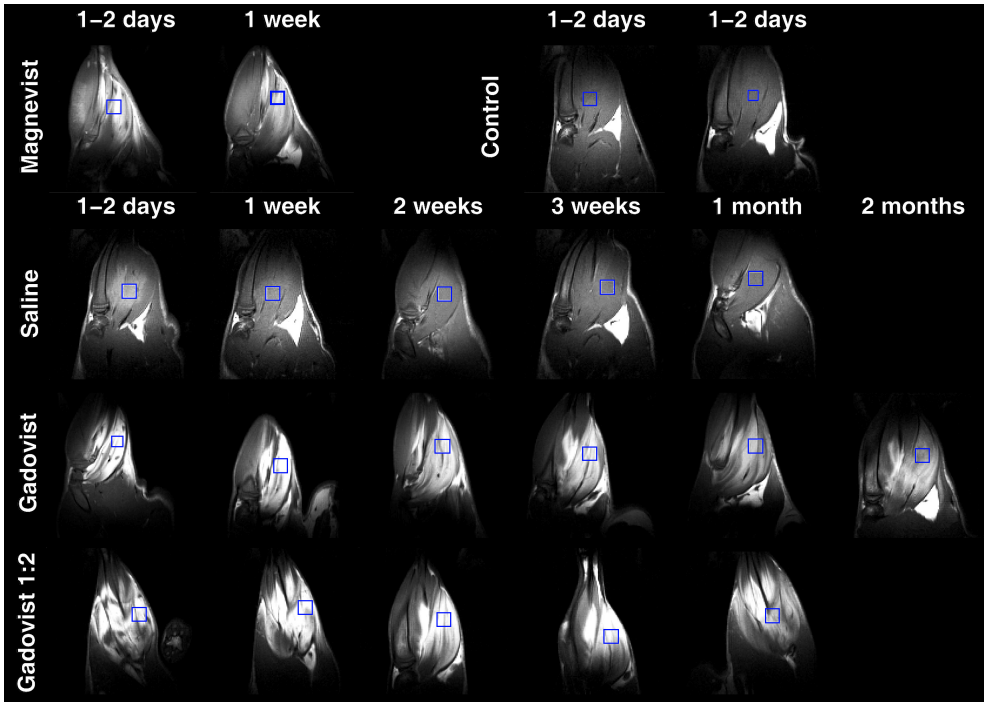


*Figure IV.2: Representative $T_1$ weighted images acquired at different time points after electroporation. For each treatment, images are shown from a single animal. The blue square indicates the location of the spectroscopy voxel*

### IV.3.3 Spectroscopy

T1 values

$T_1$ value as a function of time is shown in figure IV.3. In Cho, tCr and $H_2O$ electroporation with a contrast agent lowers $T_1$ compared to control and saline. In the IMCL (intramyocellular lipids) plots $T_1$ is approximately the same as in the controls.
For Cho, all points (5/5) of the 0.5 Gadovist and most (4/6) of the Gadovist values are significantly lower than the saline values and gradually increases towards the control value. For Magnevist the values are significantly different than saline and the first $T_1$ value is higher than the values for Gadovist.
For tCr (total Creatine = phosphocreatine & creatine) all values of 0.5 Gadovist and most values for Gadovist are significantly different from the control and saline electroporated groups. There is an increase of $T_1$ over time but the increase rate seems to slow over time. For Magnevist the first point is significantly lower than both control and saline and the second point significantly lower than saline. The $T_1$ value for the Magnevist treated animals is higher than for the Gadovist treated animals.
In IMCL-$CH_2$ and $CH_3$ $T_1$ is indepent of treatment and time. However a few points are significantly different from the saline treated group.
For $H_2O$ the picture is more mixed. $T_1$ decreases over time for the first two weeks (except for Gadovist where it increases). The first two values of saline are significantly increased compared to the non electroporated control group, whereafter the $T_1$ of the saline group normalizes. All 0.5 Gadovist values are significantly lower than both saline and control. Most values of Gadovist are significantly lower than the saline and control group. For Magnevist the $T_1$ value after a week is significantly lower than both saline and control but higher than the Gadovist treated animals.

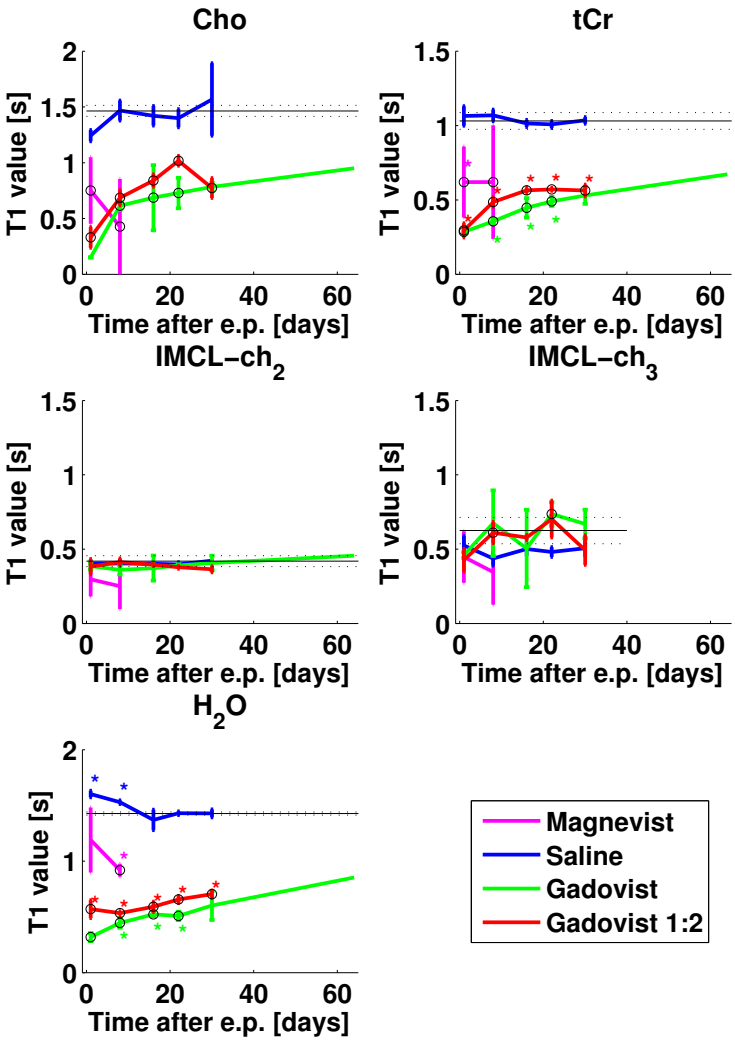


*Figure IV.3: T1 values measured for choline, creatine, IMCL-$CH_2$, IMCL-$CH_3$ and $H_2O$ as a function of time after electroporation. Bars are SEM. The solid black line indicates the mean of the control value (values obtained from untreated animals) while the dashed lines indicate +/- 1 SEM. Points shown as empty circles indicate that the value is significantly different from the mean saline value at the same time point. A * indicates that the value is significantly different from the control value.*

Metabolite concentrations

The concentration of the different metabolites over time were estimated by dividing the metabolite peak heights by the water peak heights (figure IV.4). In all electroporated animals, Cho and Cre concentrations were found to be significantly lower than control animals. Choline is significantly reduced compared to the saline electroporated animals in both Gadovist groups 14 and 21 days after electroporation. For creatine, all the electroporated animals have lower ratios than normal untreated controls. For 0.5 Gadovist and saline the difference is significant after 2 days. Both Gadovist values are significantly higher in ratio than for the saline electroporated group. The recovery of the creatine is equal for all animals.
For IMCL-CH2 and IMCL-CH3 the standard deviations are quite large. Only a 1 points is significantly different from saline controls. Only Gadovist after one week is significantly different from the control values. Although there are few significant differences, there is a tendency that the Gadovist electroporated animals have a higher ratio after one week than the others.

Contast agent concentrations

The concentration of contrast agent vs. time was estimated using the water, choline and creatine $T_1$ measurements and plotted as a function of time (figure IV.6). The half life was fitted assuming monoexponential decay and the results of this fit is shown in table 2. The decay of contrast agent is very similar for Gadovist and 0.5 Gadovist. Although the initial slope and concentration is different depending on the which metabolite is used to estimate contrast agent concentration. Both the Gadovist and 0.5 Gadovist electroporated group seem to reach a plateau concentration of approximately 200 µM.
The Magnevist injected animals show a concentration below 200 µM for both time points irrespective of the way the concentration is estimated.

| **Halflife of ontrast agent (days)** | | |
|---|---|---|
| **Metabolite** | **Gadovist** | **Gadovist 0.5** |
| **Water** | 13.0 | 45.4 |
| **Cho** | 1.3 | 2.2 |
| **Creatine** | 6.3 | 2.5 |

*Table 2: Half life estimated using the metabolites for Gadovist and Gadovist 0.5*

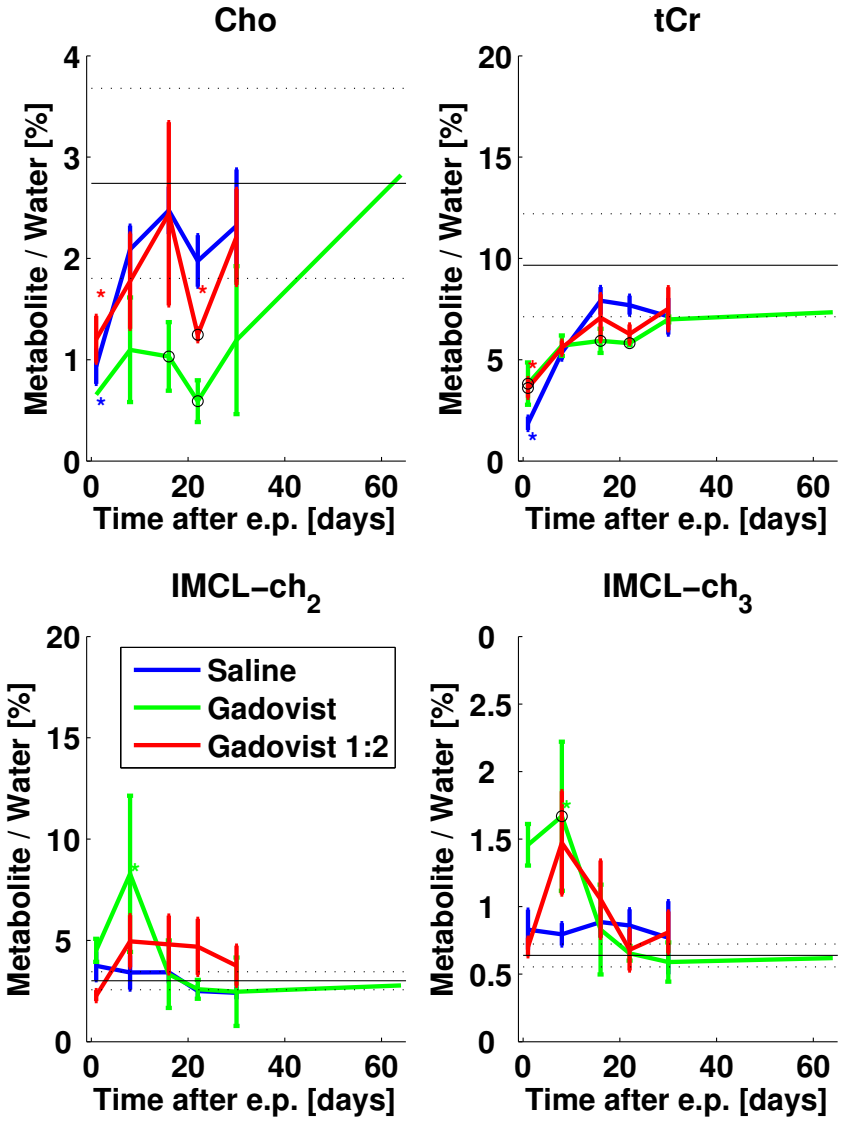


*Figure IV.4: Metabolite concentration estimates: Concentrations were estimated by dividing the peak height of the metabolites (from $M_0$ measurements) divided by peak height of water (from $M_0$ measurements). Points shown as empty circles indicate significant differences from the saline value at the same point. * indicates significant difference from the control values.*

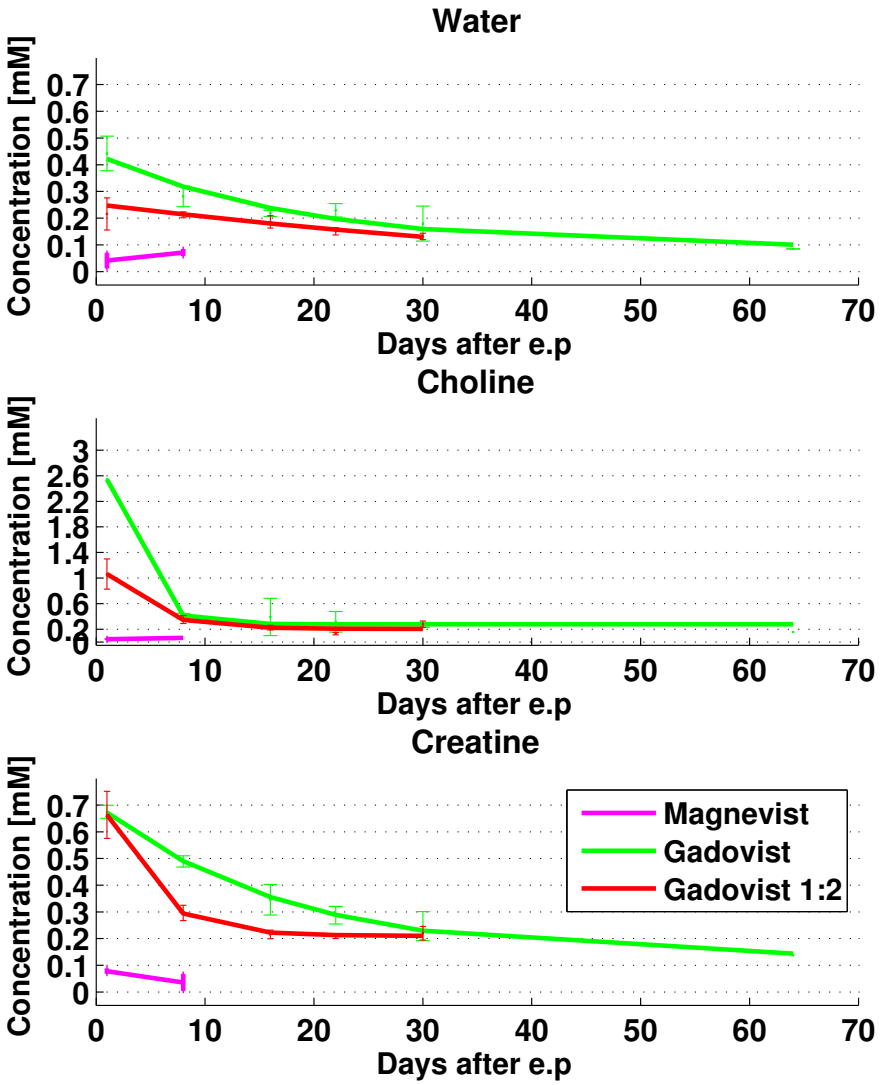


*Figure IV.5: Concentration of contrast agent as a function of time calculated using T1 values of water, cho and creatine.*

As shown in table 2 and as expected from figure IV.5, the measured halflife varies from 1.3 to 45.4 days depending on which metabolite is used to estimate half life. *in vivo* half-life was not estimated for Magnevist as only two time points were acquired in the pilot experiment.

Validation of contrast agent concentrations

In order to validate the calculated contrast agent concentrations correlation plots were made between Cho and water and tCr and water. As shown in figure IV.6 there is good correlation between the values calculated based on Cho and tCr. Furthermore it was shown that the contrast agent concentration values estimated using the metabolites was 1.6 times the contrast agent concentrations estimated using water.

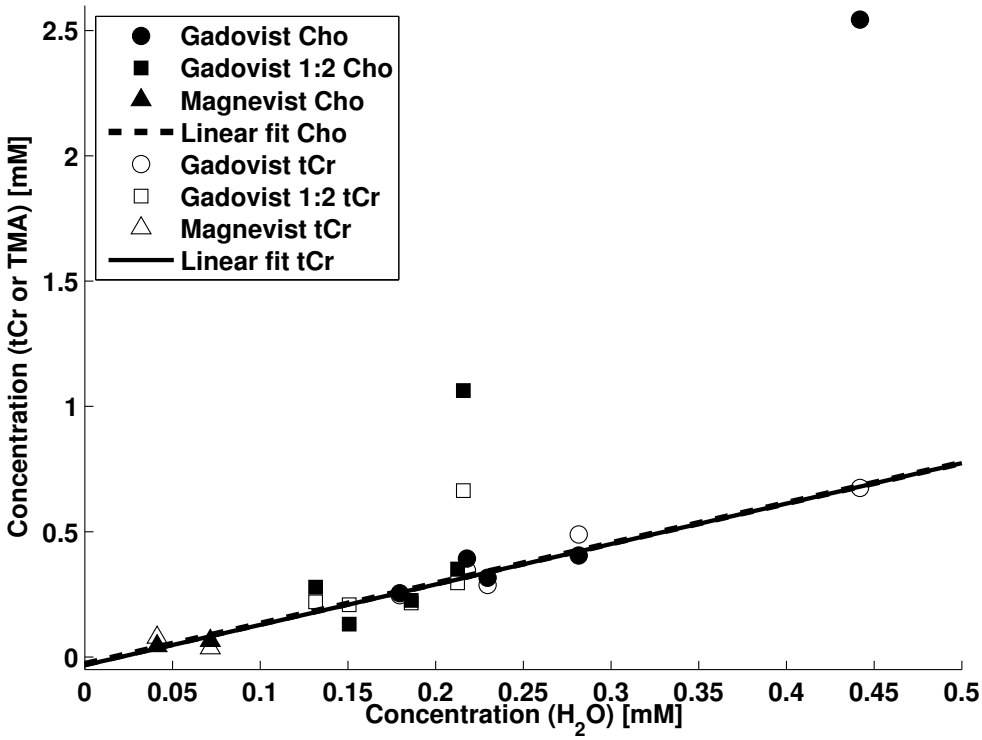


*Figure IV.6: Correlation between contrast agent concentration estimated by water signal and concentrations estimated by Cho and tCr measurements respectively. Both fitted slopes were 1.61 and both correlation coefficients 0.89. The standard error of the fit was 0.21 and 0.07 for Cho and tCr respectively.*

## *IV.4 Discussion*

### IV.4.1 Relaxivities

Relaxivities of creatine, choline and NAA were measured in phantoms with 25 mM of each metabolite and varying amounts of Magnevist or Gadovist. As shown in table 1 all metabolites have significantly different relaxivities than those obtained for water. The results obtained for Gadovist are in accord with those obtained previously for another non-ionic contrast agent (Omniscan) at 1.5T[83]. Relaxivities of 2.6, 3.8 and 3.2 $s^{-1}mM^{-1}$ for choline, creatine and NAA respectively were reported while the results for Gadovist without BSA in this study are similar with values of 2.4, 4.1 and 3.7 $s^{-1}mM^{-1}$ respectively. In this case of the ionic contrast agent Magnevist, the same previous study found relaxivities of 6.6, 3.8 and 1.7 $s^{-1}mM^{-1}$ for choline, creatine and NAA whilst this study found 8.6, 3.9 and 1.7 $s^{-1}mM^{-1}$ for Magnevist without BSA.

The effect of non-specific protein binding on the metabolite relaxivities was assessed using BSA. For Gadovist, a macrocyclic and non-ionic contrast agent (IV.1), the presence of BSA had no significant effect on the measured relaxivities. Magnevist, an ionic contrast agent possesses a double negative charge that will tend to specifically enhance relaxation of positively charged metabolites. Choline possesses a positive charge and hence exhibits the highest (-CH3) relaxivity values. In the BSA samples all metabolites can potentially bind non-specifically to the protein limiting relaxation. However, increased correlation times due to binding will decrease relaxation times hence the observed effects reflect the two competing factors. Consequently, the relaxivities measured in the presence of BSA were used for the calculation of intracellular contrast agent concentrations since non specific binding of the contrast agent inside the cell would be expected.

### IV.4.2 T1 weighted images and T1 values

The $T_1$ of Cho, tCr and Water was reduced in all animals which were electroporated with contrast agent (figure IV.4). This effect lasted up to 2 months and was clearly visible in the $T_1$w images (figure IV.2) and $T_1$ vs time plots (figure IV.4). This is in good agreement with previous findings[81].

For Cho 4/6 of the Gadovist and all 0.5 Gadovist values were significantly lower than saline. For tCr and Water most of the values were significantly different than both control (16/22) and saline values (19/22). For Cho, however, none of the Gadovist electroporated values are significantly different from the control values. This may be due to the sensitivity of the MR experiment since Cho was only visible in two of the control animals, hence the mean and standard error of the mean of the control is poorly defined. For Magnevist the effect on $T_1$ was lower than for both Gadovist and 0.5 Gadovist which is reflected in the estimates of contrast agent concentration shown in figure IV.5, suggesting that the negative charge on the chelate may influence cellular entrapment.

For the two lipid resonances (IMCL-$CH_2$ and $CH_3$), there is no effect of contrast agent and $T_1$ varies little with time. Although two values are significantly higher than the saline values, none are significantly different from the control values. This observation is attributed to the hydrophilic nature of the chelates and the minimal interaction of the contrast agent with the lipid

The animals which were electroporated with saline also appear bright on the $T_1$ weighted images (figure IV.2) while they show an increased $T_1$ on the $T_1$ measurements (figure IV.4). The sequence used is not solely dependent on $T_1$ but is also sensitive to changes in $T_2$. Increased $T_2$ values due to edema therefore contribute to the slight increase in signal intensity following electroporation. Edema resolves after approximately 2 weeks at which time the muscle signal intensity also appears to normalize. A similar pattern is visible in the Gadovist and Magnevist groups in which the $T_1$ of water is slightly higher after 2 days than after a week and then steadily increases towards the value measured in normal controls.

The electroporation process delivers the contrast agent into the cytoplasm[78] and remains trapped in the muscle tissue over a long period of time. The effects of the trapped gadolinium chelate on metabolite relaxation over this period strongly suggests that a signficant fraction of the observed metabolites also reside in the cytoplasm. Consequently, this study demonstrates the ability of extracellular contrast agents to probe the intracellular compartmentalization of MR detectable metabolites when delivered intracellularly using electroporation.

### IV.4.3 Metabolite concentrations

The estimated metabolite concentrations were calculated as the ratio of peakhights from the uninverted water suppressed spectrum and the non water suppressed spectrum using the same sequence parameters. The calculations do not take the $T_1$ shortening effect of the contrast agent in to account. However given the long TR of the $M_0$ measurements (10s) the effect of a reduced $T_1$ is minimal (for a $T_1$ of 2s which is the longest $T_1$ measured the signal is 99.9% of $M_0$).

The estimated concentration of each metabolite as a function of time after electroporation is shown in figure IV.5. The electroporated animals all show less cho and tCr than the non electroporated controls. In 3 cases this difference is significant. For choline, the metabolite is not readily detected in the non-electroporated control animals using the experimental setup described here. Consequently, the levels of choline appear to reflect the effects of the electroporation and may, therefore, indicate tissue damage.

The cho values have much higher SEMs than the rest of the metabolites due to lower signal to noise. For tCr there is a clear trend. tCr is reduced to approximately 4 % of the water peak and over time this increases to around 7.5 % of water which is within the mean + SEM of the normal controls. For the observed lipid resonances (IMCL-CH2 and CH3), there is little difference over time for saline. However both Gadovist groups have a “spike” one week after electroporation. For the Gadovist group this increase is significantly different from the normal controls. This apparent increase in IMCL might be caused by effects similar to what is seen with strenous exercise[84]. With strenous exercise it has been shown that IMCL decreases and after a couple of days increases above normal levels due to replinishment. owever, as the effect is not seen in the saline electroporated animals the cause might be some kind of interaction with Gadovist and may indicate toxicity. The levels of IMCL normalize after approximately three weeks, which fits well with the findings for water T1 in the saline electroporated group and so may reflect resolution of the electroporation-induced edema. Some effects of EMCL contamination cannot be excluded but care was taken to position the voxel in the muscle away from fascias and subcutaneous fat. A study by Boesch et.al[84] has shown that the contamination from EMCL is around 0.1% if the voxel is postitioned with care. Furthermore the same study showed that muscle fibers aligned in

parralel with the magnetic field gives good seperation of EMCL and IMCL. In the present work, the muscle fibers were aligned approximately in parallel with the field so even if EMCL contamination was present it should interfere minimally with the IMCL estimates

### IV.4.4 Contrast agent concentration

The concentration of contrast agent as a function of time was estimated using the $T_1$ relaxation times of water and the two metabolites, choline and tCr together with their *in vitro* relaxivity measurements.

The results based on each metabolite vary significantly, especially in the early time points. Part of this can be explained by the edema which also affects the water T1. After 30 days all the methods agree that the Magnevist concentration is approximately 0.2 mM which is in good agreement with the findings of Leroy-Willing et al[81] who found approximately 0.2 mM trapped in rat muscle 26 days after electroporation with Gd-DOTA. However the initial concentration of contrast agent is much higher than what Leroy-Willing reported which is most likely caused by the differences in delivery. Leroy-Willing uses direct muscular injection of contrast agent which is diluted in saline while intravascular injection of a highly concentrated contrast agent is used in this paper.

The intracellular concentration of Magnevist (<100µM) was significantly lower than the concentrations obtained with Gadovist (up to approximately 1mM, stablizing at approximately 200µM after 1 month). As suggested above, this may be caused by the negative charge of Magnevist but may also be due to linear, less stable structure of Magnevist compared with the cyclic structure of Gadovist and their relative abilities to bind the paramagnetic gadolinium cation. Release of gadolinium would result in increased toxicity, potentially reducing the concentration of the paramagnetic agent. The detection limit of Gd-DTPA is approximately 50µM at 1.5T[85], and it may be lower at higher fieldstrength. Hence, this method feasible for *in vivo* cell labeling studies e.g. cancer metastasis or cell migration.

The half life of the trapped conrast agents are difficult to obtain as it seems the concentration of contrast agent decreases in a mono-exponentially, reaching a plateau of about 0.2 mM in which value it seems to stabilize.

However compared to the half lives of free gadolinium found previously (18.2h[86] and 60 minutes[87]) the half life of the entrapped gadolinium found in this study is much longer as clearly demonstrated by significantly reduced $T_1$ values visible two months after electroporation. This suggest that the gadolinium cation remains chelated over this period. This conclusion is also supported by the correlation between the contrast agent concentrations estimated using water, choline and creatine. If, for example, free gadolinium was released and was responsible for the observed metabolite relaxation, different metabolite relaxivities may be expected due to the postive charge of the gadolinium and consequently would not provide the same correlations.

The concentration of contrast agent estimated using Cho and tCr relaxation was found to be in close agreement and 1.6 times greater than that found using water relaxation. Since water is in fast exchange across cell membranes, intracellular gadolinium may relax extracellular water. Consequently, this difference may reflect the interstitial volume and, using appropriate models, may even allow for estimates of the relative ratio of intracellular and extracellular volume to be obtained

## *IV.5 Conclusion*

We have shown that the contrast agents; Gd-DTPA and Gd-BT-DO3A can be internalized using electroporation. Once the contrast agent is trapped inside muscle cells it may remain there for over 2 months (figure IV.2). This suggest that the method may be usefull for *in vivo* cell labeling studies of e.g. cancer metastasis or cell migration.

Two different contrast agents have been studied. Electroporation following adiministration of Gadovist yielded intracellular contrast agent concentrations which were substantially larger than electroporation following Magnevist.

Cho and tCr concentrations are reduced as a consequence of electroporation. For tCr the concentration normalizes within 3 weeks. For IMCL we have shown a slight increase in the animals electroporated with Gadovist which was not seen in the saline electroporated group that may reflect contrast agent toxicity.

It has further been shown that Gd-DTPA and Gd-BT-DO3A can be used to

probe intracellular compartmentalization in vivo. The T1 s of creatine and TMA were decreased following electroporation when compared to the control and saline electroporated animals (figure IV.4). This is attributed to the contrast agent and metabolite residing in the same compartment as these metabolites.

# Manuscript references


1. Carmeliet, P. Mechanisms of angiogenesis and arteriogenesis. *Nat Med* **6**, 389-95(2000).
2. Carmeliet, P. & Jain, R.K. Angiogenesis in cancer and other diseases. **407**, 249-257(2000).
3. Auerbach, R. et al. Angiogenesis Assays: A Critical Overview. *Clin Chem* **49**, 32-40(2003).
4. Akhtar, N., Dickerson, E.B. & Auerbach, R. The sponge/Matrigel angiogenesis assay. *Angiogenesis* **5**, 75-80(2002).
5. Kragh, M. et al. In vivo chamber angiogenesis assay: an optimized Matrigel plug assay for fast assessment of anti-angiogenic activity. *Int J Oncol* **22**, 305-11(2003).
6. Ley, C.D. et al. Angiogenic synergy of bFGF and VEGF is antagonized by Angiopoietin-2 in a modified in vivo Matrigel assay. *Microvascular Research* **68**, 161-168(2004).
7. Artemov, D. et al. Dynamics of prostate cancer cell invasion studied in vitro by NMR microscopy. *Magn Reson Med* **42**, 277-82(1999).
8. Pilatus, U. et al. Imaging Prostate Cancer Invasion with Multi-Nuclear Magnetic Resonance Methods: The Metabolic Boyden Chamber. *Neoplasia (New York, N.Y.)* **2**, (2000).
9. D'Amato, R.J. et al. Thalidomide is an inhibitor of angiogenesis. *Proceedings of the National Academy of Sciences of the United States of America* **91**, (1994).
10. Downs, L.S. et al. Thalidomide and angiostatin inhibit tumor growth in a murine xenograft model of human cervical cancer. *Gynecol Oncol* **98**, 203-10(2005).
11. Hallene, K.L. et al. Prenatal exposure to thalidomide, altered vasculogenesis, and CNS malformations. *Neuroscience* **142**, 267-83(2006).
12. D'Amato, R.J. et al. Mechanism of action of thalidomide and 3-aminothalidomide in multiple myeloma. *Semin Oncol* **28**, 597-601(2001).
13. Komorowski, J. et al. Effect of thalidomide affecting VEGF secretion, cell migration, adhesion and capillary tube formation of human endothelial EA.hy 926 cells. *Life Sci* **78**, 2558-63(2006).
14. Kenyon, B.M., Browne, F. & D'Amato, R.J. Effects of thalidomide and related metabolites in a mouse corneal model of neovascularization. *Exp Eye Res* **64**, 971-8(1997).
15. Friedlander, M. et al. Definition of two angiogenic pathways by distinct alpha v integrins. *Science* **270**, 1500-2(1995).
16. Stephens, T.D. & Fillmore, B.J. Hypothesis: thalidomide embryopathy-proposed mechanism of action. *Teratology* **61**, 189-95(2000).
17. Neubert, R. et al. Down-regulation of adhesion receptors on cells of primate embryos as a probable mechanism of the teratogenic action of thalidomide. *Life Sci* **58**, 295-316(1996).

18. Gelati, M. et al. Effects of thalidomide on parameters involved in angiogenesis: an in vitro study. *J Neurooncol* **64**, 193-201(2003).
19. Bertolini, F. et al. Thalidomide in multiple myeloma, myelodysplastic syndromes and histiocytosis. Analysis of clinical results and of surrogate angiogenesis markers. *Ann Oncol* **12**, 987-90(2001).
20. Stephens, T.D., Bunde, C.J. & Fillmore, B.J. Mechanism of action in thalidomide teratogenesis. *Biochem Pharmacol* **59**, 1489-99(2000).
21. Ley, C. et al. Development of an MR Compatible in vivo Angiogenesis Assay. *Proc 12th annual meeting ISMRM* 1970(2004).
22. Marquardt, D.W. *An algorithm for least-squares estimation of nonlinear parameters*. **11**, 431-441(1963).
23. Baker, J.H.E. et al. Vascular-specific quantification in an in vivo Matrigel chamber angiogenesis assay. *Microvasc Res* **71**, 69-75(2006).
24. Tamilarasan, K.P. et al. Thalidomide attenuates nitric oxide mediated angiogenesis by blocking migration of endothelial cells. *BMC Cell Biology* **7**, (2006).
25. Olsen, M.W.B. et al. Angiopoietin-4 Inhibits Angiogenesis and Reduces Interstitial Fluid Pressure. *Neoplasia (New York, N.Y.)* **8**, (2006).
26. Yuan, F. et al. Vascular permeability and microcirculation of gliomas and mammary carcinomas transplanted in rat and mouse cranial windows. *Cancer Res* **54**, 4564-8(1994).
27. Artemov, D. et al. Pharmacokinetics of the 13C labeled anticancer agent temozolomide detected in vivo by selective cross-polarization transfer. *Magn Reson Med* **34**, 338-42(1995).
28. Ruiz-Cabello, J. et al. Gradient-enhanced heteronuclear correlation spectroscopy. Theory and experimental aspects. . *J Magn Reson* **100**, 282-302(1992).
29. Kato, Y., Okollie, B. & Artemov, D. Noninvasive 1H/13C magnetic resonance spectroscopic imaging of the intratumoral distribution of temozolomide. *Magn Reson Med* **55**, 755-61(2006).
30. Garwood, M. & Ke, Y. Symmetric pulses to induce arbitrary flip angles with compensation for RF inhomogeneity and resonance offsets. *J Magn Reson* **94**, 511-25
31. Bhujwalla, Z.M. et al. Vascular differences detected by MRI for metastatic versus nonmetastatic breast and prostate cancer xenografts. *Neoplasia* **3**, 143-53
32. Ostrowitzki, S. et al. Comparison of gadopentetate dimeglumine and albumin-(Gd-DTPA)30 for microvessel characterization in an intracranial glioma model. *J Magn Reson Imaging* **8**, 799-806
33. Tofts, P.S. et al. Estimating kinetic parameters from dynamic contrast-enhanced T(1)-weighted MRI of a diffusable tracer: standardized quantities and symbols. *J Magn Reson Imaging* **10**, 223-32(1999).
34. Wu, O. et al. Tracer arrival timing-insensitive technique for estimating flow in MR perfusion-weighted imaging using singular value decomposition with a block-circulant deconvolution matrix. *Magn Reson Med* **50**, 164-74(2003).
35. Belliveau, J.W. et al. Functional cerebral imaging by susceptibility-contrast NMR. *Magn Reson Med* **14**, 538-46(1990).
36. Dijkhuizen, R.M. & Nicolay, K. Magnetic resonance imaging in experimental models of brain disorders. *J Cereb Blood Flow Metab* **23**, 1383-402(2003).
37. Kato, Y. et al. Contributing factors of temozolomide resistance in MCF-7 tumor xenograft models. *Cancer Biol Ther* **6**, 891-7(2007).
38. Bocangel, D.B. et al. Multifaceted resistance of gliomas to temozolomide. *Clin Cancer Res* **8**, 2725-34(2002).
39. Ma, J. et al. Biochemical changes associated with a multidrug-resistant phenotype of a human glioma cell line with temozolomide-acquired resistance. *Biochem Pharmacol* **63**, 1219-28(2002).
40. Yuan, F. et al. Vascular permeability in a human tumor xenograft: molecular size dependence and cutoff size. *Cancer Res* **55**, 3752-6(1995).
41. Warmuth, C., Gunther, M. & Zimmer, C. Quantification of Blood Flow in Brain Tumors:

Comparison of Arterial Spin Labeling and Dynamic Susceptibility-weighted Contrast-enhanced MR Imaging. *Radiology* **228**, 523-532(2003).
42. Sun, Y. et al. Perfusion MRI of U87 brain tumors in a mouse model. *Magn Reson Med* **51**, 893-9(2004).
43. Pathak, A.P., Rand, S.D. & Schmainda, K.M. The effect of brain tumor angiogenesis on the in vivo relationship between the gradient-echo relaxation rate change (DeltaR2*) and contrast agent (MION) dose. *J Magn Reson Imaging* **18**, 397-403(2003).
44. Boxerman, J.L., Schmainda, K.M. & Weisskoff, R.M. Relative cerebral blood volume maps corrected for contrast agent extravasation significantly correlate with glioma tumor grade, whereas uncorrected maps do not. *AJNR Am J Neuroradiol* **27**, 859-67(2006).
45. Donahue, K.M. et al. Utility of simultaneously acquired gradient-echo and spin-echo cerebral blood volume and morphology maps in brain tumor patients. *Magn Reson Med* **43**, 845-53(2000).
46. Ostermann, S. et al. Plasma and cerebrospinal fluid population pharmacokinetics of temozolomide in malignant glioma patients. *Clin Cancer Res* **10**, 3728-36(2004).
47. Barrett, T. et al. MRI of tumor angiogenesis. *Journal of Magnetic Resonance Imaging* **26**, 235-249(2007).
48. Hashizume, H. et al. Openings between Defective Endothelial Cells Explain Tumor Vessel Leakiness. *Am J Pathol* **156**, 1363-1380(2000).
49. Guy, C.T., Cardiff, R.D. & Muller, W.J. Induction of mammary tumors by expression of polyomavirus middle T oncogene: a transgenic mouse model for metastatic disease. *Mol Cell Biol* **12**, 954-61(1992).
50. Dankort, D.L. & Muller, W.J. Signal transduction in mammary tumorigenesis: a transgenic perspective. *Oncogene* **19**, 1038-44(2000).
51. Lin, E.Y. et al. Progression to malignancy in the polyoma middle T oncoprotein mouse breast cancer model provides a reliable model for human diseases. *Am J Pathol* **163**, 2113-26(2003).
52. Maglione, J.E. et al. Transgenic Polyoma middle-T mice model premalignant mammary disease. *Cancer Res* **61**, 8298-305(2001).
53. Wedam, S.B. et al. Antiangiogenic and Antitumor Effects of Bevacizumab in Patients With Inflammatory and Locally Advanced Breast Cancer. *J Clin Oncol* **24**, 769-777(2006).
54. Gossmann, A. et al. Dynamic contrast-enhanced magnetic resonance imaging as a surrogate marker of tumor response to anti-angiogenic therapy in a xenograft model of glioblastoma multiforme. *J Magn Reson Imaging* **15**, 233-40(2002).
55. Ikeda, O., Yamashita, Y. & Takahashi, M. Gd-enhanced dynamic magnetic resonance imaging of breast masses. *Top Magn Reson Imaging* **10**, 143-51(1999).
56. Cha, S. et al. Dynamic, contrast-enhanced perfusion MRI in mouse gliomas: correlation with histopathology. *Magn Reson Med* **49**, 848-55(2003).
57. Su, M. et al. Pharmacokinetic parameters analyzed from mr contrast enhancement kinetics of multiple malignant and benign breast lesions detected in the same patients. *Technol Cancer Res Treat* **4**, 255-63(2005).
58. Hulka, C.A. et al. Dynamic echo-planar imaging of the breast: experience in diagnosing breast carcinoma and correlation with tumor angiogenesis. *Radiology* **205**, 837-42(1997).
59. Tikhonov, A. Solution of incorrectly formulated probles and the regularization method. *Soviet Math Dokl* **4**, 1035-1038(1963).
60. Patlak, C.S., Blasberg, R.G. & Fenstermacher, J.D. Graphical evaluation of blood-to-brain transfer constants from multiple-time uptake data. *J Cereb Blood Flow Metab* **3**, 1-7(1983).
61. Larsson, H.B.W. et al. Dynamic contrast-enhanced quantitative perfusion measurement of the brain using T1-weighted MRI at 3T. *J Magn Reson Imaging* **27**, 754-62(2008).
62. Larson, K.B. et al. Tracer-kinetic analysis for measuring regional cerebral blood flow by dynamic nuclear magnetic resonance imaging. *J Theor Biol* **170**, 1-14(1994).
63. Larsson, H.B.W. et al. Myocardial perfusion modeling using MRI. *Magnetic Resonance in*

*Medicine* **35**, 716-726(1996).
64. Almholt, K. et al. Reduced metastasis of transgenic mammary cancer in urokinase-deficient mice. *Int J Cancer* **113**, 525-32(2005).
65. Ewing, J.R. et al. Model selection in magnetic resonance imaging measurements of vascular permeability: Gadomer in a 9L model of rat cerebral tumor. *J Cereb Blood Flow Metab* **26**, 310-320(2005).
66. Larsson, H.B. et al. Measurement of brain perfusion., blood volume and blood brain barrier permeability using dynamic contrast enhanced T1-weighted MRI at 3 tesla. *In preperation*
67. Cenic, A. et al. A CT Method to Measure Hemodynamics in Brain Tumors: Validation and Application of Cerebral Blood Flow Maps. *AJNR Am J Neuroradiol* **21**, 462-470(2000).
68. Galbraith, S.M. et al. Combretastatin A4 Phosphate Has Tumor Antivascular Activity in Rat and Man as Demonstrated by Dynamic Magnetic Resonance Imaging. *J Clin Oncol* **21**, 2831-2842(2003).
69. Pham, C.D. et al. Magnetic resonance imaging detects suppression of tumor vascular permeability after administration of antibody to vascular endothelial growth factor. *Cancer Invest* **16**, 225-30(1998).
70. Cemazar, M. & Sersa, G. Electrotransfer of therapeutic molecules into tissues. *Curr Opin Mol Ther* **9**, 554-62(2007).
71. Sersa, G. et al. Electrochemotherapy in treatment of tumours. *European Journal of Surgical Oncology (EJSO)* **34**, 232-240(2008).
72. Gothelf, A., Mir, L.M. & Gehl, J. Electrochemotherapy: results of cancer treatment using enhanced delivery of bleomycin by electroporation. *Cancer Treat Rev* **29**, 371-87(2003).
73. Takei, Y. et al. In vivo silencing of a molecular target by short interfering RNA electroporation: tumor vascularization correlates to delivery efficiency. *Mol Cancer Ther* **7**, 211-21(2008).
74. Rogers, W.J., Meyer, C.H. & Kramer, C.M. Technology Insight: in vivo cell tracking by use of MRI. *Nat Clin Pract Cardiovasc Med* **3**, 554-562(2006).
75. Walczak, P. et al. Magnetoelectroporation: improved labeling of neural stem cells and leukocytes for cellular magnetic resonance imaging using a single FDA-approved agent. *Nanomedicine: Nanotechnology, Biology and Medicine* **2**, 89-94(2006).
76. Walczak, P. et al. Instant MR labeling of stem cells using magnetoelectroporation. *Magnetic Resonance in Medicine* **54**, 769-774(2005).
77. Daldrup-Link et al. In vivo tracking of genetically engineered, anti-HER2/neu directed natural killer cells to HER2/neu positive mammary tumors with magnetic resonance imaging. *European Radiology* **15**, 4-13(2005).
78. Terreno, E. et al. Effect of the intracellular localization of a Gd-based imaging probe on the relaxation enhancement of water protons. *Magnetic Resonance in Medicine* **55**, 491-497(2006).
79. Gissel, H. et al. Magnetic Resonance Imaging of Changes in Muscle Tissues after Membrane Trauma. *Annals of the New York Academy of Sciences* **1066**, 272-285(335).
80. Lee, R. et al. Magnetic resonance imaging of muscle electroporation injury. *Engineering in Medicine and Biology Society, 2004. IEMBS '04. 26th Annual International Conference of the IEEE* **2**, 5451-5454 Vol.7(2004).
81. Leroy-Willig, A. et al. In vivo NMR imaging evaluation of efficiency and toxicity of gene electrotransfer in rat muscle. *Gene Ther* **12**, 1434-1443(2005).
82. Gehl, J. et al. In vivo electroporation of skeletal muscle: threshold, efficacy and relation to electric field distribution. *Biochimica et Biophysica Acta (BBA) - General Subjects* **1428**, 233-240(1999).
83. Murphy, P.S., Leach, M.O. & Rowland, I.J. Signal modulation in 1H magnetic resonance spectroscopy using contrast agents: Proton relaxivities of choline, creatine, and N-acetylaspartate. *Magnetic Resonance in Medicine* **42**, 1155-1158(1999).
84. Boesch, C. et al. Role of proton MR for the study of muscle lipid metabolism. *NMR in*

*Biomedicine* **19**, 968-988(2006).
85. Langereis, S. et al. Evaluation of Gd(III)DTPA-terminated poly(propylene imine) dendrimers as contrast agents for MR imaging. *NMR Biomed* **19**, 133-41(2006).
86. Port, M. et al. Stability of gadolinium chelates and their biological consequences: new data and some comments. *Br J Radiol* **81**, 258-259(2008).
87. Vogler, H. et al. Pre-clinical evaluation of gadobutrol: a new, neutral, extracellular contrast agent for magnetic resonance imaging. *European Journal of Radiology* **21**, 1-10(1995).